2014

Fragmentation Analysis in the Dynamic Stress Wave Collision Regions in Bench Blasting

Catherine E. Johnson
University of Kentucky, catherinejohnson589@gmail.com

STUDENT AGREEMENT:

I represent that my thesis or dissertation and abstract are my original work. Proper attribution has been given to all outside sources. I understand that I am solely responsible for obtaining any needed copyright permissions. I have obtained needed written permission statement(s) from the owner(s) of each third-party copyrighted matter to be included in my work, allowing electronic distribution (if such use is not permitted by the fair use doctrine) which will be submitted to UKnowledge as Additional File.

I hereby grant to The University of Kentucky and its agents the irrevocable, non-exclusive, and royalty-free license to archive and make accessible my work in whole or in part in all forms of media, now or hereafter known. I agree that the document mentioned above may be made available immediately for worldwide access unless an embargo applies.

I retain all other ownership rights to the copyright of my work. I also retain the right to use in future works (such as articles or books) all or part of my work. I understand that I am free to register the copyright to my work.

REVIEW, APPROVAL AND ACCEPTANCE

The document mentioned above has been reviewed and accepted by the student's advisor, on behalf of the advisory committee, and by the Director of Graduate Studies (DGS), on behalf of the program; we verify that this is the final, approved version of the student's thesis including all changes required by the advisory committee. The undersigned agree to abide by the statements above.

Catherine E. Johnson, Student

Dr. Braden Lusk, Major Professor

Dr. Thomas Novak, Director of Graduate Studies

FRAGMENTATION ANALYSIS IN THE DYNAMIC STRESS WAVE COLLISION REGIONS IN BENCH BLASTING

DISSERTATION

A dissertation submitted in partial fulfillment of the
requirements for the degree of Doctor of Philosophy in the
College of Engineering
at the University of Kentucky

By
Catherine Emily Johnson
Lexington, Kentucky
Director: Dr. Braden Lusk, Associate Professor of Mining Engineering
Lexington, Kentucky
2014

ABSTRACT OF DISSERTATION

FRAGMENTATION ANALYSIS IN THE DYNAMIC STRESS WAVE COLLISION REGIONS IN BENCH BLASTING

The first step in many mining operations is blasting, and the purpose of blasting is to fragment the rock mass in the most efficient way for that mine site and the material end use. Over time, new developments to any industry occur, and design and implementation of traditional techniques have to change as a consequence. Possibly the greatest improvement in blasting in recent years is that of electronic detonators. The improvements related to safety and increased fragmentation have been invaluable. There has been ongoing debate within the explosives industry regarding two possible theories for this. Shorter timing delays that allow interaction between adjacent shock waves or detonation waves, or the increase in accuracy associated with electronic detonators. Results exist on the improved accuracy of electronic detonators over that of electric or non-electric, but data on the relationship between the collision of dynamic stress waves and fragmentation is less understood. Publications stating that the area of greatest fragmentation will occur between points of detonation where shock waves collide exist, but experimental data to prove this fact is lacking.

This dissertation looks extensively at the head on collision of shock (in the rock mass) and detonation (in the detonation column) waves with relation to fragmentation through a number of small scale tests in concrete. Timing is a vital tool for this collision to occur and is the variable utilized for the studies. Small scale tests in solid masonry blocks, 15 x $7\ \frac{7}{8}$ x $7\ \frac{7}{8}$ inches in size, investigated shock and detonation wave collisions with instantaneous detonation. Blocks were wrapped in geotextile fabric and a wire mesh to contain the fragments so that in situ tensile crack formations could be analyzed. Detonating cord was used as the explosive with no stemming to maintain the shock pressure but reduce the gas pressure phase of the fragmentation cycle. Model simulations of these blocks in ANSYS Autodyn looked at the stress and pressure wave patterns and corresponding damage contours for a direct comparison with the experimental investigation.

Detonation wave collision in a single blast hole was found to positively influence the fragmentation and throw of the material. Mean fragment size decreased compared to tests with no detonation wave collision. Area of greatest throw occurred at the point of detonation collision where a buildup of gas pressure exited the block from one location.

Head on collision of shock waves did not positively influence the muck pile. Largest fragments were located at the point of shock collision. The lack of particle velocity with relation to shock collision in previous literature could be attributed to the increased particle size here. Directional particle velocities could actually increase the strength and density of the rock at this location, decreasing the degree of fragmentation rather than increasing it.

KEYWORDS: Fragmentation, Shock and Detonation Wave Collison, Timing, Electronic Detonators, Finite Element Model

Catherine Emily Johnson

Student's Signature

12/15/2014

Date

FRAGMENTATION ANALYSIS IN THE DYNAMIC STRESS WAVE COLLISION REGIONS IN BENCH BLASTING

By

Catherine Emily Johnson

Dr Braden Lusk

Director of Dissertation

Dr Thomas Novak

Director of Graduate Studies

12/15/2014

Date

ACKNOWLEDGEMENTS

Without the help and support of the following people, the successful completion of this dissertation would not have been possible. To them I am eternally grateful.

First, I would like to thank Dr. Braden Lusk for giving me the opportunity to study for my doctorate degree under his supervision. The support, lessons learned and experiences he has shared go far beyond the pages here or words I could express.

Thanks also go to my coworkers, Joshua Hoffman, William Wietzel and Joshua Calnan who have helped with data collection, ideas and support on the subject. I would also like to express my gratitude to the Professors that served as my Advisory Committee. Their input in the final stages of my degree was invaluable.

Lastly I would like to thank my friends and family for their kind words and support during this stressful time. Alex in particular has been my rock throughout my graduate degree. His motivation, as well as the numerous technical discussions we shared did not go unnoticed. I would not be here without you, thank you.

TABLE OF CONTENTS

LIST OF TABLES

LIST OF FIGURES

Chapter 1. Introduction

The largest user of explosives is by far the mining industry, where they are used extensively for rock fragmentation, to both break up and uncover ore or coal. Optimum fragmentation can be looked at in a number of ways. MacKenzie (1966) described optimum fragmentation to be "that blasting practice which gives the degree of fragmentation necessary to obtain the lowest unit cost of the combined operations of drilling, loading, hauling and crushing." Since the introduction of environmental regulations and new developments in explosive and blasting techniques, blasts can no longer be designed simply around monetary cost. An optimized blast design is one that will break or move rock to the required fragment size for secondary equipment to efficiently handle it. All this must be done while minimizing secondary components such as cost and environmental effects including ground vibration and airblast. To that end, the optimization of blasting is not achieved in the same way at every site. This suggests a modern need for optimization tools that allow for adjustments in fragmentation distribution through changes in a number of input variables, including that of timing. The Kuz-Ram Model for fragmentation distribution prediction is still widely used; using blast parameters burden, spacing and face height along with strata properties to calculate a mean fragmentation size. A number of improvements to the model have been made but none include that of timing; which is now known to have a significant contribution to fragmentation.

Traditionally, fragmentation size at a blast site was designed dependent on powder factor: pounds of explosive per cubic yards of rock moved (lbs/yd^3). An easy way to increase fragmentation is to increase your powder factor. Powder factor ties in closely with blast design parameters including burden, spacing, hole diameter and face height. Clearly the closer together your blast holes are and a greater weight of explosives per hole will increase your fragmentation. Increased fragmentation in this instance is a lower mean fragmentation size. This is however not an ideal definition of 'increased fragmentation'. A bimodal distribution with a large proportion of fines and some large fragments will reduce the mean fragment size significantly but may not be beneficial to the mine. Increased fragmentation should therefore be defined based solely on a normal distribution

with the majority of particles the same size, or the term ‘desirable fragmentation’ be used. With increased powder factor, blasting cost also increases so a balance between the two is established at any one blast site. Fragmentation should be optimized to produce the lowest operational cost including all factors of mining. Costs associated with the environment must be considered.

One of the biggest breakthroughs in recent years in blasting is electronic detonators; manufactures represent an accuracy of plus or minus 1 ms in most cases. A number of mine sites have seen an increase in fragmentation (Verbal discussions with Dyno Nobel, 2014) since they have been using electronic detonators. One possible, but controversial, theory is that since shorter delay times are now possible, shockwaves between holes can collide and increase fragmentation between two adjacent blast holes (Yamamoto, 1999 and Rossmanith, 2003). No conclusive data on this is available. Data is, however, available on the increased accuracy of these detonators over electric or non-electric initiation systems that have accuracies as low as plus or minus 5%. The increase in fragmentation could therefore also be due to this reduced cap scatter and no holes firing out of sequence, a large contributor to poor fragmentation. Timing a mine blast has traditionally been related to environmental considerations and a maximum quantity of explosives per 8 ms time delay. The practice of dual initiation using precise timing from electronic detonators in boreholes is thought to be beneficial for increasing fragmentation at a desired location in the rock strata. This increased capacity for fragmentation is understood to be a product of both the collision of detonation waves in the explosive column and an increased energy liberation rate, each resulting from dual initiation.

The interaction of shock waves for years has been associated with the resultant line crack of a smooth blast or pre-split. Literature is available discussing the theory that shock wave interaction between adjacent holes in a presplit forms the cracks that join the blast holes. (ISEE, 1998, Muller et al, 2013). Pre-split and smooth blasting techniques involve a lower powder factor and often decoupled holes, reducing the intensity of the shock wave on the surroundings, effectively reducing the dynamic effects of the explosive. Shock wave collision theories by Rossmanith (2003) suggest an increase in fragmentation is found at this location. The two theories contradict so both, if either,

cannot coincide. Worsey (1986) argues that the pre-split is actually due to hydrofracture, not the interaction of stress waves. This process can be coupled with that of timing and fragmentation while looking at instantaneous detonation at distances where shock waves will overlap.

Timing is now a crucial part of the blast design process, along with traditional parameters of powder factor and blast geometries; burden, spacing and hole diameter. Precise timing of electronic detonation is thought to provide a mechanism for controlling the collision of shockwaves or detonation waves when strata characteristics are understood, however the fundamentals surrounding the collision of stress waves is controversial. Due to the nature of the muck pile produced after a blast and the difficulty of recording these waves through strata, quantitative evidence to support this theory has proved difficult to attain. This dissertation uses experimental and finite element modelling techniques to understand the interaction of dynamic stress waves and how they affect fragmentation.

Chapter 2. Rationale

As a blast detonates, the rock immediately surrounding the blast hole is crushed and a compressive shockwave with trailing tensile wave expands out from the blast hole in all directions (Cooper, 1996). When two of these shockwaves collide, controversy arises as to whether the collision of these waves producing an increase in pressure and reflecting back (Cooper, 1996), the expanding gas pressure, an increase in detonator accuracy or a different novel theory which is responsible for the increased fragmentation documented by mining companies. Head on collision of detonation waves, and the resultant shock wave, vertically in strata is thought to increase fragmentation at the point at which they meet. This dissertation aims to shed some light on the fragmentation process based on these underexplored theories.

The Kuz-Ram model uses blast design inputs to calculate fragmentation distribution. It is still widely used, utilizing basic blast design parameters to calculate fragmentation size distribution. The model is based on traditional blast parameters before the invention of precise initiator timing. For this reason, the model is scrutinized for its accuracy in today's market. What is not clear is how the fragmentation process actually works with short delay timing. Does the traditional process of extensive cracking around the blast hole from the shockwave followed by extension of cracks to the face and expansion due to gas pressure still apply? Or, have people have simply got carried away with shockwave collision after these short delay times have become possible?

2.1 Goals and objectives

Research for the dissertation will focus on four main research areas associated with recent discussions related the fragmentation process. The four main objectives are:

1. Small scale experiments on the collision of shock waves and detonation waves in uniform concrete masonry blocks and examine the resultant fragmentation.
2. Implement finite element models to correlate the fragmentation patterns observed in experimental tests with the stress and pressure contours simulated in models.
3. Correlate the small scale tests where shock wave collision occurs to the pre-split theory, where the overlapping shock waves produce an adjacent line crack.

4. Relate the distribution of dynamic stresses within small scale tests to a full scale production blast.

2.2 Novel contribution to research

The objectives of this dissertation will provide a significant contribution to the industry through shedding light on a number of underexplored theories related to the effects of timing detonation and shock collisions on fragmentation in surface mine blasting. The cost of an electronic detonator is significantly higher than that of a less accurate electric or non-electric detonator. Manufactures have been known to sell their product based on improvements observed in fragmentation due to the ability for short time delays where shock collisions can occur, consequently reducing downstream costs. Increasing total blasting costs through electronic detonators, multiple detonators and reducing the distance between holes so that shock waves can collide between can be detrimental to total production costs if there are no significant improvements to fragmentation for that site. Understanding the fundamentals behind shock wave and detonation wave interactions is new to the mining industry. The increased accuracy of electronics is fact; shock collision influencing fragmentation is not. Understanding these phenomena can go a long way in overcoming difficulties in the explosives industry as costs of detonators and new technologies in the industry are increasing at the same time environmental regulations are more stringent and fines increasing.

Chapter 3. Literature Review

Fragmentation produced as a result of blasting practices are complex and based on a number of controlled, (blast design, explosive selection etc.) and uncontrollable (misfires, rock type, joints etc.) variables. There are several approaches in modelling, predicting and adjusting fragmentation, many of which many don't agree. A number of studies have been published based on "improvements" at their one location or mathematical models with no empirical proof. The following sections review a number of these, starting with the basic fragmentation process.

3.1 Introduction to bench blast fragmentation

There are three general types of explosives; one way to categorize them is Primary, Secondary and Blasting Agents, based primarily on the shock amplitude necessary to detonate them. Primary explosives only require a small shock to detonate them and are used in modern day detonators, secondary explosives require a low pressure to detonate but blasting agents require much higher pressures to detonate. It is blasting agents that are primarily used in bench blasting, initiated using a combination of primary and secondary explosives. Each blast hole is initiated on a separate time delay to both reduce adverse effects (ground vibration and airblast) and improve the fragmentation process by allowing rock in front of the blast hole to move out the way creating a free face. Detonators have come a long way since the use of black powder and safety fuse to precise initiation using electronic detonators. Electronic detonators have a microchip that can currently be programmed in millisecond (ms) increments. This is far more accurate than the cheaper pyrotechnic initiators where the timing comes from a specified length of pyrotechnic element. At times, the inaccuracy in these can cause holes to fire out of sequence. Figure 3-1 shows the basic parameters in bench blast design. Bench height and hole diameter are often governed by the mine site through seam thickness and drill availability. Burden and spacing are designed by a blasting engineer and alter dependent on final use. Stemming is vital to contain the explosive energy within the rock mass for fragmentation as opposed to escaping out the top of the blast hole. This area, however, has no explosive charge and produces larger fragments as a result.

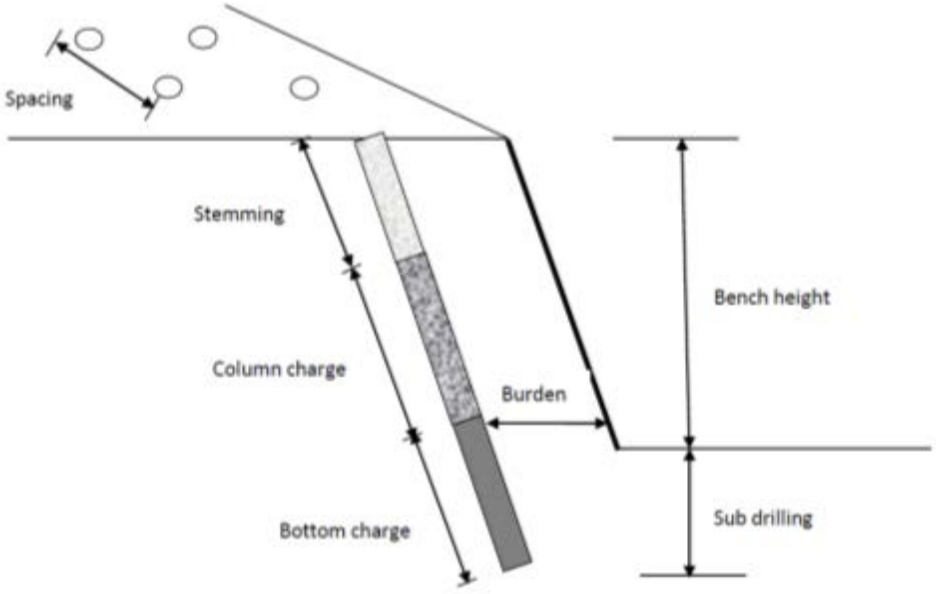

.

Figure 3-1 Parameters of blast design (EPC, 2010)

Once a charge has been detonated, a number of processes work in unison to create the overall fragmentation process: stress waves, gas expansion and reflection. Huge quantities of stored energy are released. This energy produces a high pressure pulse, subsequently generating a compressive strain pulse in the surrounding rock, creating crushed rock in the immediate area that moves outward from the blast hole. This pulse travels radially, reducing amplitude with distance. When a distance is reached that no further breakage is possible, the pulse travels a further seismic distance. On impacting a free face the seismic wave undergoes a 180° phase change and is reflected back to the rock as a tensile rarefaction wave due to the sudden drop in pressure to negative values. Since rock is weaker in tension than compression, primary failure cracks develop and produce spalling at the free face. Fragmentation by tensile fracture is necessary for breaking the hardest rocks but compressive forces can break softer rocks. Reflection of stress waves does not just occur at the free face but is influenced by fractures and joints within the rock mass. These distances are a lot harder to quantify.

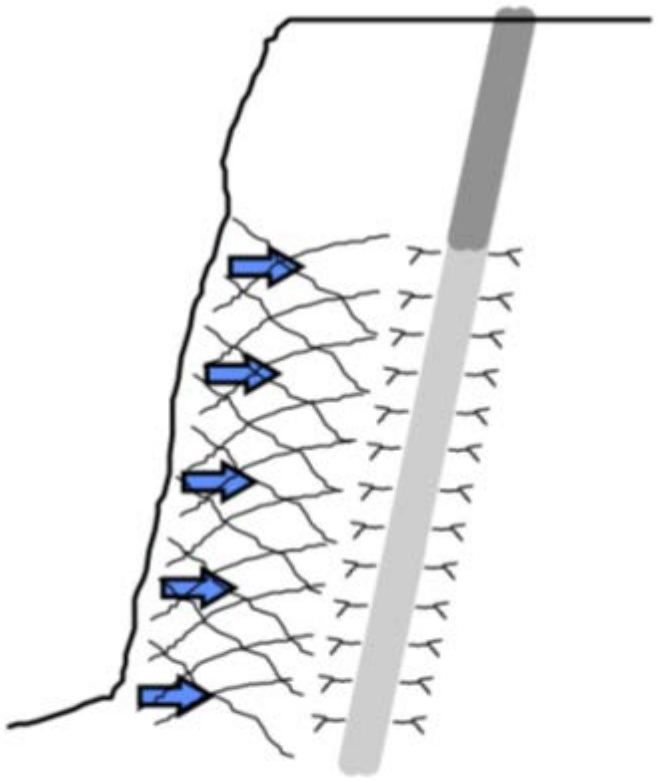

Figure 3-2: Reflection of shock waves at the free face (EPC, 2010)

The final stage in the process is that of gas expansion, breakage in this stage is much slower. After the sudden release of stored energy there is a large outbreak of gas at high temperature and pressure. Thrust energy describes the work done by the gases produced by detonation (Figure 3-3). The high temperature gas dissipates through the primary cracks, elongating them. The gas pressures are sustained much longer than the detonation pressures and dissipate only when a significant phase change is reached, such as the free face. The gas leaving the face pushes the material out in a bow like shape (Figure 3-3) demonstrates how the rock reacts to the gas phase. The degree of fragmentation and angle of bow are dependent on the properties of the burden rock.

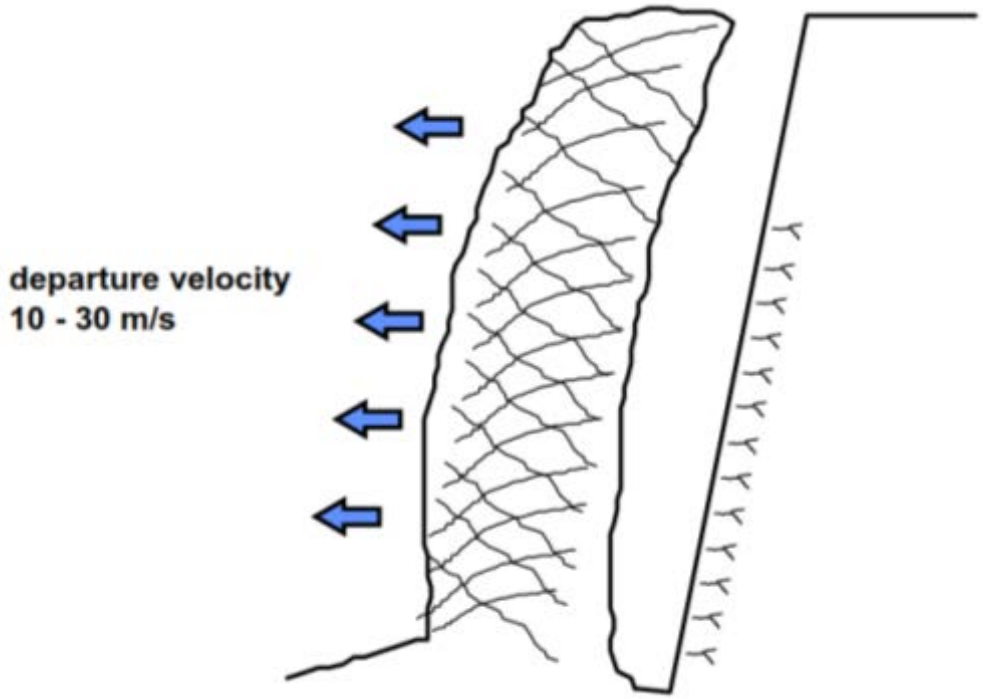

Figure 3-3: The gas phase (EPC, 2010)

3.1.1 Optimized Fragmentation

Blast design would be simple without consideration for the environment or the final use of the material, but this is not the case. An optimized blast design incorporates maximizing your fragmentation for final use, minimizing environmental considerations whilst keeping costs reasonable. Often, final use for fragmented material used in mining and construction is as an input for a crusher so minimizing crusher energy and throughput is important. Large boulders might be beneficial for dam construction or sea defenses. When overburden or fill material is being blasted, a range of sizes might be beneficial. The degree of fragmentation is influential on the overall process and the start of a well-known term 'mine to mill' (Kanchibotla and Valery, 2010) governing the overall costs to the mine. Fragmentation change is influenced greatly by changing explosive quantity, its distribution and the rock structure. The latter, rock structure, is quite clearly site dependent, but if the energy imparted by the explosive is used to its full potential using the same quantity of explosives through additional stress wave interactions between

consecutive holes or the same hole, fragmentation could be increased with minimal cost added. This concept is the premise of this dissertation. Optimum fragmentation is documented extensively in literature, (Katsabanis and Liu (1996), Rossmanith (2002), Vanbrabant and Espinosa (2006) Bauer, (k2014)) referring to a specific site. Confusion arises in literature through the use of the term increased fragmentation used interchangeably. A common definition of this term is not easy to determine. Often, increased fragmentation is referred to as a decrease in the p50 (size where 50% of particles through a sieve) particle size but this might not always be beneficial. A decrease in the p50 size can occur through a binomial distribution of fines and larger boulders, which is not necessarily beneficial to all end uses.

Blasts are initiated with a detonator. Traditional detonators consist of a specified length of pyrotechnic element initiated by either an electric current of shock tube. Inaccuracies are observed with these detonators because of the drastic difference in burn rate of the pyrotechnic element. More recently electronic detonators are being used that contain a microchip that can be programmed in millisecond increments.

3.2 Fragmentation Modeling and Limitations

A number of models have been established to predict size distributions from specific blast designs. Predictions are made either through empirical or mechanistic modeling. Empirical modeling assumes finer fragmentation from higher energy input whilst mechanistic modeling tracks the physics of detonation and the energy transfer for specific blast layouts. Quite clearly the mechanistic model requires more data so is more difficult to apply on a day to day basis. Therefore, empirical models are most often used for the prediction of fragmentation size. One of the first empirical fragmentation models with respect to blasting is the Kuz-Ram model. The model was established by Cunningham in 1983 as an easy method of estimating fragmentation based on geometric parameters of the drilling and blast design. A mean size is calculated using blast parameters (Kuznetsov, 1973) and the fragmentation spread is based on an adapted version of the Rosin-Rammler equation. Four equations are required for the model:

Adapted Kuznetsov equation:

$$x_m = AK^{-0.8}Q^{\frac{1}{6}}\left(\frac{115}{RWS}\right)^{\frac{19}{20}} \quad (3\text{-}1)$$

Where x_m = mean particle size (cm); A = rock factor; K = powder factor (kg/m^3); Q = mass of explosive in the hole (kg); RWS = weight strength relative to ANFO, 115 being the RWS for TNT

Rock Factor, A

$$A = 0.06(RMD + JPS + JPO + SGI + HF) \quad (3\text{-}2)$$

Table 3-1: Rock factor parameters (Lilly, 1983)

Rock Mass Description (RMD)	Powdery/Friable	10
	Blocky	20
	Totally Massive	50
Joint Plane Spacing (JPS)	Close (<0.1m)	10
	Intermediate (0.1 to 1m)	20
	Wise (>0.1m)	50
Joint Plane Orientation (JPO)	Horizontal	10
	Dip Out of Face	20
	Strike Normal to Face	30
	Dip into Face	40
Specific Gravity Influence (SGI)	SG in tonnes/m^3	25(SG-50)
Hardness Factor (HF)	Elastic Modulus(GPa)/3	1-10

Adapted Rosin-Rammler equation:

$$R_x = exp\left[-0.693\left(\frac{x}{x_m}\right)^n\right] \quad (3\text{-}3)$$

Where R_x = mass fraction remained on screen opening x; n = uniformity index, between 0.7 and 2.

Uniformity equation:

$$n = \left(2.2 - \frac{14B}{d}\right)\sqrt{\left(\frac{1+S/B}{2}\right)}\left(1 - \frac{W}{B}\right)\left(abs\left(\frac{BCL-CCL}{L}\right) + 0.1\right)^{0.1}\frac{L}{H} \quad (3\text{-}4)$$

Where B = burden (m); S = spacing (m); d = hole diameter (mm); W = standard deviation of drilling precision (m); L = charge length (m); BCL = bottom charge length (m); CCL = column charge length (m); H = bench height (m). (Cunningham, 1983)

The model is simple to use due to the ease of access to data for all parameters involved and does not involve a lengthy image analysis process, unless of course you want to validate it. Despite this, it has been scrutinized for its lack of inclusion of all parameters involved with rock fragmentation and an underestimation of the prediction of fines (fragments less than 50mm). Lownds (1983) identified that the uniformity parameter is not influenced by mechanical properties of the rock or characteristics of the explosive. Fragmentation prediction by Cunningham (1983) assumes that a single distribution of pre-existing discontinuities are present within the rock mass and that tensile failure is the main mechanism of failure. A tensile stress field is created around each blast hole extending radial cracks as it initiates. The interaction between radial cracks from different blast holes and the free face create rock fragments.

Rollins (1990) acknowledged that explosive properties and mechanical rock properties are not fully considered within the original Kuz-Ram model, only the drilling pattern and general rock mass factors based on an original model by Lilly (1986) (Table 2-1). He developed a separate model that takes into account different tensile breakage mechanisms that occur due to explosive interaction with the rock. Breakage mechanisms identified include the main breakage area, secondary breakage and a back break area, shown in Figure 3-4. The boundary of the main breakage area is found from the magnitudes of the strain from the tensile stress waves and the tensile strength of the rock. The secondary breakage area is determined by tensile stress wave reflections at discontinuities and interactions from adjacent boreholes. The back break area is that beyond the main breakage area where reflected tensile waves no longer break the rock. A rock volume for the main breakage area is calculated for each hole and individual mean fragmentation sizes and a fragmentation distribution for each borehole are calculated using equations 1 and 3, respectively; an average is taken of all boreholes calculated. To calculate the

breakage area, more in depth analysis of the specific explosive used and individual rock parameters around each blast hole are required. Comparing this model to field data showed excellent results for the fine end of the spectrum, far more accurate than using the total volume of rock as in the original model by Cunningham (1983); however, the model is based on a small scale, ideal test. (Rollins, 1990)

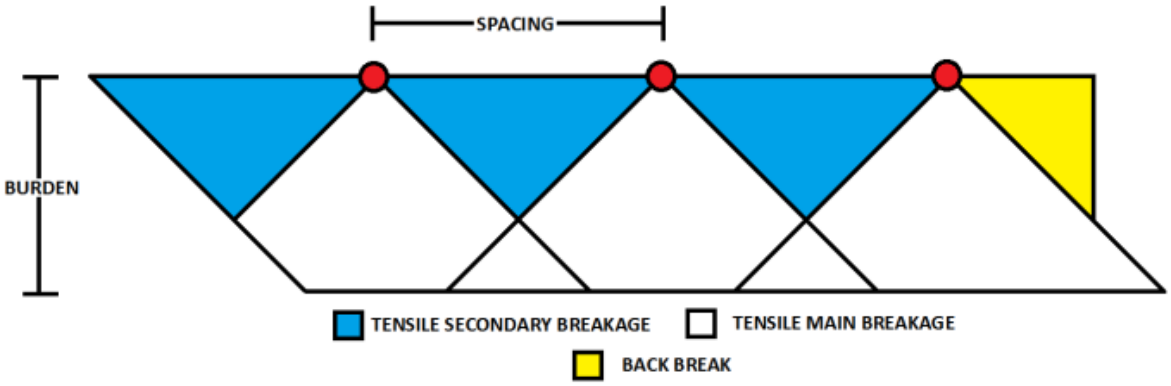

Figure 3-4: Breakage mechanisms identified by Rollins (1990).

The Rollins model still only takes into account tensile breakage, in reality, there are two very different mechanisms that cause rock fragmentation, both tensile failure, and compressive shear failure (Figure 3-5). Compressive shear failure occurs close to the blasthole and creates much smaller particles. In hard rock blasting, fragmentation models such as the Kuz-Ram give a good result since the effects of compressive shear failure are minimal. Softer rocks, however, have a significant amount of compressive shear failure and therefore this parameter should be taken into account in the prediction of fragmentation size. This also explains the underestimation of fines in the original Kuz-Ram model. Djordjevic (1999) developed a two component model for cases where fragmentation of the given rock volume occurs due to two different mechanisms. The d_{50} size calculated from equation 3-1 is used for the coarse distribution of sizes. The mean size of fines, typically under 50mm, are considered separately. The model gives a better estimation to the full spectrum of fragmentation sizes. The two separate d_{50} sizes are input into a modified version of equation 3 to give:

$$R_x = 1 - (1 - F_c).exp\left[-0.693\left(\frac{x}{a}\right)^b\right] - F_c.exp\left[-0.693\left(\frac{x}{c}\right)^d\right] \quad (3\text{-}5)$$

Where a and c = mean fragment sizes in the tensile and compressive failure regions, respectively; b and d = uniformity coefficients in the tensile and compressive failure regions, respectively and F_c = the total mass of rock failed by shear compressive strength, given by:

$$F_c = \frac{M_o}{M} \tag{3-6}$$

Where M_o = mass of rock failed in compression and M = total mass of rock per blast hole.

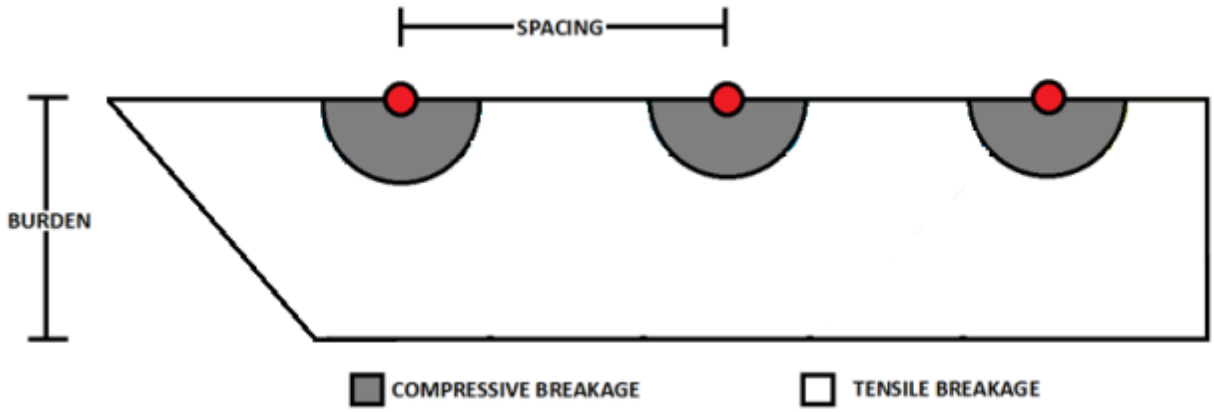

Figure 3-5: Compressive and tensile stress rock breakage

Kanchibotla et al (1999) hypothesize that fines are produced by the crushing action of the rock adjacent to the blast holes. A cylindrical volume, similar to that shown in Figure 3-5 as compressive breakage, is determined by calculating the point at which radial stress around the blast hole exceeds the dynamic compressive strength of the rock. The distribution of the coarse fraction (>1mm) and the fine fraction of the rock are considered separately. Predictions using this model have been used on several mine sites. The resulting size distributions on the fines zone are far superior to those from the original Kuz-Ram model (Kanchibotla, 1999). Ouchterlony (2004) incorporates a third parameter to account for the upper limit cut-off of block sizes from the original model giving correlation coefficients with sieved data of at least 0.997.

Fragmentation distribution can also be analyzed through photographic image analysis. A number of computer models have been developed including, but not limited to, GoldSize, (Kleine, 1997) BLASTFRAG (Exedaktylos, 1989) and WipFrag. Kanchibotla et at

(1999), discuss the systematic bias involved with image analysis due to the coarse fragmentation zone on the surface of the muck pile caused by the stemming zone where no explosive charge is present (Figure 3-6). Fragmentation in this zone is due to gas heave from the underlying explosive charge and secondary breakage through crushing and grinding during movement. To avoid sampling bias, images need to be taken at regular intervals throughout the digging process, possibly hindering the shovel and truck productivity. An image based software system needs to be able to distinguish between different particles, usually by identifying particle boundary pixels in a grey level scale. It is easy to confuse shadows with particle separation and the fine portion of the scale is nearly impossible to predict. Due to this, pre-processing work is often required to outline separate rock particles and identify areas of fines. Fines are not fully taken into account through image analysis; first, they are not always present on the surface due to settling, wind or rain, and secondly, individual fragments are too small to segregate due to image resolution limitations. Since fines are not often of high interest when looking at fragmentation distribution, they are often eliminated from the final size distribution in image analysis, but this is the specific users' choice.

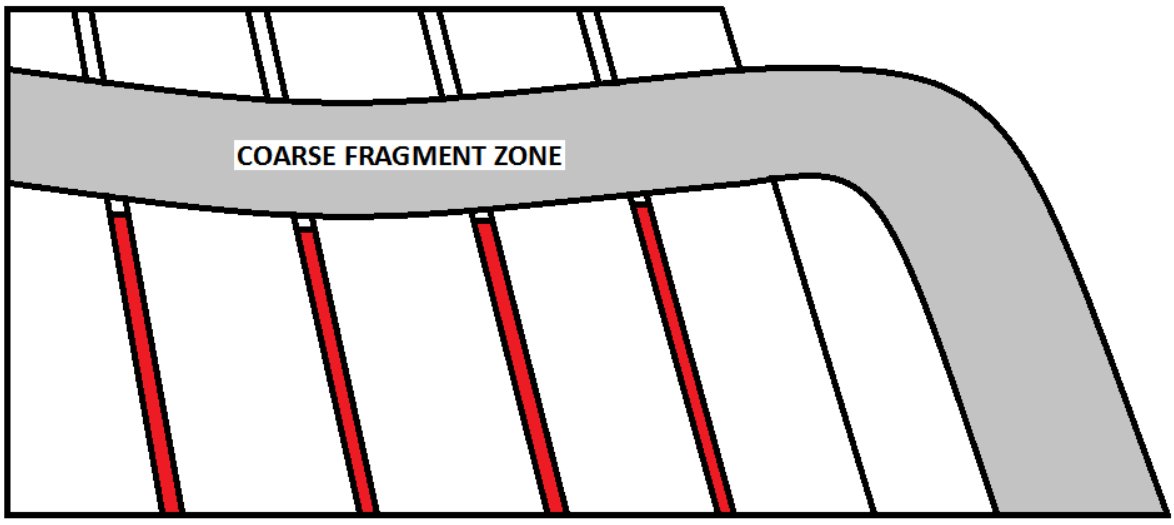

Figure 3-6: Coarse fragmentation zone from a blast. (Kanchibotla, 1999)

When looking at Figure 3-6 and the consideration for the coarse fragmentation limitation for image analysis, it is apparent that the coarse fragmentation zone is not taken into account for the Kuz-Ram model. It has been discussed that the column charge (red in

Figure 3-6) causes two types of failure, compressive and tensile, where the tensile fraction is considered in the original model. Attempts have been made to include the fines fraction into the model through two and three component models by Djordjevic (1999) and Ouchterlony (2004), respectively. However, no consideration for the large end of the size distribution has been considered.

Numerous discrepancies in the Kuz-Ram model have been identified and minor improvements to this model implemented. Each, however, brings with it additional parameters to input, taking it from a simplistic model to a complicated one displaying only minute differences. What has never been included in such a model is timing.

3.3 Theory of detonation and shock waves

A complex sequence and interaction between multiple stress waves occur when any one blast hole is initiated in rock. The main premise in mine blasting it to utilize these stress waves for efficient fragmentation of the rock mass, as opposed to being wasted through ground or air vibrations. Stress wave propagation is the first step in the fragmentation process, preconditioning the often strong rock mass with extended fractures in which the strong gas pressure can expand. The most prominent difference between the detonation wave and shock waves named throughout this dissertation is that a detonation wave only travel through an explosive mixture, often at a constant rate due to the chemical composition of the explosive mixture until the entire column has detonated. A shock wave is resultant of a detonation wave and travels through the surrounding medium, rock, air or water, dissipating with distance. The detonation wave has an associated shock wave it propagates but rather than dissipating with distance, the shock wave is constantly being pushed by the chemical detonation.

3.3.1 Detonation waves

Detonation waves travel as energy is released from a chemical reaction, originating from a detonation point. In an ideal detonation, the velocity of detonation (VOD) is the maximum possible velocity when all components in the chemical reaction react fully. VOD can be measured easily with traditional methods such as the D'autriche Method (Figure 3-7). Essentially, an explosive cartridge for which you want to determine the VOD has two ends of a line of detonating cord inserted into it. Detonating cord is used

as it is known to have a constant, repeatable, ideal VOD that's well documented by manufacturers (PRIMACORD, Cordtex etc.). The center of the detonating cord is placed over a lead plate and the exact center point marked. Upon detonation of one end of the explosive column, the two ends of the detonating cord are initiated independently. The point at which they collide leaves a mark on the lead plate. The difference in distance between this and the measured center point of the detonating cord, along with the known VOD of the detonating cord are used to determine the VOD of the cartridge. The method has in the past worked well as a low technical method of determining the VOD of explosives (Kosanke et al, 2012). A significant downfall for mining explosives is that the explosive has to have a high enough shock to initiate the detonating cord, which is not possible with a small diameter charge of Ammonium Nitrate/Fuel Oil (ANFO), for example. A more common method of calculating VOD is with a VOD probe and data acquisition system such as an MREL Datatrap.

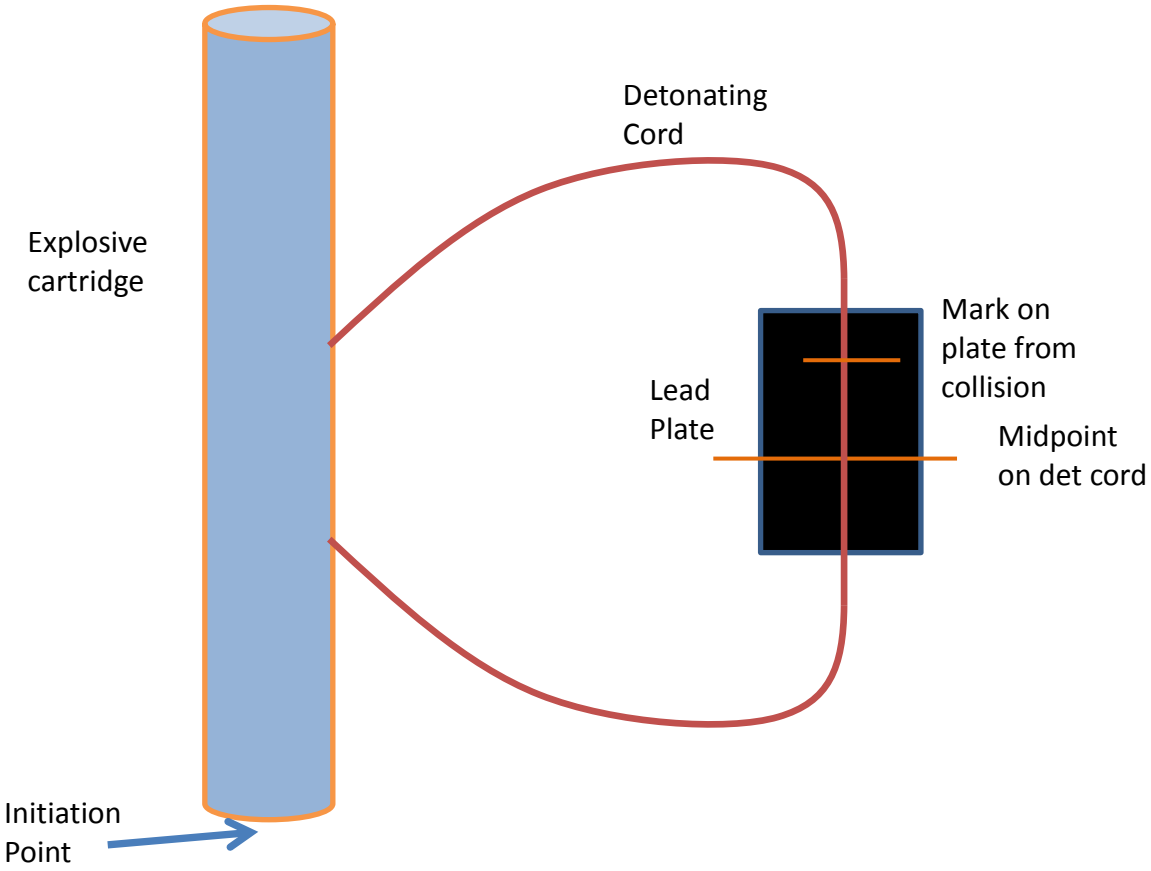

Figure 3-7: D'autriche Method for determining VOD of explosive

Ideal detonation, however, is not a reality in mining explosives. As an oxygen balanced explosive, such as ANFO, detonates, a large quantity of expanding hot gases is produced. In an ideal situation only hot steam, carbon dioxide and nitrogen are produced.

$$3NH_4NO_3 + CH_2 \rightarrow 3N_2 + CO_2 + 7H_2O$$

In reality, efficient blasting practice is only possible with sufficient confinement and priming. Furthermore, the explosive products are often contaminated with water and drill cuttings, all of which affect the explosives quality and chemical kinetics. This results in non-ideal explosive reactions and production of toxic gases: nitrogen dioxide, nitric oxide and carbon monoxide (NO_2, NO and CO), as well as a reduction in energy imparted onto the rock mass. Explosives are often contaminated with ground or rain water, leading to increased levels of NOx gases through the breakdown of ammonium nitrate into nitrate and ammonia in solution. The desensitized solution will not fully decompose when detonated, producing non-ideal products. Under and over fueling an explosive mixture results in positive and negative oxygen balances, respectively. A positive oxygen balance will produce more NOx gases, whilst a negative oxygen balance will produce more CO.

Effect of over fueling ANFO is:

$$2NH_4NO_3 + CH_2 \rightarrow 2N_2 + CO + 5H_2O$$

Effect of under fueling ANFO is:

$$5NH_4NO_3 + CH_2 \rightarrow 4N_2 + 2NO + CO_2 + 7H_2O$$

Nitric oxide is unstable in air and reacts with oxygen to produce the more toxic nitrogen dioxide, which can be seen after a blast by the generation of an orange/brown cloud (Onederra, 2012):

$$2NO + O_2 \rightarrow 2NO_2$$

The degree to the non-ideal state of an explosive is dependent highly on the rate of detonation and degree of confinement. Selecting the correct explosive for a specific site is crucial. Mining explosives, typically ANFO, Emulsion, water gels, or a blend, have a critical diameter under which they do not fully detonate, reducing the effectiveness of the

explosive. If the VOD is lower than its full potential, so is the shock wave velocity reaching the blast hole wall and travelling through the rock mass affecting the fragmentation.

3.3.2 Shock waves

Upon detonation of a blast column, a strong shock wave is emitted; this quickly decays into an elastic stress and in the far field is responsible for initial ground vibrations (Broek 1988; Clark 1987). When the shock wave reaches the borehole wall the fragmentation process begins. This shock wave, which starts out at the velocity of the explosive, decreases quite rapidly once it enters the rock and in a short distance is reduced to the sonic velocity of that particular rock. The distance at which this occurs depends on the rock blasted and the VOD of the explosive, as well as other contributing factors such as pore pressure or fractures in the rock. At those areas surrounding the blast column, radial cracks form after a small delay. The outgoing shockwave travels through these cracks radially, creating a tangential stress. This pressure is compressive, but since rock is weaker in tension, it is the tensile wave that typically causes the rock to break. When the stress reaches a free face, it reflects back as a tensile wave due to the change in density, causing further breakage. (Cook, 1974).

The velocity of a shock wave through a medium changes due to the relationship between stress and strain and whether it occurs in the plastic or elastic region. In the elastic region, pressure and density are linearly related and the sound velocity proportional to this ratio. Beyond this, wave velocity increases with pressure or density and is not linearly proportional. Particle velocities also increase with pressure. The wave velocity continues to increase until it approaches a straight vertical line; it is at this point that the wave becomes a shock wave. The three velocities present, sound, particle and shock, do not all increase the same rate. Shock velocity increases at a rate faster than that of the particle velocity; it can be explained in simple terms as the inclusion of numerous particle velocities that are occurring at one time. An excellent depiction of this by Cooper (1996) is shown in Figure 3-8 using popsicle sticks of width ‘W’ separated by the same width ‘W’.

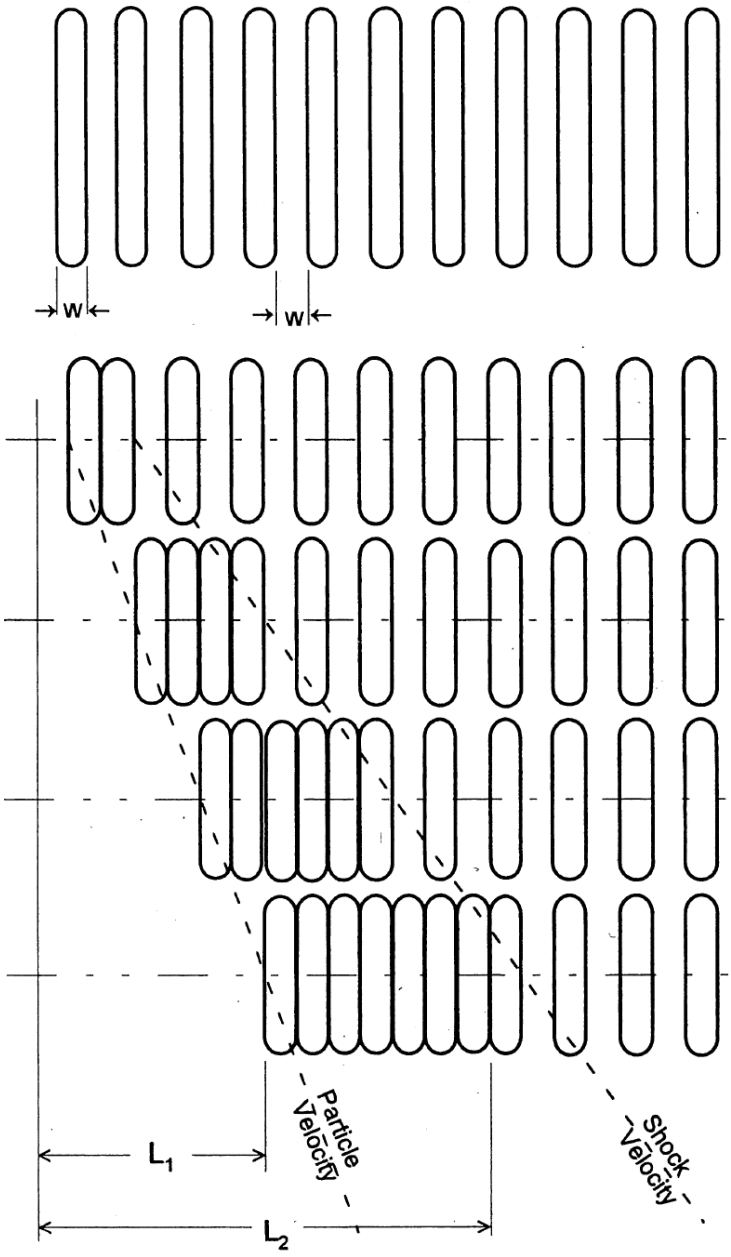

Figure 3-8: Shock and particle velocity portrayal (Cooper, 1996)

When considering a square wave, like that in Figure 3-9, the front of the shock wave is already in shock. The velocity at the back of the wave is the sum of the particle velocity and the wave speed and appears vertical (1. In Figure 3-9). The velocity increases at a faster rate at the back of the wave since it is approaching a medium of higher density and pressure as a shock front has already passed through. This velocity eventually catches up

with the front (4. In Figure 3-9), the velocity at this portion, the rarefaction wave, is the greatest velocity the wave will possess. Beyond this point, this rarefaction wave is reaching unaffected medium and will eventually slow to the velocity of the rock mass. (Cooper, 1996)

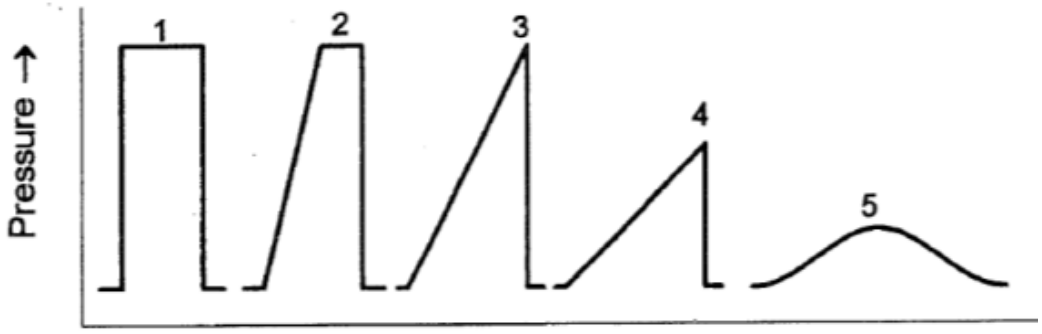

Figure 3-9: Progression of a shock wave (Cooper, 1996)

As a shock front travels through a medium, there is a sudden change in state across the shock front (U) to the particle velocity (u), density (ρ), internal energy (e) and pressure (P), not a gradual increase. They essentially change from an unshocked front to a shocked front. Figure 3-10 demonstrates this process in a simple diagram across a square shock front where the subscripts depict the state in front of and behind the shock front.

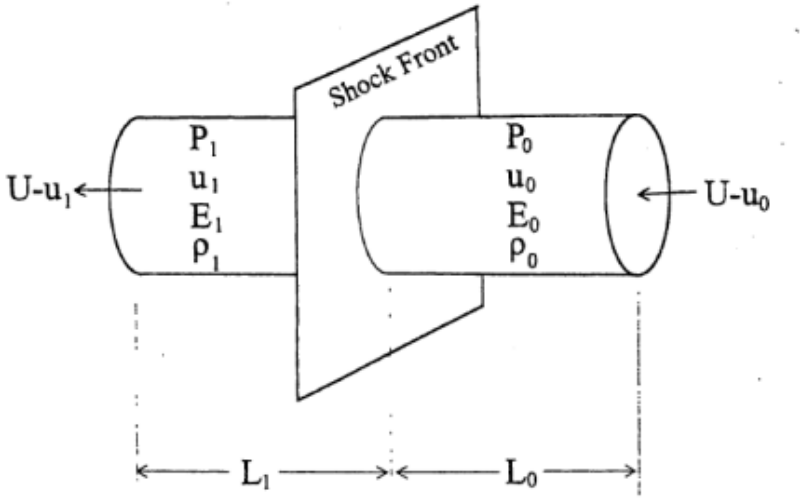

Figure 3-10: Mass moving through a shock front (Cooper, 1996)

Rankine-Huginiot jump equations for mass, momentum and energy balances describe the relationships either side of a shock front.

$$mass\ equation: \frac{\rho_0}{\rho_1} = \frac{U-u_0}{U-u_1} = \frac{v_0}{v_1} \quad (2\text{-}7)$$

$$momentum\ equation: P_1 - P_2 = \rho_0(u_1 - u_0)(U - u_0) \quad (2\text{-}8)$$

$$energy\ equation: e_1 - e_0 = \frac{P_1u_1 - P_0u_0}{\rho_0(U-u_0)} - \frac{1}{2}(u_1^2 - u_0^2) \quad (2\text{-}9)$$

Three additional relationships explain a series of empirical relationships. the Huginiot planes; the Shock Velocity – Particle Velocity (*U*-*u*), the Pressure – Specific Volume (*P*-*v)* and the Pressure – Particle Velocity (*P*-*u*) planes. These such relationships, between the basic shock parameters already explained, are called Equations of State (EOS).

The *U*-*u* plane has been found to have a linear relationship and related using equation 2-10:

$$U = C_0 + su \quad (2\text{-}10)$$

Where C_0 is the y intercept, or bulk sound speed and s is the slope (Figure 3-11). Values for many materials are available from experimental data (Cooper, 1996).

The *P*-*v* plane is found by combining the *U* – *u* plane with the mass and momentum equations and eliminating the unwanted parameters, *u* and *U*. Assuming P_0 and $u_0 = 0$:

$$P = C_0^2(v_0 - v)[v_0 - s(v_0 - v)]^{-2} \quad (2\text{-}11)$$

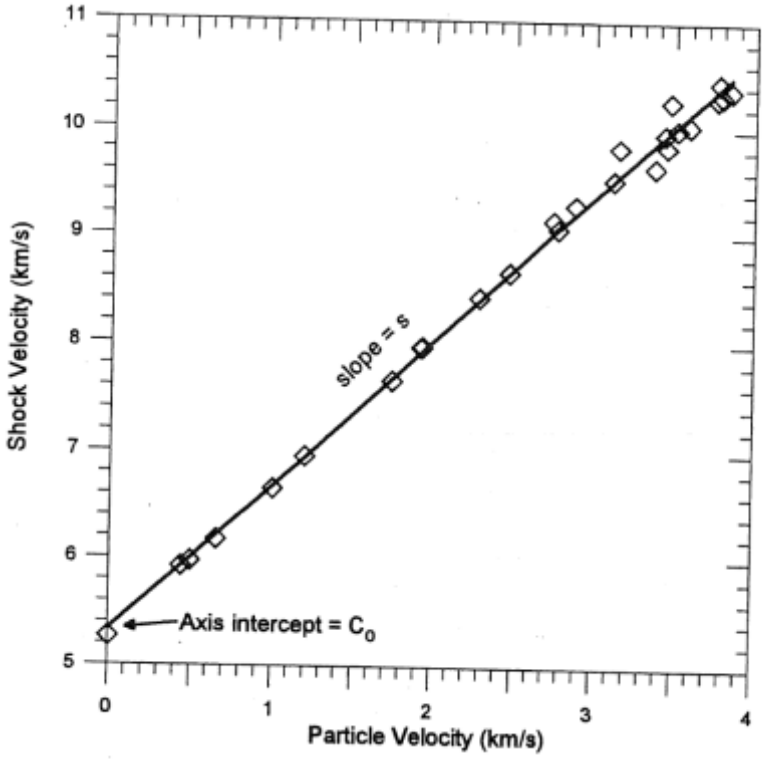

Figure 3-11: U-u Huginiot experimental data for aluminum, (Cooper, 1996)

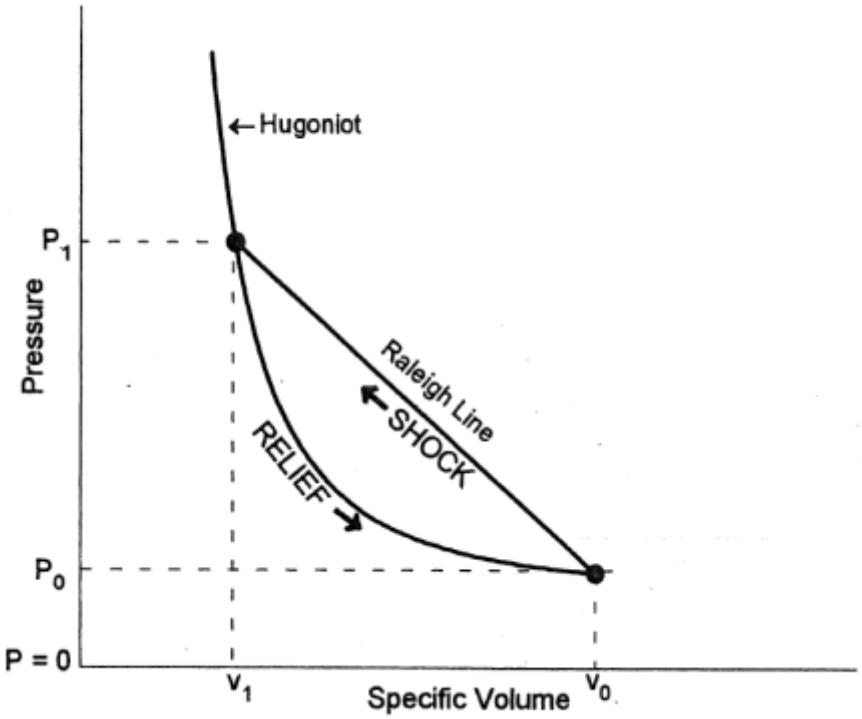

Figure 3-12: *P-v* Huginiot (Cooper, 1996)

Figure 3-12 shows the P-v Huginiot. Joining the initial and final states of the Huginiot gives the Raleigh Line, representing the jump condition at the shock front. Equation 2-12 gives the equation of the Raleigh Line. The shock velocity can be calculated if the initial and final P-v states are known.

$$p_1 - p_0 = \frac{U^2}{v_0} - \frac{U^2}{v_0^2} v_1 \tag{2-12}$$

The *P-u* Plane EOS can be found from the momentum and *U-u* Huginiot equations. Again, assuming P_0 and $u_0 = 0$:

$$P_1 = \rho_0 u_1 (C_0 + s u_1) \tag{2-13}$$

All the equations of state thus far describe a moving shock front hitting a stationary object, the unshocked state at P_0 and $u_0 = 0$. The premise of this dissertation is on two colliding shock fronts, so the material the shock is entering is already in motion. At this point Lagrangian and Eulerian transforms can become clear. A shock front attenuating an unaffected medium can be described with Lagrangian equations, when a shock front attenuates a material already in motion the Eulerian equation becomes important. For a material already in motion, the Lagrangian equation 2-13 becomes the Eulerian Equation 2-14 (Cooper, 1996):

$$P_1 = \rho_0 C_0 (u_1 - u_0) + \rho_0 s (u_1 - u_0)^2 \tag{2-14}$$

A series of P-u planes are required for the Eulerian state, the initial particle velocity for each one unique. (Figure 3-13)

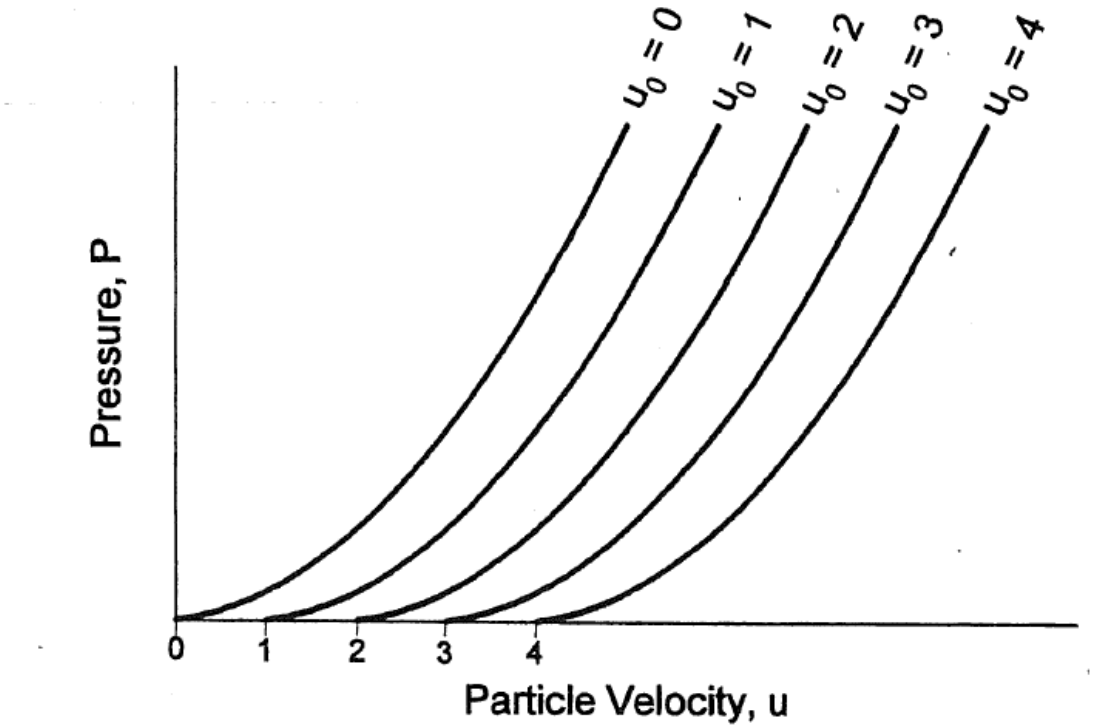

Figure 3-13: Eulerian P-u Huginiot (Cooper, 1996)

Ernest Mach in 1886 discovered the now well-known relationship between the speed of a body moving through air and the speed of sound in air, often used for airplane or ballistics, known as the Mach number. Rossmanith et al (1998) carried out a number of tests in Plexiglas and numerical models to conclude that this same relationship occurs in solids between the detonation velocity and either the P-wave (pressure) or S-wave (Shear) velocity of the rock mass. P and S waves are to types of body wave produced by an explosion that travel through the rock mass. P-waves have a higher velocity and travel in the direction of the detonation, compressing the particles back and forth in its path. An S-wave, or transverse wave, moves in a direction across that of the detonation, shearing and rotating it, moving at a much slower speed than the P-wave.

The Mach number determines the angle of the shock front, known as a Mach angle (Equation 2-15).

For a supersonic velocity detonation, the Mach angle in air can be calculated by:

$$sin\alpha = \frac{a}{v} \quad \text{or} \quad sin\alpha = \frac{1}{M} \tag{2-15}$$

Where α is the Mach angle; a is the sonic velocity; v the detonation velocity and M the Mach number.

Muller et al (2013) states that to choose the right explosive you much determine the detonation velocity and the P and S wave velocities. Using the relationship established by Rossmanith et al (1998), the higher the Mach number, and the smaller the Mach angle, the more intense the fragmentation process will be. This, as explained by Muller et al (2013), increases the fragmenting cutting effect of the shock front. Formulae used in the calculation are:

P and S Mach numbers:

$$M_P = \frac{C_d}{C_P} \quad or \quad M_S = \frac{C_d}{C_S} \tag{2-16}$$

P and S Mach angle or shock front angle:

$$\sin \alpha_P = \frac{C_p}{C_d} \quad \text{or} \quad \sin \alpha_S = \frac{C_S}{C_d} \tag{2-16}$$

Where c_d is the detonation velocity of the explosive; C_P the P-wave velocity of the rock; C_S the S-wave velocity of the rock and α the shock front angle.

Blair (2009), however, states that the extent of the P and S Mach waves only exist for a short duration and volume, where the detonation column is being consumed. Blast holes would therefore have to be very close together for an interaction to occur, or the waves slowed to such an extent that any additional increase due to a collision would be minimal.

3.3.3 Interaction of Shock Waves in air

The theory of colliding shock waves in air or a shock wave attenuating a solid structure is well understood and documented in the likes of Cooper (1996) and Forbes (2012). When two waves of unequal amplitude approach one another, Cooper (1996) states that when they meet they produce a much higher pressure that is reflected back. The final reflected pressure has a magnitude greater than that of the sum of the two initial pressures. If the Huginiot were a straight line then the resultant pressure would be the sum of the initial pressures, but since they curve increasingly upwards the resultant pressure becomes

greater than that of the initial pressures. All shock wave discussion in Cooper (1996) is in two dimensions. Figure 3-14 demonstrates a simple depiction of two unequal shock waves travelling towards each other (Cooper, 1996). The pressure asserted by the two waves essentially combine, increase due to the particle velocity already in play and two equal higher Pressure waves reflect back in the opposing directions.

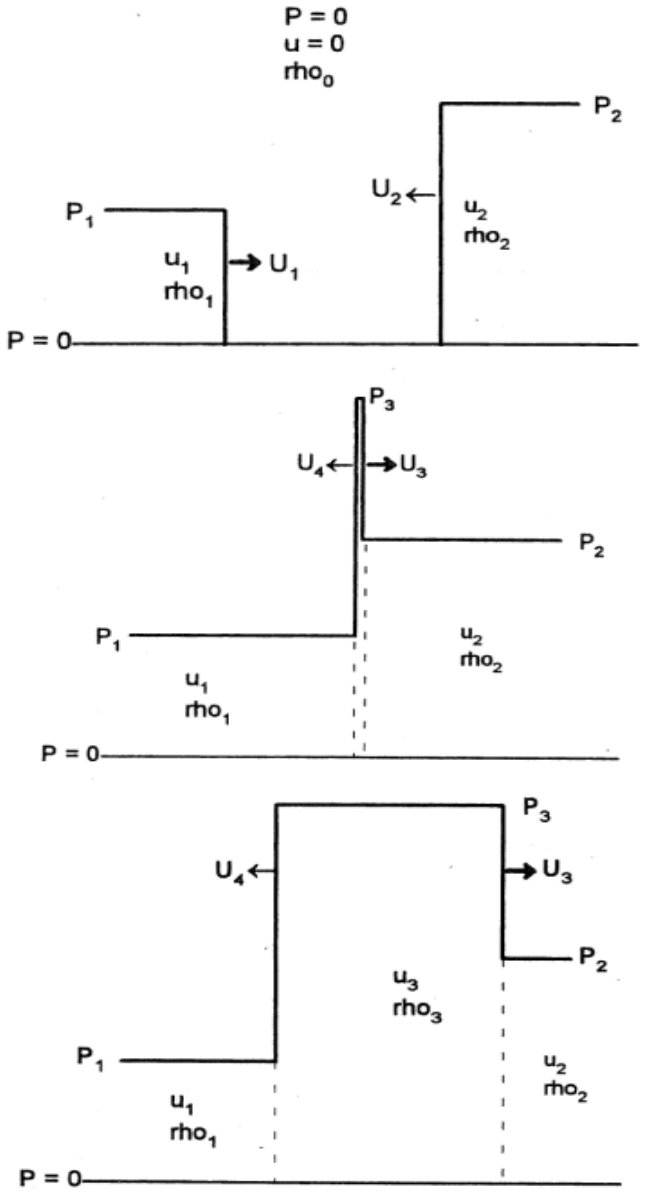

Figure 3-14: Pressure – Distance diagram for two shock waves of unequal amplitude (Cooper, 1996)

3.3.4 Colliding Shock Waves in Strata

Measuring and observing two shockwaves collide in strata is a difficult feat. It is yet to be fully established whether the waves would reflect back, increasing in magnitude, pass through each other and magnitudes of each wave add together or whether any increase is observed. Cook (1974) states that the laws of shock wave propagation in media other than that of air or water aren't well known at short distance. Considerable data is available at greater distances through the use of seismographs and ground vibration analysis. It is assumed that the same basic relationships occur, but how the additional parameters of shear and tensile strengths, density and unavoidable fractures in the rock mass, play in the process is more difficult to quantify. Yamamoto et al (1999) state that when considering two adjacent blast holes, maximum fragmentation is achieved in those sections between the blast holes, where the two tensile trailing sections of the blast waves meet. When two of shock waves collide and no free face is present, the tensile waves will meet, increase in magnitude, and form cracks. Yamamoto et al (1999) propose that for simultaneously detonating charges, this happens at the mid-section of the spacing of these blast holes; for a delayed charge it occurs away from the centerline. No experimental data is available on this, only theoretical. This delay has a very short range of only a few milliseconds dependent on the speed of sound in the rock being blasted. Therefore delay timing has to be selected appropriately for any interaction to occur.

The interaction of these stresses has been difficult to measure as the pressure that builds up in the borehole depends not only upon explosive composition, but also the physical characteristics of the rock. Strong competent rock will result in higher pressures than weak, compressible rock. Rossmanith (2003) discusses how the delay time, wave speed in the rock mass, shape of the wave pulse and acoustic impedance mismatch have become decisive parameters in modern day advanced blast design. As a blast hole detonates it creates a leading compressive pulse and a trailing tensile pulse, the length of this is dependent on the explosive type and type of rock. The wave speed can vary between 6560 feet per second (ft/s) for soft sandstone to 21,320 ft/s for granite (Cook, 1974). Maximum fragmentation is achieved in those sections where the two tensile trailing sections of the blast wave meet. When two adjacent blast holes of spacing 's' are considered, the elementary event is the interaction between the two stress waves: P_1-P_2,

S_1-S_2, P_1-S_2 and S_1-P_2. In the close vicinity of the blast, the P and S waves will overlap, but will separate with distance from the blast due to their varying speeds. Figure 3-15 shows a Lagrange diagram in 1 dimension between the stress wave interaction when two holes are detonated simultaneously. Subscripts F and E denote the front and end of the compressive waves, respectively. (Rossmanith, 2003)

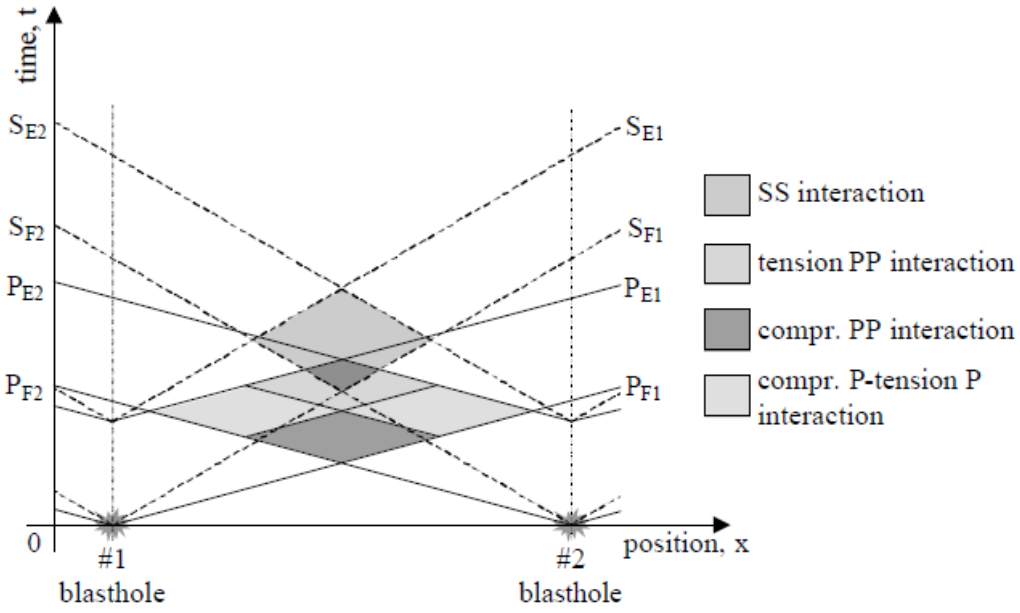

Figure 3-15: Lagrange diagram showing interaction of stress waves emerging from two simultaneously detonated blast holes. (Rossmanith, 2003)

Identifiable interactions are:

1) $P_1^+P_2^+$ Interaction of the leading compressive parts of the P-waves
2) $P_1^-P_2^-$ Interaction of the trailing tensile parts of the P-waves
3) S_1S_2 Interaction of the S-waves
4) A range of mixed wave interactions, e.g. P_1S_2 of the P_1 wave of blast-hole #1 with the S_2 shear-wave from blast-hole #2.

If the detonation of the second wave is delayed, the above regimes will move closer to the delayed blast hole, consequently controlling the fragmentation pattern. Conversely, if the stress waves occur in the center of the two blast holes, overlapping at the greatest

magnitude, the potential for fragmentation is increased. Longer wave pulses can also be obtained using an explosive with a lower VoD and brisance. These explosives are usually associated with larger volumes of produced gas, generating differing opinions on the precise cause of the enhanced fragmentation. Rossmanith's Theory has come under scrutiny for being too simplistic. Experimental tests by Katsabanis et al (1996, 2006, 2014) and Johansson and Ouchterlony (2013) do not agree with the interaction defined by Rossmanith (2003). Model simulations in LS-DYNA by Sjoberg et al (2012) also disagree with the Rossmanith Theory, concluding greater fragmentation is achieved at greater time delays where no wave interaction occurs. Further detail on these tests is explained in sections 3.4.2 and 3.5.1.

3.3.5 Shock Wave theory for Pre-splits

A widely referenced source for all blasting engineers is that of the International Society of Explosives Engineers (ISEE) Handbook. This is a book that "represents more than 185 years of DuPont and ETI blasting expertise" (ISEE, 1998). Figure 3-16 is taken from the 18th edition of the ISEE handbook regarding the theory of presplitting (ISEE, 2011). A presplit is a common blast design used to control highwall stability and for road cuts through hard rock. It involves a single row of blast holes with a low quantity of explosives initiated on the same delay to crack the rock between adjacent holes. The row is initiated before the main shot.

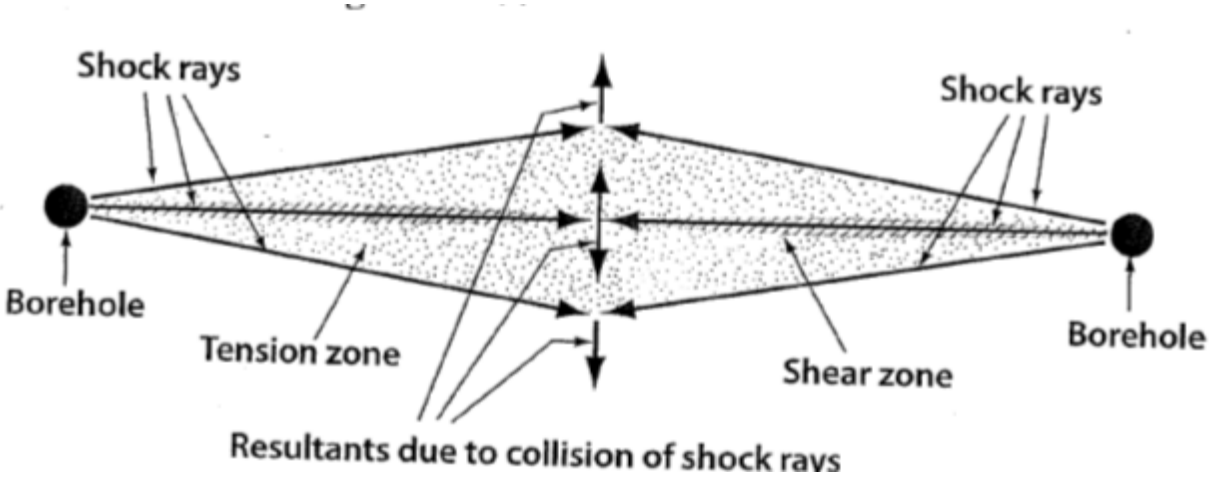

Figure 3-16: Presplitting theory illustration (ISEE, 2011)

Figure 3-16 demonstrates "resultants due to collision of shock rays". What is not clear from the diagram is what this resultant is, if the shockwave collision occurs in this manner then the crack would appear perpendicular to the blast holes rather than joining them. The ISEE handbook (1998) states that "the theory of presplitting in controlled blasting is that when two charges are shot simultaneously in joining holes, collision of shock waves between the holes places the web in tension and causes cracking that gives a sheared zone between the holes".

Figure 3-17 shows a presplit blast and a fragmentation blast taken from Muller et al, (2013) when timing is instantaneous. Theory is the same as in Figure 3-16, demonstrating that an overlap in shock wave Mach cones are the cause of the single line crack of a presplit. This fragmentation pattern differs significantly from the top down view of fragmentation shown in the right hand, fragmentation blast. Interestingly, the overlapping of Mach cones in the presplit blast correlate to the overlapping of P and S waves in Figure 3-15. Rossmanith, in his explanation says that fragmentation will be greatest between the two holes but Muller et al (2003) show no sign of fragmentation between holes, just a single line joining them. Both theories cannot be true.

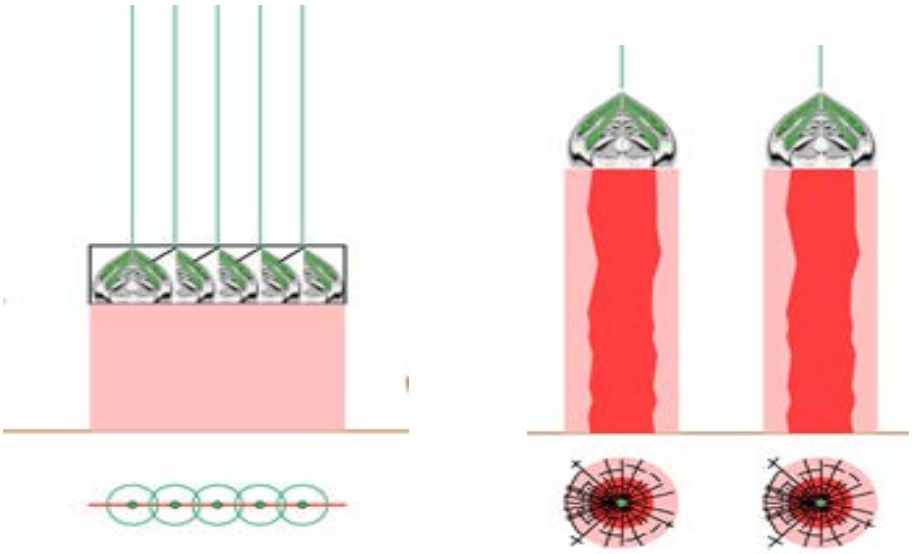

Figure 3-17: Presplit blast and fragmentation blast with Mach fronts. (Muller et al, 2013)

Worsey (1984) argues that the crack is not due to wave interaction at all, but by hydrofracture. The lower power, deflagrating explosives used, or decoupled high explosives, reduce the dynamic effects of the explosive and resultant rock stresses. The crack produced in a presplit is most likely caused from the joining of radial cracks from neighboring holes through the high pressures associated with gas expansion. The elongated line occurs due to the confinement around the blast holes and no free face for gas pressures to expand towards. The easiest path for the gas pressure is to the closest blast hole. McHugh (1981) agrees with that of Worsey in that the gas pressure penetrates the initial cracks formed around the blast hole with the pressures exerted large enough to extend the crack to the next hole. A series of tests in Plexiglas and calculations demonstrate this theory.

3.4 Timing effects on Fragmentation

The effect of timing with regards to blasting is not a new concept. Timing has for many years thought to have an influential control of muck pile placement and heave and the control of adverse environmental effects; ground vibration and air blast. It is only since accurate timings have been available through electronic detonators that timing effects and

fragmentation have been in association. Anecdotal papers are also available but with limited data.

3.4.1 Electronic Detonators

Detonators have come a long way since the introduction of safety fuse in 1831 utilizing a cord of black powder. In the early 1920's electric detonators were used that implemented electric wires connected to an aluminum shell cap. The ignition occurs using a bridge wire as a match to ignite a charge. More recently, 1960 - 1970s, a non-electric detonator was introduced. A shock tube with a light explosive dusting on the inside replaces the electric bridge wire of an electric detonator. A delay element was introduced using a specified length of pyrotechnic element, the length of time required to burn the pyrotechnic element governed the delay time for the detonator. This pyrotechnic element was also implemented into the early electric detonators. Due to the chemical makeup of the delay element, the accuracy is relatively low. Larsson et al (1988) published results of accuracies of 1.5 – 2.5% of the total delay time and also stated that inaccuracy increased with delay time. Bajpayee et al (1990) agree with this statement publishing conclusions of increased scatter with increased delay time for electric and nonelectric detonators. This inaccuracy is an improvement than with their first introduction but in some circumstances the scatter can be detrimental to fragmentation and ground vibrations with holes firing out of sequence.

Electronic detonators include an electronic circuit and bridge wire to create a delay with a small microchip that can currently be programmed in 1ms increments, rather than the length of pyrotechnic element seen in electric and non-electric detonators. Figure 3-18 shows a simple construction of the electric, nonelectric and electronic detonators. (Watson, 1988). Delay detonators can be simply grouped as pyrotechnic delay and electronic delay for the remainder of this work.

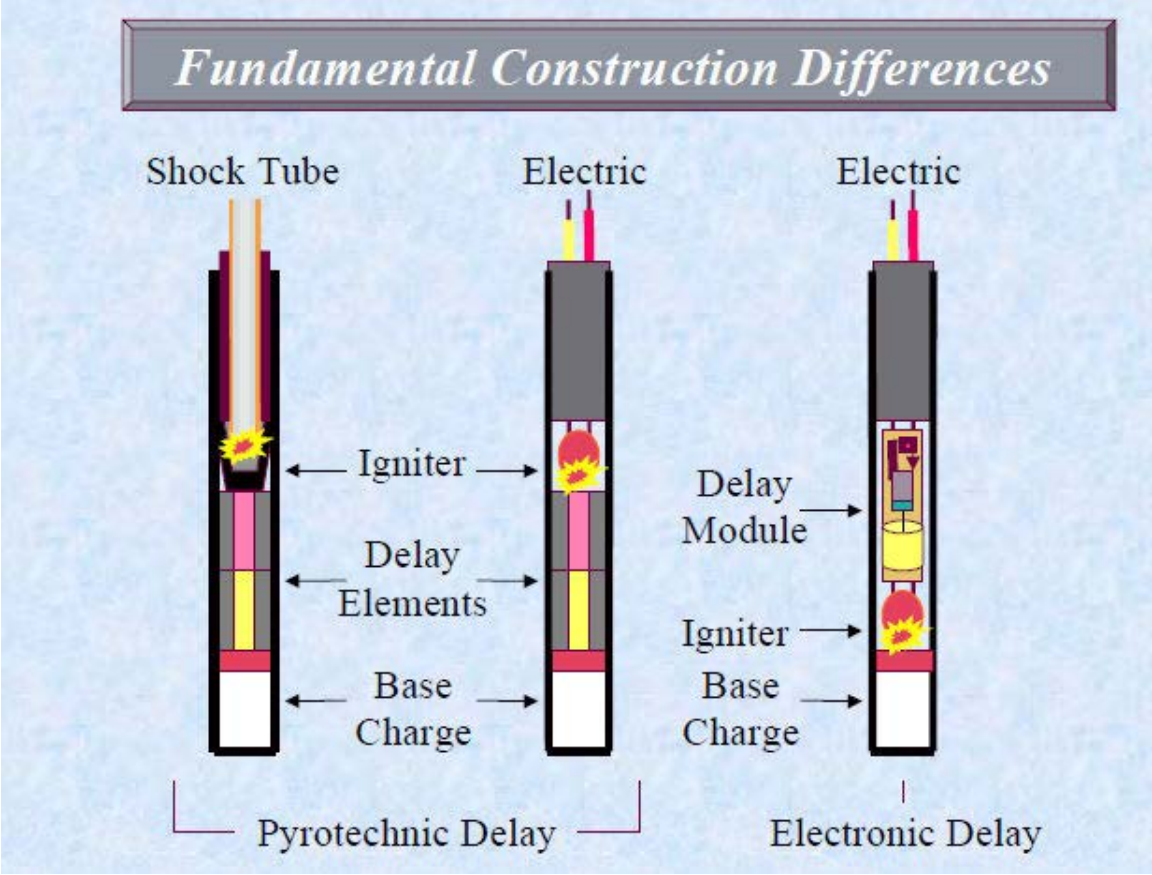

Figure 3-18: Detonator types (Watson, 1988)

Table 3-3 and Table 3-2 show results published by Lusk et al (2012) on the accuracy of electronic detonators against non-electric. Detonators A and B simply refer to two different manufacturers, that are not named. Results coincide with that of Bajpayee et al (1990) and Larsson et al (1988) that the scatter of all detonators increases with delay time. Results also show that non-electric detonators have a larger scatter range than electronic with maximum standard deviation of 19.054 compared with that of 3.751 for electronic.

Timing is crucial for blast design, for fragmentation and maximum scaled distance requirements. Results from Lusk et al (2012), Bajpayee et al (1990) and Larsson et al (1988) show clear evidence that when using pyrotechnic detonators the time you design your blast to and what your final blast shot produces are two very different things.

Table 3-2: Electronic Detonator accuracy (Lusk et al, 2012)

Electronic Detonator Results						
	Electronic Detonators A			Electronic Detonators B		
Programmed Delay (ms)	10	1000	8000	10	1000	8000
Number of detonators Tested	53	43	50	51	52	47
Delay Average (ms)	9.950	1000.543	8003.375	9.987	999.804	7998.589
Standard Deviation	0.092	0.321	3.751	0.030	0.107	0.851
Maximum (ms)	10.201	1001.120	8015.625	10.052	999.954	7999.400
Minimum (ms)	9.816	999.960	7995.190	9.910	999.460	7995.800
Percent Error	-0.501%	0.054%	0.042%	-0.130%	-0.020%	-0.018%

Table 3-3: Non-electric detonator accuracy (Lusk et al, 2012)

Non-electric Detonator Results						
	Non-electric Detonators A			Non-electric Detonators B		
Nominal Delay (ms)	9	1000	1400	25	100	700
Number of detonators Tested	68	60	67	59	65	59
Delay Average (ms)	11.342	1125.501	1418.766	27.751	102.730	715.710
Standard Deviation	4.594	6.550	19.054	0.765	11.250	6.195
Maximum (ms)	15.756	1146.782	1462.381	29.304	123.193	730.575
Minimum (ms)	1.534	1114.704	1367.035	26.155	79.835	697.925
Percent Error	26.023%	12.550%	1.340%	11.005%	2.730%	2.244%

3.4.2 Review of timing and fragmentation research

Electronic detonations have many proven benefits including, but not limited to, operational efficiency, vibration reduction, consistency of results and safety. A relationship between the effects of fragmentation and timing has been examined by researchers since the introduction of electronic detonators. The following paragraphs present results from previous researchers in this area.

Stagg and Rholl (1991) provided data of 29 small scale tests, where fragmentation was measured varying the timing between holes. The small scale tests showed fragmentation is improved with timings greater than 3.3ms/m of burden. A second full scale test from the same study showed that short (1ms/m) and long delays (26ms/m) had adverse effects on fragmentation. The very short delays suggest periods where wave propagation will influence fragmentation. Rossmanith (2003) states that wave interactions are of vast

importance to rock fragmentation. These interactions are that of the wave itself with natural features in the rocks, such as cracks or free faces, implying that short delays are going to be most influential with many mines utilizing this concept with electronic detonators.

Katsabanis et al (2014) published a paper reviewing certain literature on timing and fragmentation relationships. Some of his earlier work with Liu (1996) used a 6.5 ft bench with a burden of 2.6 ft and hole diameter of1.5 in to establish the effect of delay time. Various delay times were used and recorded on high speed video camera. Fragmentation was analyzed manually from the videos, this in itself is not very accurate and eliminates the visibility of small fragments. Consequently only large differences can be observed (Katsabanis and Liu, 1996). Optimum fragmentation (smallest d50 size) occurred at 8ms/m, discrepancies in the testing however does not allow for confidence in these results.

McKinstry (2004) extensively discussed the use of electronic detonators at Barrick. A time of 3ms between holes on the same row to utilize the collision of stress waves has proven beneficial at this location.

Katsabanis (2006) carried out small scale tests using blocks of granodiorite that were 92cm by 36cm by 21cm. A total of 23 blast holes were drilled per block, 11mm in diameter. The explosive used was detonating cord of varying lengths to alter the timing. Largest fragments were produced with instantaneous detonation where elongated cracks simply joined blast holes together, like that of a pre-split. Fragmentation increases with delay until the delay becomes so great it is equivalent of firing each hole independently. At times greater than 22ms/m no increase in fragmentation is present. Results found by Katsabanis (2006) agree with that by Stagg and Rholl (1991) that improved fragmentation is now available using electronic detonators, but perhaps more likely that the reason for this is improved accuracy, not the ability to detonate at very short delay times where there is a possibility for stress wave interaction.

Work by Johansson and Ouchterlony (2013) attempted to eliminate some of the primary concerns with previous experimental data; scatter and a lack of repeatability with

concurrent tests: unwanted additional reflection zones around the block and few points covering the range of timings in question. The novel experimental technique used by Johansson and Ouchterlony (2013) was the addition of a magnetic mortar yoke around the sample to reduce the reflection zones not present in a typical bench blast. Two blast rows were used, blasted independently of each other and fragmentation analyzed after each. A burden and spacing of 2.76 in and 4 in, respectively, was used with 5 holes per row. PETN was used as the explosive from 100gr/ft detonation cord giving a powder factor of 1.2 lb/yd^3. The explosive was decoupled within the hole. All times used were below 2ms/m of burden, below the optimum found by other authors (Katsabanis, 2006; McKinstry, 2004) but within the shock interaction times.

Table 3-4: Timing delay used by Johansson (2013)

Nominal Delay (μs)	Delay (ms/m of burden)	Expected Interaction
0	0	Instantaneous Initiation
28	0.4	P-Wave interaction at neighbor hole
37	0.53	Shock wave interaction at neighbor hole
46	0.66	Initial tensile phase interaction with shock wave
46	0.66	Initial tensile phase interaction with shock wave (repeat)
56	0.80	Intermediate tensile phase interaction with shock wave
73	1.04	Vanbrabant (2006) 2nd scheme
73	1.04	Vanbrabant (2006) 2nd scheme
73	1.04	Vanbrabant (2006) 2nd scheme, confined
73	1.04	Vanbrabant (2006) 2nd scheme, confined
86	1.23	Vanbrabant (2006) recommendation
146	2.08	No shock wave interaction, confined
146	2.08	No shock wave interaction, confined
146	2.08	No Shock Wave Interaction
∞		Single Shots to determine shock wave arrival times at neighbor hole

Results by Johansson and Ouchterlony (2013) display a boulder and dust character that does not fit well with the Kuz-Ram model due to the normal distribution from the Rosin-Rammler curve. For row 1 scatter was much greater than in row two, where the material

had already been pre conditioned. The least back break and smoothest wall after a row was shot was for instantaneous detonation, essentially representing a pre-split blast.

The most recent experiments were carried out by Katsabanis et al (2014) where a similar technique to Johansson and Ouchterlony (2013) was used, using a stronger yoke around the back and sides of the concrete to be tested. Figure 3-19 shows the extent of the yoke. Material to be blasted was positioned within the three walls. Block dimensions were 60 cm x 40 cm x 25 cm with boreholes 12 mm in diameter of length 23 cm. Timing between holes, of spacing 10.5 cm went to a nominal delay of 2000 ms. This is equal to 27 ms/m of burden based on the 7.5 cm burden. PETN was used as the explosive with a power factor of 1.2 lb/yd^3 which was doubled after poor results on the first tests. Results show that that the worst fragmentation is achieved with instantaneous detonation, both for average particle size and fit to the Swebrec and Rosin-Rammler distributions. Results plateau at the optimum fragmentation between 400 μs and 1000 μs so an exact optimum could not be determined. Mean fragmentation size increases again after 1000 μs.

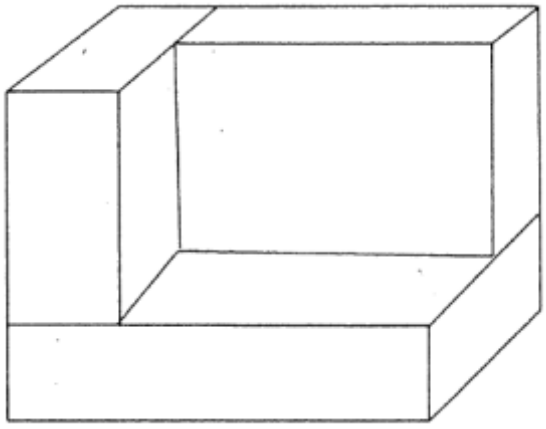

Figure 3-19: Schematic of yoke used by Katsabanis et al (2014) and Johansson and Ouchterlony (2013)

Due to the supersonic speed of a shockwave, the time between two adjacent holes would have to be almost instantaneous for this interaction to occur. Katsabanis and Liu (1996), Rossmanith (2002), Vanbrabant and Espinosa (2006) Katsabanis et al (2006), Johansson and Ouchterlony (2013) and Katsabanis et al (2014), however, have all published results stating that a reduction in fragmentation occurs with timing of less than 2 milliseconds

per meter of burden. More than 2 ms between holes and the shock wave of the first hole will have passed the second and no collision will be present.

3.5 Finite Element Modelling of Explosive Products

Finite analysis modelling codes such as ANSYS or FLAC 3D have been used to model blast phenomena for years. Models can be beneficial in calculating and predicting stress and strain rates as well as deformation that are difficult to execute experimentally. The most commonly used program for the short duration, high pressure loading from an explosive charge is ANSYS. The analysis tool is used for modelling nonlinear dynamics of the interaction between solids, fluids and gasses. Typical application for the program include, impact, ballistic protection, energetic systems, blast propagation, blast effects on structures and materials research. A number of solvers are available, including (ANSYS, 2013):

- Finite element solvers for computational structural dynamics; Lagrange and Euler (FE)
- Finite volume solvers for fast transient Computational Fluid Dynamics (CFD)
- Mesh free particle solvers for high velocities, large deformation, and fragmentation (SPH)
- Multi solver coupling for multi physics solutions including coupling between FE, CFD and SPH

Numerous analysis systems are available in ANSYS Workbench, including, but limited to, Explicit Dynamics, Static Structural, Steady-State Thermal and Laminar Buckling. In addition to the ANSYS systems, concurrent systems have been purchased by ANSYS, including that of Autodyn, originally developed by Century Dynamics (Century Dynamics, Inc, 2003). Explicit Dynamics has been developed to design and compute impacts of short duration, high pressure loading, often too dangerous to accomplish experimentally. Explicit Dynamics is limited in the solvers available, more complex interactions between explosives and solids, for example, have to be run in Autodyn. Both systems contain a number of inbuilt material models and a geometry modeler to simulate a multitude of scenarios.

3.5.1 Previous research in Modeling Blast Phenomena

Schonberg et al (2005) used Autodyn to model building response subjected to blast pressures. The Riedel, Hiermaier and Thoma (RHT) material strength model was used for the building properties. The authors stress the importance of a correct strain erosion rate for your model. Applying erosion to a model essentially removes a cell after material or strain failure and transfers the energy to a neighboring cell. Figure 3-20 shows Schonberg et al's (2005) building after 0.205 seconds with no erosion set. The severe stretching demonstrated is clearly not characteristic of concrete. For characteristic fragmentation to occur, a strain erosion failure rate was set to 0.02, after a series of iterations. This model can be seen in Figure 3-21

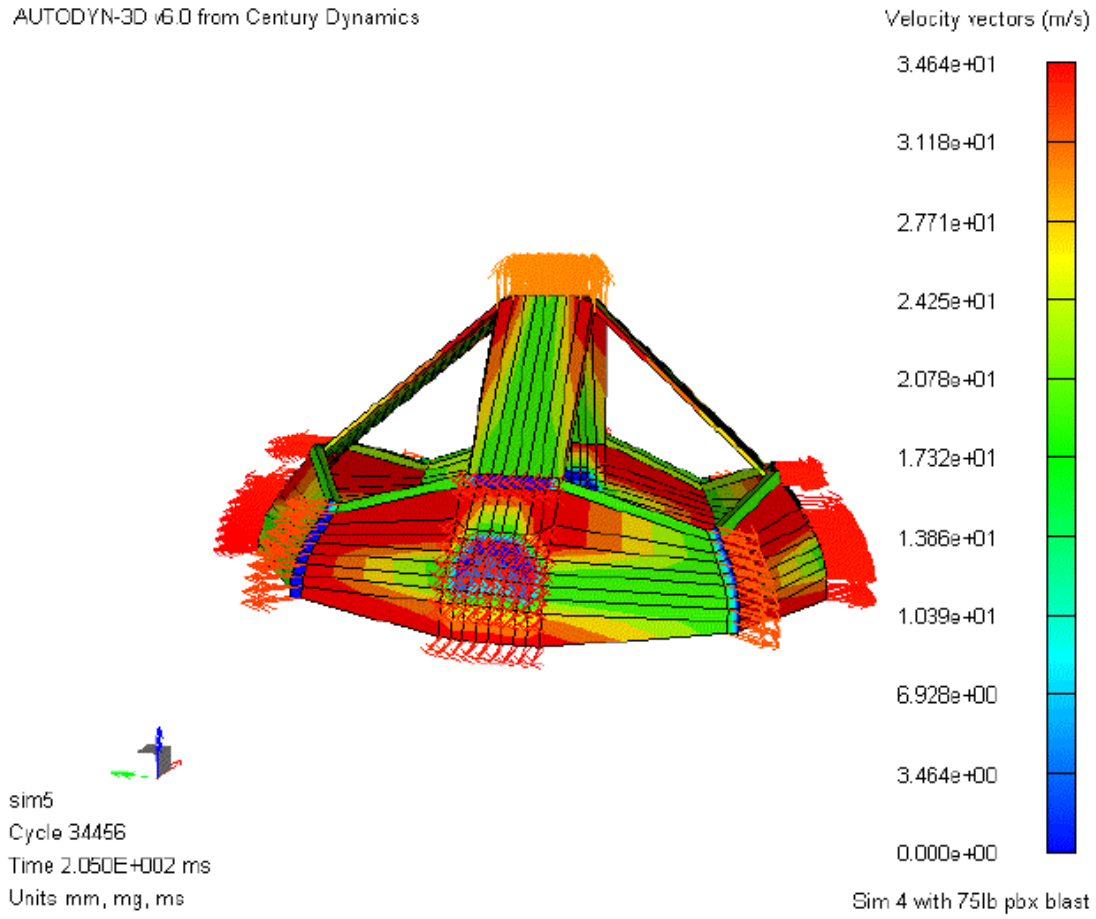

Figure 3-20: Concrete modelled with no strain erosion (Lusk et al, 2006)

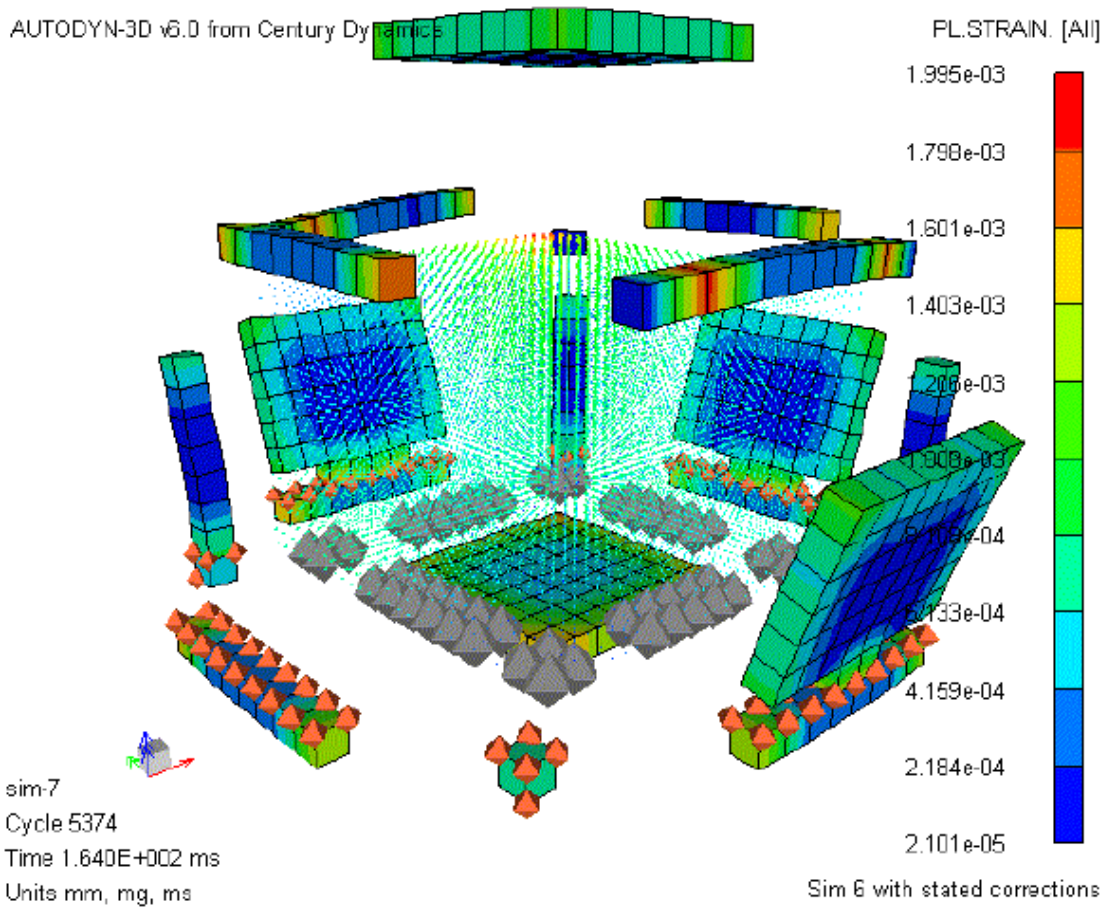

Figure 3-21: Concrete modelled with strain erosion set to 0.02 (Lusk et al, 2006)

Lusk et al (2006), in a review of the Autodyn part of the project, explains the unique grid coupling between Euler and Lagrange grid types. The explosive, TNT in this case, as well as the air inside the building have been modelled with an Euler grid while the concrete building has been modelled using a Lagrangian grid. Reference is given to Fedwik (2002), stating that Euler grids are effective for fluid and gasses, but not for solid material behavior. Lagrange grids are most suitable for solid material calculations whilst being impractical for gases. Lusk et al (2006) used Autodyn to couple the two grids together. Since the publication of this Journal article, Autodyn was purchased by ANSYS from Century Dynamics. Now, this same coupling interaction can occur but the use of both Explicit Dynamics, in ANSYS, and Autodyn are required.

The interaction between Euler and Lagrange grids has also been modelled by Preece and Lownds (2008) in a paper entitled "3D Computer Simulation of Bench Blasting with Precise Delay Timing". Two adjacent blast holes are modelled and a series of timings reviewed between of the two blast holes, utilizing bottom initiation. Figure 3-22 demonstrates the portion of a bench blast that has been modeled. The use of symmetry planes allow for much shorter computational times. Parameters input in the model are :

- Burden: 32.5 ft
- Spacing 48 ft
- Borehole Diameter: 12 in
- Explosive: Emulsion
- Rock: Shale with UCS of 800 psi

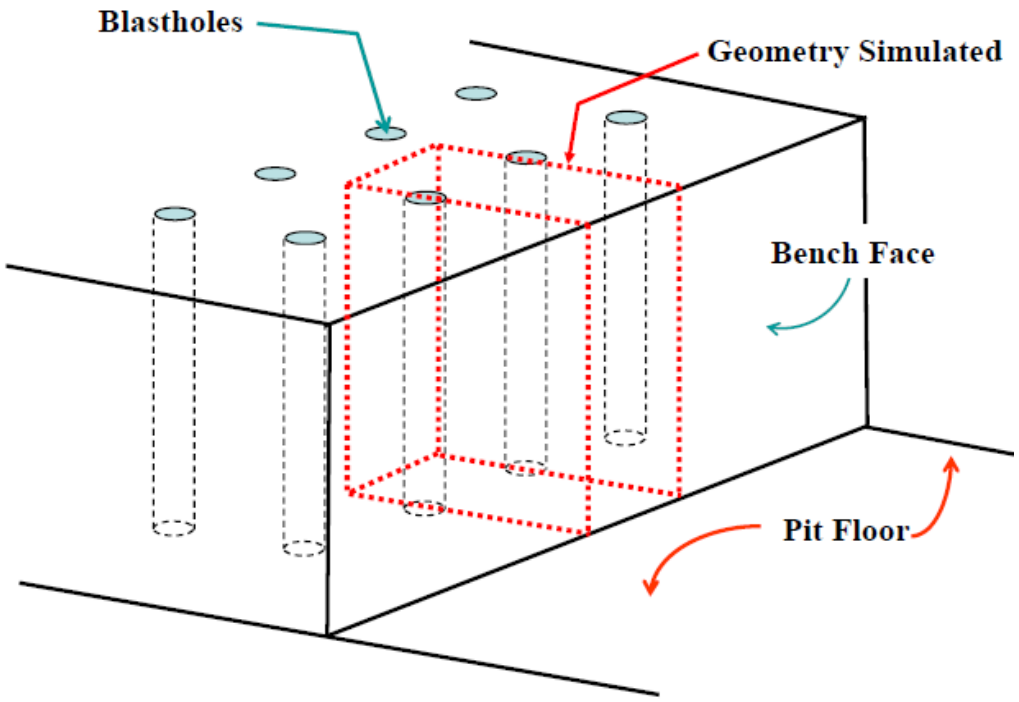

Figure 3-22: Portion of blast geometry modeled (Preece and Lownds, 2008)

The RHT material model for brittle material was used for the shale portions of the model in a Lagrangian mesh. The authors have used this model with effective results in a number of publications (Berg and Preece, 2004; Preece and Chung, 2003; Preece 2006; 2007). Figure 3-23 shows the Lagrangian mesh for the shale and embedded Eulerian grid

for the Emulsion explosive. The borehole is clearly supposed to circular; however authors stress the drastic increase in computational time when the shape is refined.

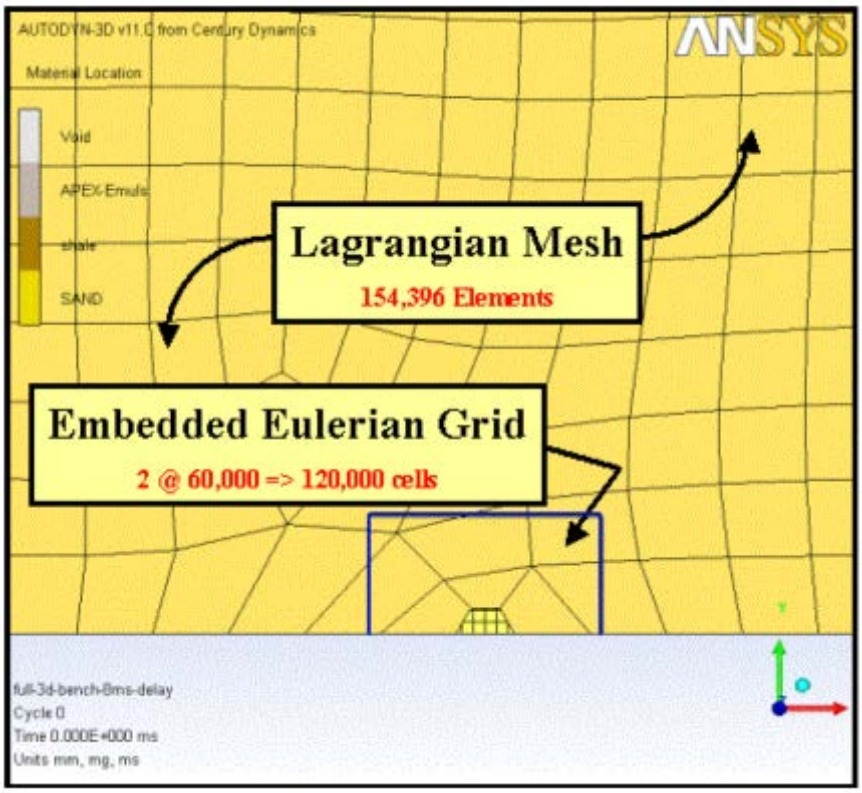

Figure 3-23: Euler and Lagrange grids (Preece and Lownds)

The RHT model is ideal for simulating the compressive shock wave velocity and the lagging crack propagation velocities. When two compressive waves are introduced and once interacts with already damaged material, a portion of this is reflected while a separate portion continues through the damaged material, at a reduced velocity. Figure 3-24 demonstrates two compressive waves (red) detonated 2 ms apart. The dark blue represents rock at a tensile stress of at least 700 psi (Preece and Lownds, 2008).

Detonation times evaluated were 0, 2, and 8 ms. The short delay times are not conducive of the best fragmentation. Instantaneous detonation does increase damage contours in the model (Figure 3-25) , but the poor throw and large vibrations observed in the field make it an impractical solution. Large delay times were not computed due to the excessive computational time necessary to calculate them. The optimum time, according to data collected by Stagg and Rholl (1987), would be 42 to 88 ms time difference

between holes, far greater than those already tested. The time to compute the 2ms model for 20ms took 6 hours. (Preece and Lownds, 2008)

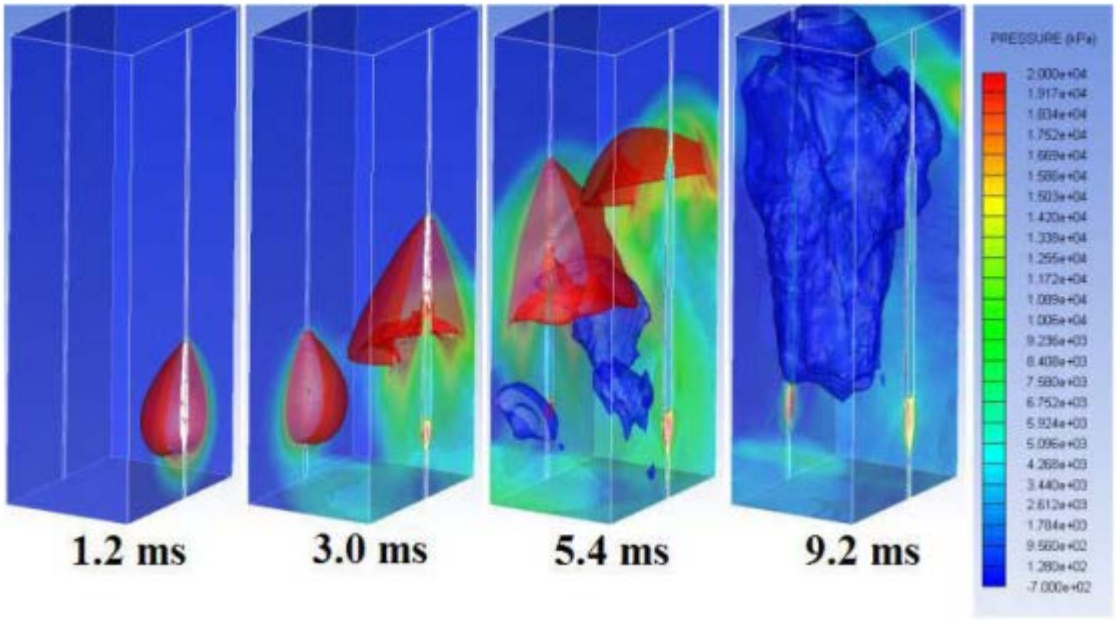

Figure 3-24: Two adjacent blast holes detonated 2 ms apart. (Preece and Lownds, 2008)

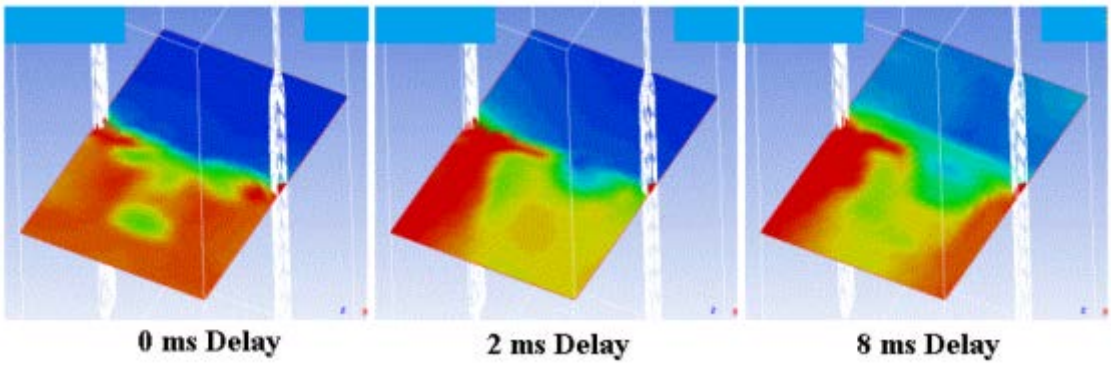

Figure 3-25: Damage contours at 0, 2 and 8 ms (Preece and Lownds, 2008)

A numerical model using Autodyn to determine rock failure and fragmentation due to blast wave pressure in 2D was carried out by Zhu et al (2008). A 2D slice through a cylindrical block was modeled using 1.1 g/m (7 gr/ft) detonating cord as the explosive through the center. Dimensions, in mm, are shown in Figure 3-26.

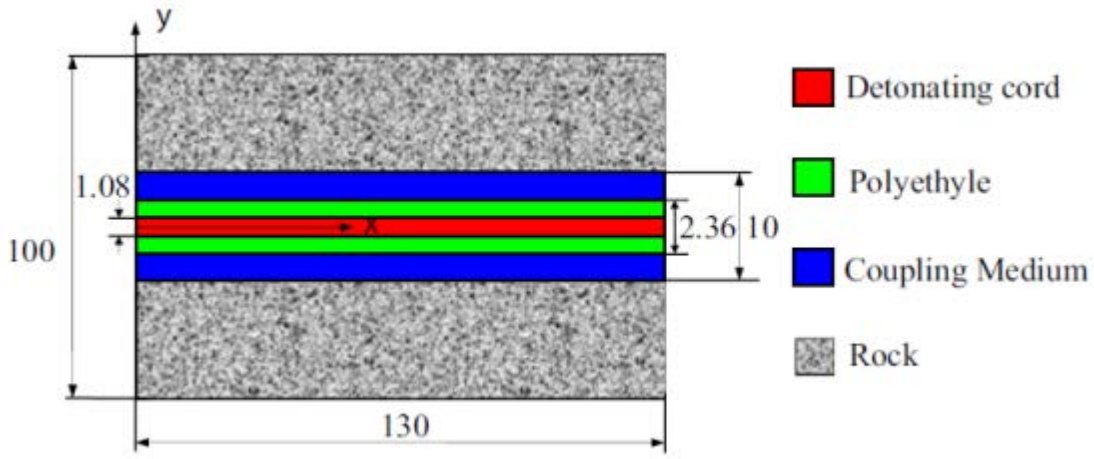

Figure 3-26: Dimensions of 2D slice of Cylindrical block (mm) (Zhu et al, 2008)

A coupling medium was applied to the model either air, sand or water; and a polyethylene sheath directly around explosive is also simulated. Both stress wave loading and gas pressure are crucial in the fragmentation process. Only stress wave propagation was studied in this paper and the resulting crushed zone, severely fractured zone incipiently cracked zone around the borehole wall, as well as spalling cracks have been simulated. A Lagrange grid has been used to model the homogeneous rock, diorite, while Euler grids have been used to model the water, air and explosive. Four equations of state have been used in the simulation, linear, shock, compaction and ideal gas. A linear EOS has been applied to the rock due to the low pressures asserted on it due to the low quantity and additional coupling medium absorbing some of the shock. Coupling medium air is modeled using an ideal gas EOS, sand employs a compaction EOS and water utilizes a shock EOS. The erosion of elements has been applied to the model, reducing effect of strain of the particle, effectively removing them upon failure, similar to that of Schonberg et al (2005). A series of screen shots have been taken and represented in Figure 3-27 with single initiation from the left side of the block. Shear stress failure immediately around the borehole is demonstrated in yellow in Figure 3-27. Beyond this, three distinct groups of tensile failure zones have been identified:

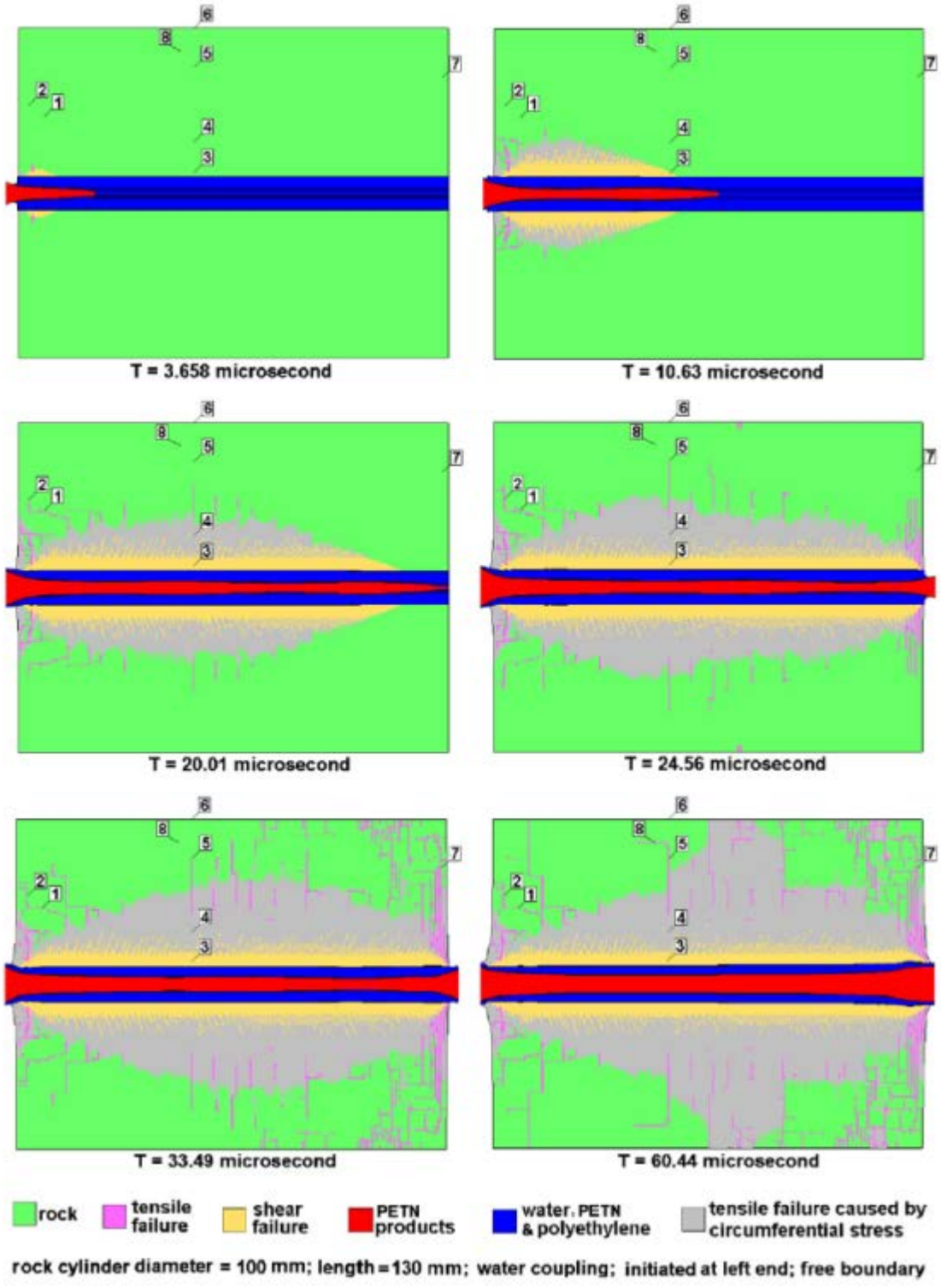

Figure 3-27: Material status with time of simulated block. Target points are numbered 1 through 8. (Zhu et al, 2008)

1. Cracks perpendicular to the explosive axis caused by tensile stresses (Pink vertical cracks in Figure 3-27)
2. Cracks parallel to the explosive axis caused by tensile stresses (Pink horizontal cracks in Figure 3-27)
3. Cracks formed due to the circumferential stress. Crack extends into the block and limited due to 2D model. (Grey in Figure 3-27)

Target points have been added to the model. At each of these points, stress in the x, y and circumferential (θ) directions have been monitored over time. Figure 3-28 show the effects from the element containing target 3 (left) in the shear failure zone and target 5 (right) in the type 2 tensile zone. Target 3 contains only compressive stresses in the x and y directions. Failure of the element occurs due to the shear stress reaching a level in excess of that input into the material model, after which points it returns to zero. Target 5 however shows failure by tensile stress. Initially, stresses are compressive but change to tensile with increasing time, and ultimately fail in tension around 23 microseconds.

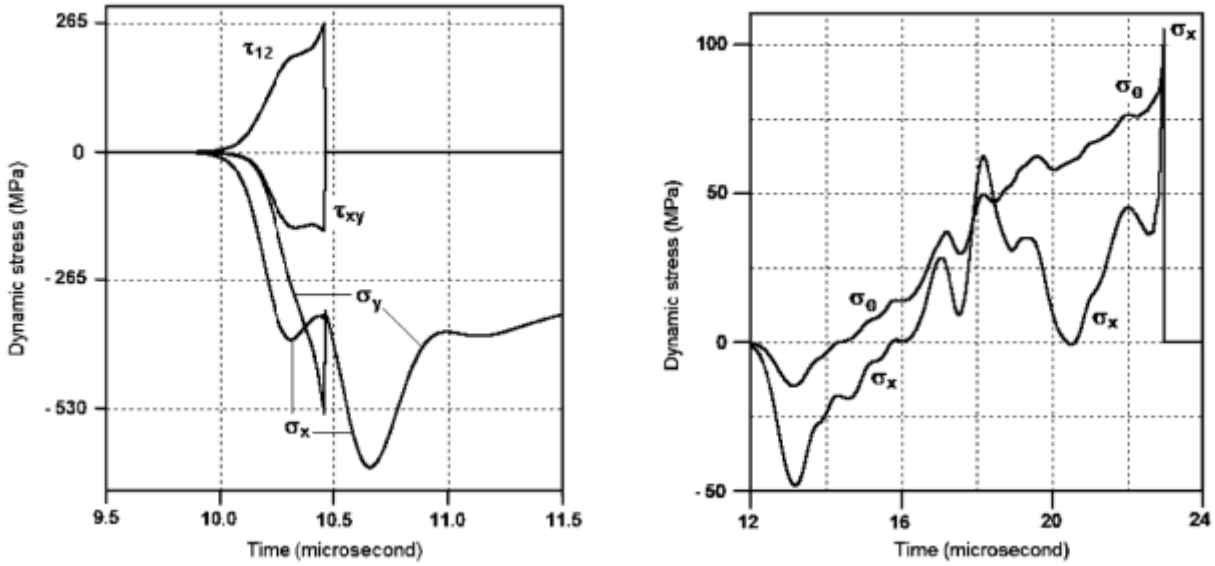

Figure 3-28: Left: dynamic stresses (normal and shear) versus time for target 3; Right: Dynamic stresses (normal) versus time for target 5

A series of influencing factors are also modelled, including coupling, confinement, initiation location and air ducking. The stress wave analysis using target cells in Autodyn was a successful way of examining the data output from the simulations.

Computer simulations in LS-DYNA were developed by Sjoberg et al (2012) using a similar setup as Johannsson and Ouchterlony (2013). The RHT model was used to simulate the concrete. Euler solvers were used to model the explosive and Lagrange the concrete. Only short duration models were simulated due to the extensive deformation observed during longer runs. Results show that areas of wave interaction were small and an increase due to this unlikely. Largest effects on fragmentation were seen when hole spacing and quantity of explosive were altered, effectively just increasing the powder factor. Model simulations accurately demonstrated the phenomenon in question but more tests are ongoing.

Chapter 4. Experimental Investigation into the Relationship Between Shockwave and Detonation Wave Interactions with Fragmentation

4.1 Introduction

Before the question of 'greatest fragmentation is achieved between holes due to shock wave collision' can be answered, how shock waves react in strata compared to that of air needs to be established. A significant understanding of head on collisions between shock waves either with each other, or a solid object such as a bullet hitting a target is known (Cooper, 1996). For this reason, rather than attempting to implement multiple hole interactions, a single borehole was tested experimentally. Experimental tests by Johansson and Ouchterlony (2013) and Katsabanis et al (2014) and simulations by Preece and Lownds, (2008) have notable differences in overall fragmentation with different timings. No significant differences in fragmentation patterns between blast holes were observed, despite a number of their tests being in time delays where shock wave collision will occur. Fragmentation was collected after the event, but in-situ crack formation not recorded. Interactions of colliding detonation waves in a single hole has not been tested experimentally to the same extent as shock waves between holes. It is common practice to have a backup detonator per hole in case of a misfire. Therefore, by placing this additional detonator at a different location in the hole to create a detonation wave collision at no additional cost, can fragmentation be increased?

Tests were carried out looking at the collision of detonation and shockwaves through strata. Identical solid concrete masonry blocks were used for the experiments. The blocks were 15x7¾ x7¾ inches in size. Detonating cord, at a strength of 50 grains/foot (gr/ft), was the explosive used for the tests, initiated using 25 ms surface delays. One block from each test was recorded on high speed video at 250 frames per second. The remaining blocks were wrapped in geotextile fabric and welded wire mesh to contain the fragments for further analysis.

4.2 Experimental setup

A total of 27 tests were carried out at the University of Kentucky Explosive Research Team's Experimental Mine, located in Georgetown, Kentucky to investigate both colliding detonation and shock waves. Solid masonry blocks were used for the experiments. Both the relatively small size to effectively handle multiple repetitions of the experiments and uniformity of the concrete made them an ideal option. All blocks were formed at the same location, on the same day and all tests carried out in the same atmospheric conditions for constant repeatability.

The explosive used for the experiments was Pentaerythritol tetranite (PETN) in the form of detonating cord. Detonating cord is a common explosive in mining operations used as downline or trunkline initiators for detonating a high strength booster. PETN is known to have a very constant detonation velocity, independent of its surroundings, making it ideal for repeating multiple tests with little deviation. Detonating cord is essentially a thin flexible cord of PETN coated in plastic to contain the explosive. A large reel can be cut easily in to various lengths without weighing out the explosive each time. The grade of detonating cord used was 50 gr/ft, or 10.8 grams per meter (g/m). The idea for the blocks and detonating cord through the center to visualize colliding waves came from the D'autriche Method for measuring VOD. The method has been used for years, benefiting from the constant detonation velocity of detonating cord. Using a typical bulk explosive, such as ANFO or Emulsion, would not be practical for these tests due to the small blasthole diameter used. These explosives have a critical diameter of approximately two inches, more sensitive emulsions are available but the critical diameter is still much larger than that being used in these experiments. Additionally, bulk explosives are non-ideal, meaning that even small changes in the atmospheric conditions could alter the consistency of the results.

The three tests carried out were:

- *Test 1: Single initiation* – Detonating cord is initiated from one end and no collisions of dynamic waves occur. Used as a baseline test to compare with Test 2. Six blocks were tested.

- *Test 2: Colliding Detonation Waves* – Detonating cord is initiated from both ends, creating a collision of detonation waves through the center of the block. The same quantity of explosives as Test 1 is used for a direct comparison. Six blocks were tested.
- *Test 3: Colliding Shock Waves* – No explosive is present through the center of the block, allowing only the two shock waves to progress through and collide in the center, similar to what would occur between blast holes. Fifteen blocks were tested.

4.2.1 Test 1: Single Initiation

Six blocks were drilled through the center down the full 15 inch length side of the blocks. The drill bit size was 0.375 inches. The diameter of the 50 gr/ft detonating cord was 0.185 inches leaving the explosive slightly decoupled within the drilled hole. This allows some of the gas pressure to escape, leaving most of the fragmentation to occur through the dynamic stress waves. A three feet length of 50 gr/ft detonating cord was cut and thread through the drilled hole, zip ties were placed at each end to prevent the cord from moving, leaving 1.25 inches at the bottom end of the block for consistency. Five of the blocks were wrapped three times in geotextile fabric and three times in welded wire mesh to contain the fragments (Figure 4-1). This method was taken from that used in demolition, where chain link and geotextile fabrics are used on support columns to prevent fragments flying and causing cutoffs in any of the undetonated structure. The sixth block was left unwrapped to record on high speed video at a frame rate of 250 frames per second (fps). A 25 ms surface delay was secured to the end of the detonating cord and detonated using a remote fire triggering system. The powder factor for Test 1 was 0.46 pounds explosive per cubic yard (lb/yd^3), in the ideal range of 0.25-0.5 lb/yd^3 for a boulder shot. The blocks were painted green and collected samples will be referred to as samples T1a through T1e. Figure 4-2 shows the test 1 setup, where red line represents the detonating cord.

Figure 4-1: Sequence of block preparation

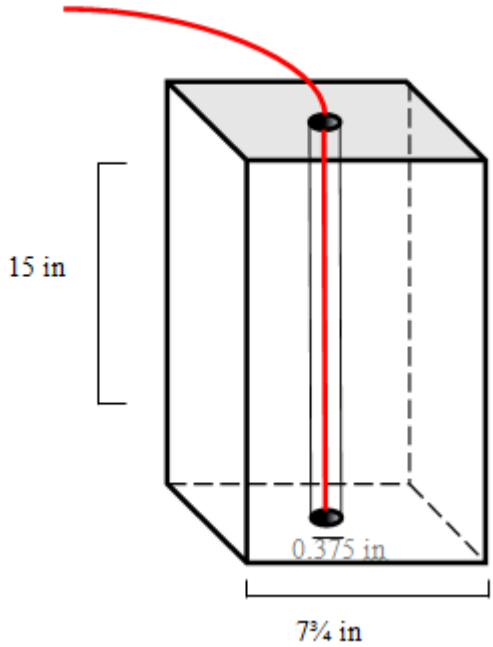

Figure 4-2: Test 1 layout

4.2.2 Test 2: Colliding Detonation Waves

The blocks for Test 2 were prepared in the same manner as Test 1 and drilled through the full length of the block. A 6 ft length of detonating cord was cut, threaded and secured through the drilled hole, leaving the exact same excess at each end of the block, giving the same powder factor as Test 1 of 0.46 lb/yd^3. The surface delay was secured to both ends of the detonating cord for simultaneous detonation and the collision of the detonating waves through the center of the block. Again, five blocks were wrapped and one left open for use with the high speed video camera. Blocks for Test 2 were painted orange and samples T2a through T2e retained for further analysis. Figure 4-3 shows the test 2 configuration.

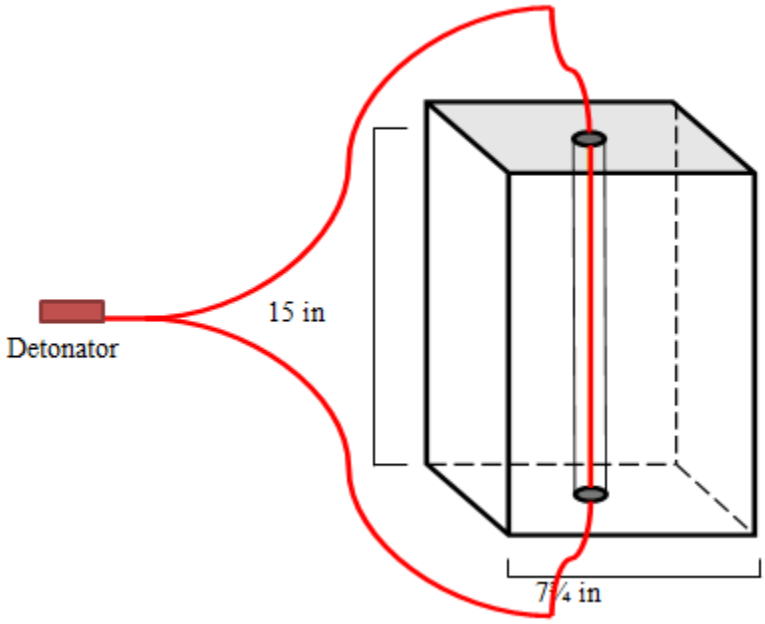

Figure 4-3: Test 2 Layout

4.2.3 Test 3: Colliding Shock Waves

Blocks for Test 3 were only drilled one third of the way from each end of the block, leaving the middle third intact with no drill-hole or explosive present, in order to gauge the interaction of the shockwaves through the solid concrete. Two 3 ft lengths of detonating cord were cut and secured to each end. The powder factor for these shots was lower (0.307 lb/yd^3), but still within the recommended range. Nine blocks were examined for this test due to inconsistency of some of the results. Blocks T3a through T3h were painted pink wrapped in fabric and wire for analysis and a final block left unwrapped for recording on the high speed video camera. Figure 4-4 shows the Test 3 setup.

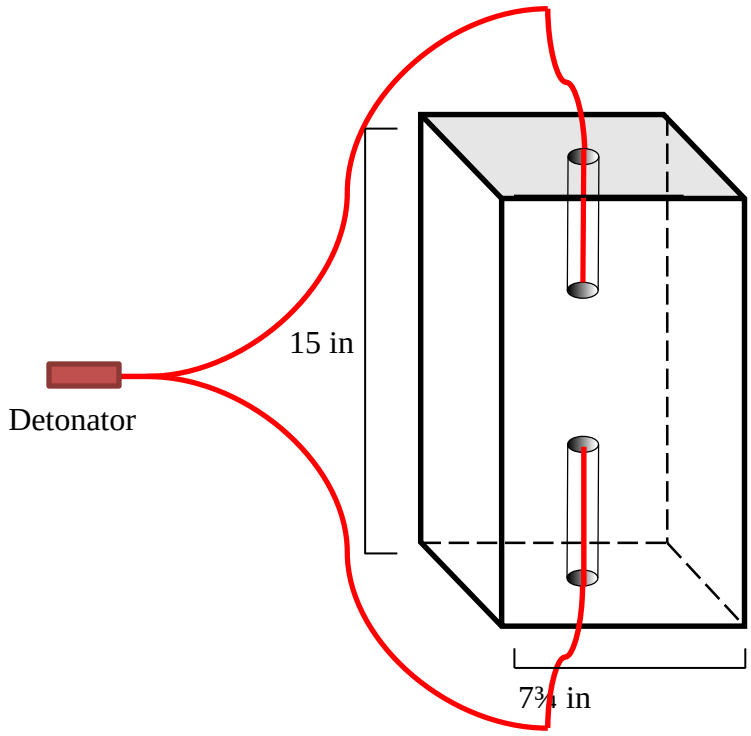

Figure 4-4: Test 3 layout

Timing effects were also investigated for Test 3. The timing difference was based on differing lengths of detonating cord either side of the block. Differences of 2, 4 and 6 inches were investigated. Since detonating cord has a constant velocity of detonation and is initiated from one end, a change in length will alter the location of the collision. Two blocks for each difference were wrapped for fragmentation analysis, making a total of 15 blocks for Test 3.

The collected samples for the 24 blocks were taken back to the lab and unwrapped carefully to preserve any evidence of tensile cracking. Particle sizes smaller than one and a half inches were processed using a series of sieves. Larger particles were placed on a work bench with a scale and a picture taken to use with WIPFRAG photographic fragmentation analysis software.

4.3 Results and Analysis

Three experimental series were carried out. Analysis of the results has been split into two sections, by powder factor. Tests 1 and 2 were analyzed together, with Test 3 analyzed separately. Analysis of the results is threefold, visual analysis of the tensile cracks after unwrapping the blocks, fragmentation analysis of the blocks, and analysis of the high speed video footage.

4.3.1 Tests 1 and 2 – Detonation Waves

The results for tests 1 and 2 can be seen in Sections 4.3.1 and 4.3.2. Visual analysis of tensile cracks once the blocks had been unwrapped is unique to this study. The geotextile fabric and welded wire mes worked well, effectively containing nearly all of the fragments, whilst maintaining the shape of the block (Figure 4-5). This process allows for both fragmentation and visual analysis. Blocks recorded on high speed video could not be further analyzed as it could not be determined where all the fragments went and all fine particles were lost on the mine floor.

Figure 4-5: Contained fragments after detonation

4.3.1.1 Visual Analysis

Visual analysis of the unwrapped blocks is the best way to see the location of tensile cracks formed from an explosive. Figure 4-7 and Figure 4-8 show the five unwrapped blocks for Test 1 and Test 2, respectively. Tests a through e are shown from left to right going down the page. It can instantly be seen that a horizontal crack is visible in Test 2 that is not visible in Test 1, at the point where detonation waves would collide. Test 1, with single initiation, shows characteristic radial cracking surrounding the blast hole with no distinct pattern vertically through the block. Compressive wave reflections at the free faces have created tensile cracks meeting in the center of the block where the detonation cord was located. Figure 4-6 backs up this observation, showing radial cracks meeting in the center. Cracks do appear vertically through the block, but no distinct pattern can be observed. Due to the long, thin shape of the fragments, it is assumed that they broke into two, or sometimes three, fragments as they reached a critical length to width ratio.

Figure 4-6: Top of block

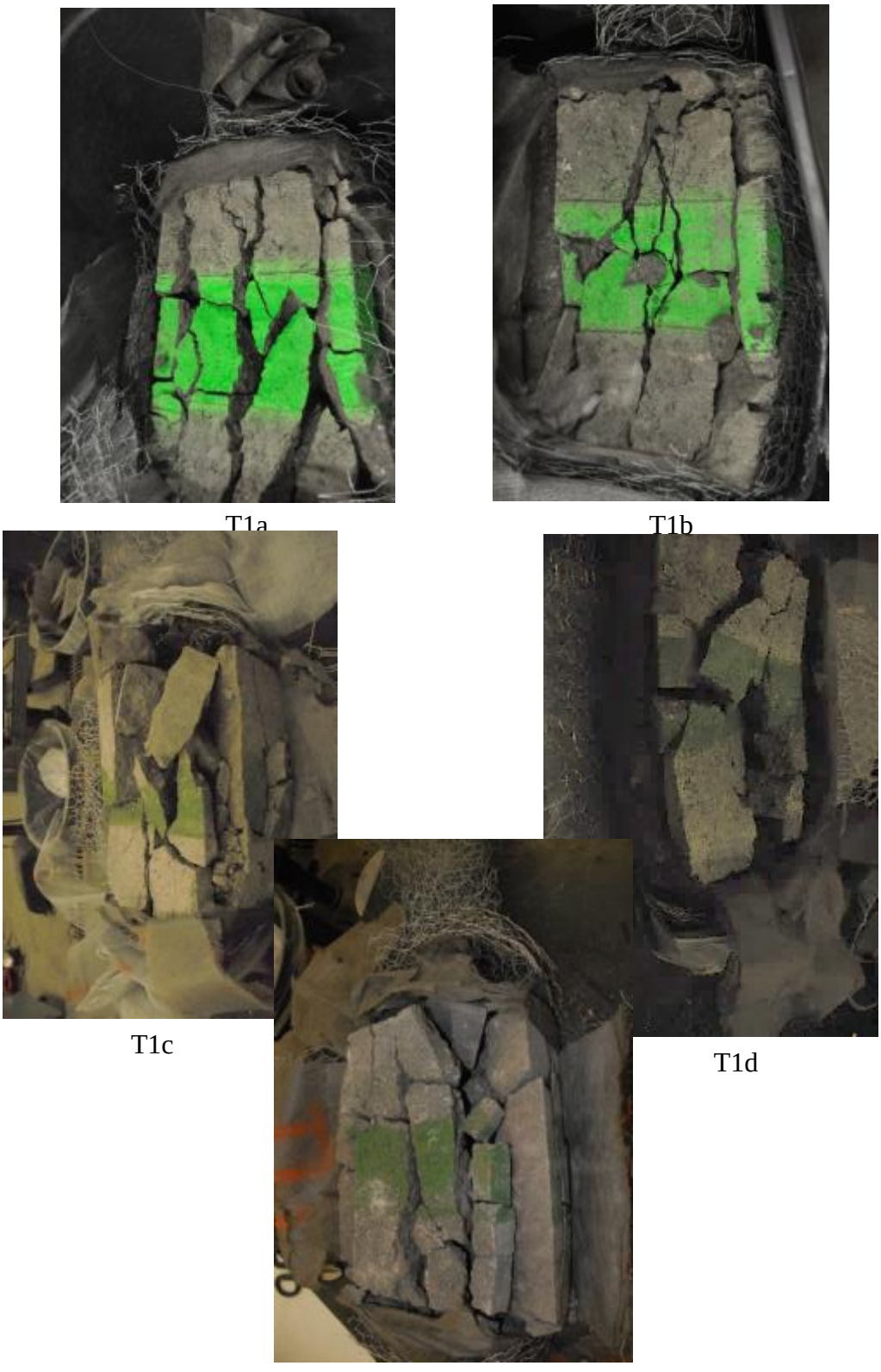

Figure 4-7: Unwrapped blocks for Test 1

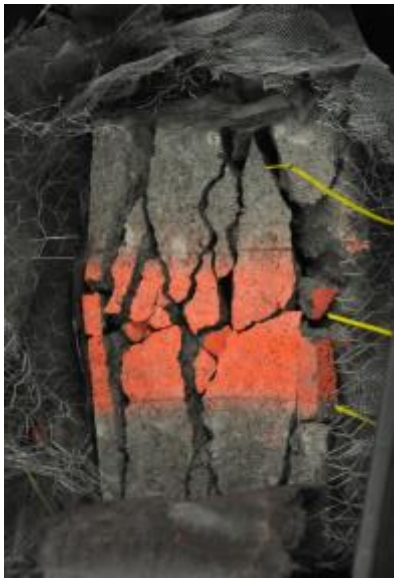

T2a

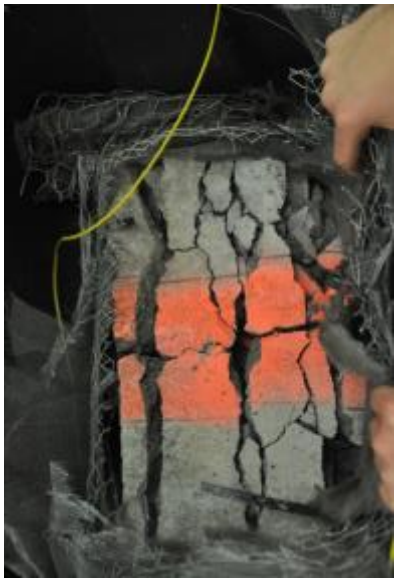

T2b

T2c

T2d

T2e

Figure 4-8: Unwrapped blocks for Test 2

Test 2 has the same radial crack formation, with an additional horizontal crack through the center, in all 5 cases, suggesting that fragmentation is influenced due to the collision of detonation waves in a single hole. Careful removal of larger fragments in stages resulted in Figure 4-9. It is clearly evident that smaller fragments are grouped around the blast hole in the compressive shock wave region. There is no evidence, however, of any smaller fragments occurring where the detonation waves collided.

Figure 4-9: Small fragments centered around the blast hole

4.3.1.2 Fragmentation Analysis

Particles were separated into small and large fragments to carry out the fragmentation analysis. Small particles were those smaller than 1.5 inches in size. These fragments were put through a series of sieves and the total of each size weighed individually (Figure 4-10). Fragments greater than 1.5 inches were placed on a table with appropriate scale and a picture taken to use with WIPFRAG photographic image fragmentation analysis. Figure 4-11 shows a picture of the large fragments for T1a both before and after WIPFRAG. The bottom picture in the diagram shows the output from WIPFRAG: percentage retained on each sieve, and a logarithmic plot of the fragmentation

information. The total weight of all fragments was recorded; the weight on each individual sieve could then be back calculated from the WIPFRAG analysis and combined with the small size fragments. A total of 14 sieve sizes were used from 16 inches down to 0.01 inches.

Figure 4-10: Small size sieve analysis

Tables 4-1 and 4-2 show the average particle size and percent passing for T1 and T2, respectively. The average particle size is the difference between consecutive sieves and used commonly in mineral processing. Figures 4-12 and 4-13 show the information graphically. Individual tests are shown in the bars and average percent passing for the tests shown as a line graph. It is immediately evident that the majority of fragments fall between 5.66 and 11.31 inches in size. Calculation shows that 62 % of fragments in Test 1 and 63 % of fragments for Test 2 fall between these sizes. Direct comparison between the two tests is most easily seen in Figure 4-14, where the average for each test is plotted against each other. The line graph in Figure 4-14 shows the ratio between T1 and T2, where T1 has been divided by the sum of both tests and represented as a percentage. A value greater than 50 % demonstrates a larger percentage of fragments have passed that average particle size in T1. Conversely, a value less than 50 % shows that T2 has a larger percentage of fragments passing that average sieve size. Increased, or optimum, fragmentation, described by a larger proportion of smaller fragments, can be determined through a percentage greater than 50 % demonstrating T2 has increased fragmentation and a percentage difference less than 50 % demonstrates T1 has the better fragmentation, at the particle size. Interestingly, results show that for all sizes less than 3.46 inches, T1

demonstrates increased fragmentation. For sizes above 3.46, T2 demonstrates increased fragmentation. Even though T2 has increased fragmentation in only 3 of the 14 sieve sizes, 75 % of the fragments fall in these sizes, indicating that overall T2 shows increased fragmentation.

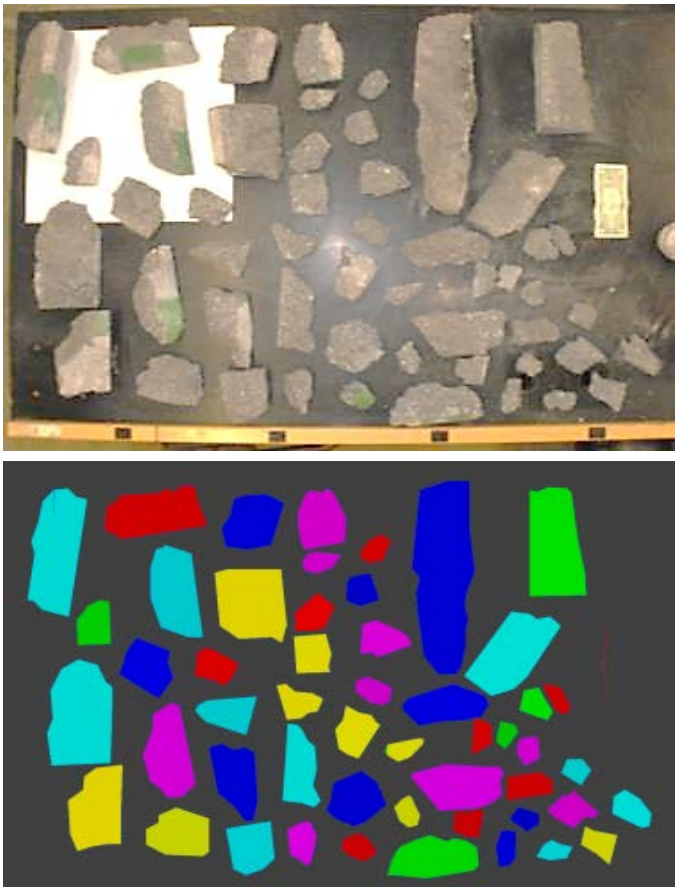

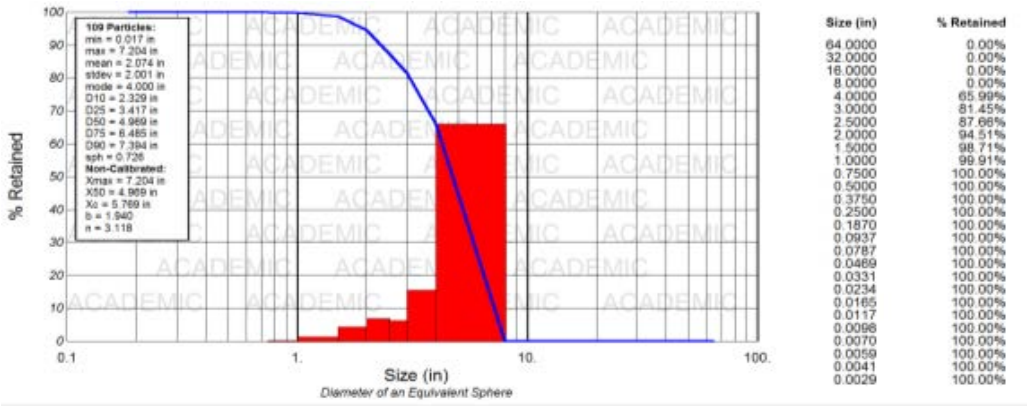

Figure 4-11: Large size sieve analysis

Table 4-1: Percent passing for Test 1

	% Passed					
Average Particle Size (in)	**T1a**	**T1b**	**T1c**	**T1d**	**T1e**	**Average**
16.00	100.00	100.00	100.00	100.00	100.00	100.00
11.31	100.00	100.00	91.59	100.00	94.49	97.22
5.66	42.64	39.51	32.06	31.37	31.50	35.41
3.46	27.08	29.25	25.04	22.84	22.50	25.34
2.74	20.50	20.10	18.41	17.86	18.76	19.13
2.24	15.08	18.10	12.10	11.92	12.96	14.03
1.73	13.29	9.57	10.54	9.87	10.48	10.75
1.22	9.38	7.66	9.51	7.70	9.16	8.68
0.87	7.47	6.54	7.43	6.36	7.03	6.97
0.61	4.85	4.13	4.93	4.13	4.40	4.49
0.35	-	-	2.52	1.98	2.96	2.49
0.17	0.89	0.79	1.11	0.83	1.36	1.00
0.05	0.14	0.15	0.21	0.16	0.27	0.19
0.01	-	-	0.08	0.06	0.10	0.08
Base	-	-	-	-	-	-

Table 4-2: Percent passing for Test 2

	% Passed					
Average Particle Size (in)	**T2a**	**T2b**	**T2c**	**T2d**	**T2e**	**Average**
16.00	100.00	100.00	100.00	100.00	100.00	100.00
11.31	100.00	100.00	100.00	100.00	100.00	100.00
5.66	38.13	48.64	39.25	27.24	32.81	37.21
3.46	23.63	28.84	26.81	18.03	21.72	23.81
2.74	17.81	21.58	20.89	15.77	17.98	18.81
2.24	11.39	16.69	12.87	9.28	13.56	12.76
1.73	7.45	11.11	10.27	6.77	8.82	8.89
1.22	6.20	7.92	8.63	5.97	8.31	7.40
0.87	5.32	6.98	6.52	4.69	5.92	5.89
0.61	3.88	5.02	4.64	4.23	4.46	4.45
0.35	-	-	2.33	2.20	2.49	2.34
0.17	0.85	1.16	0.94	0.96	1.10	1.00
0.05	0.14	0.21	0.18	0.19	0.21	0.19
0.01	-	-	0.06	0.06	0.06	0.06
Base	-	-	-	-	-	-

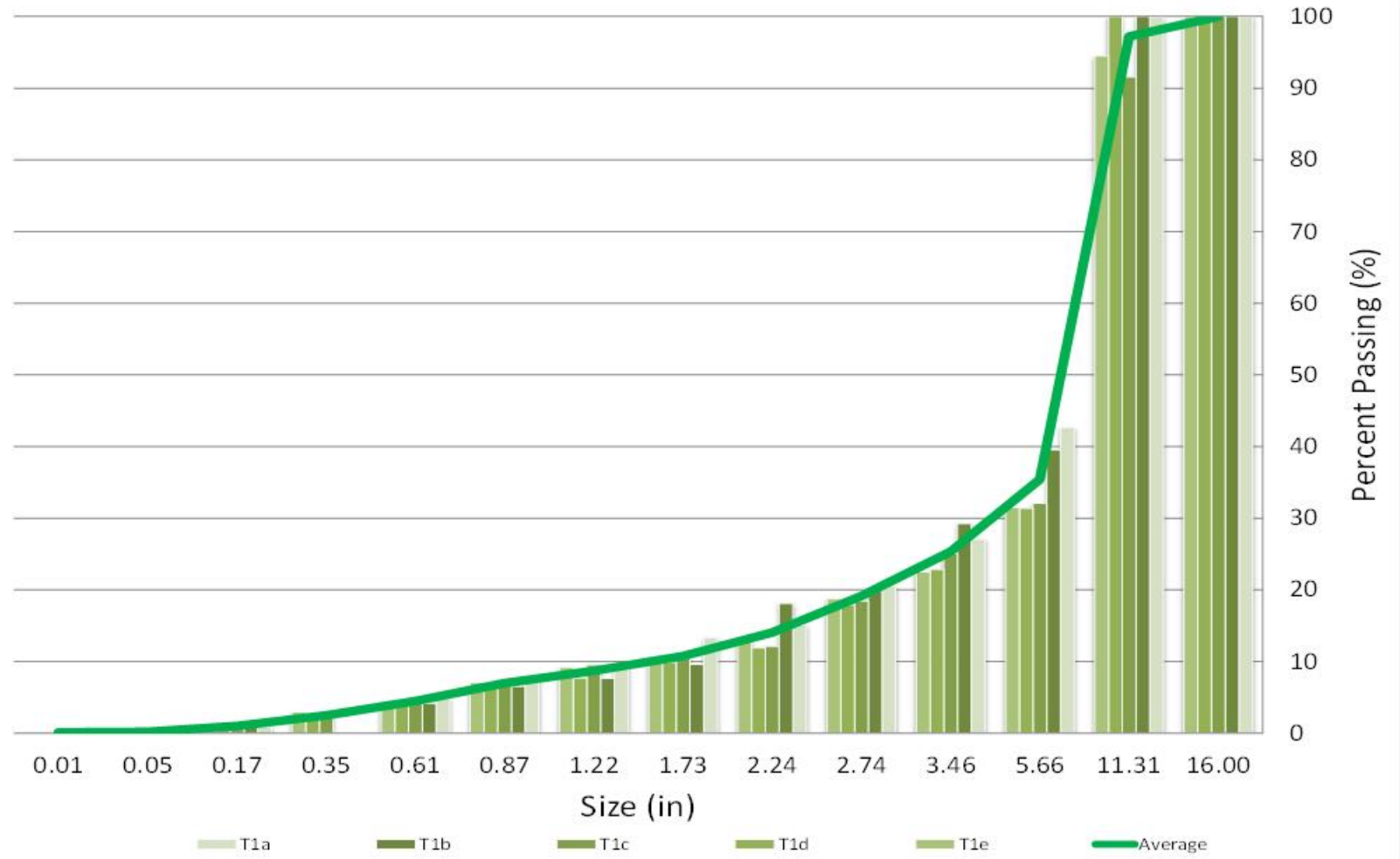

Figure 4-12: Percent passing for Test 1

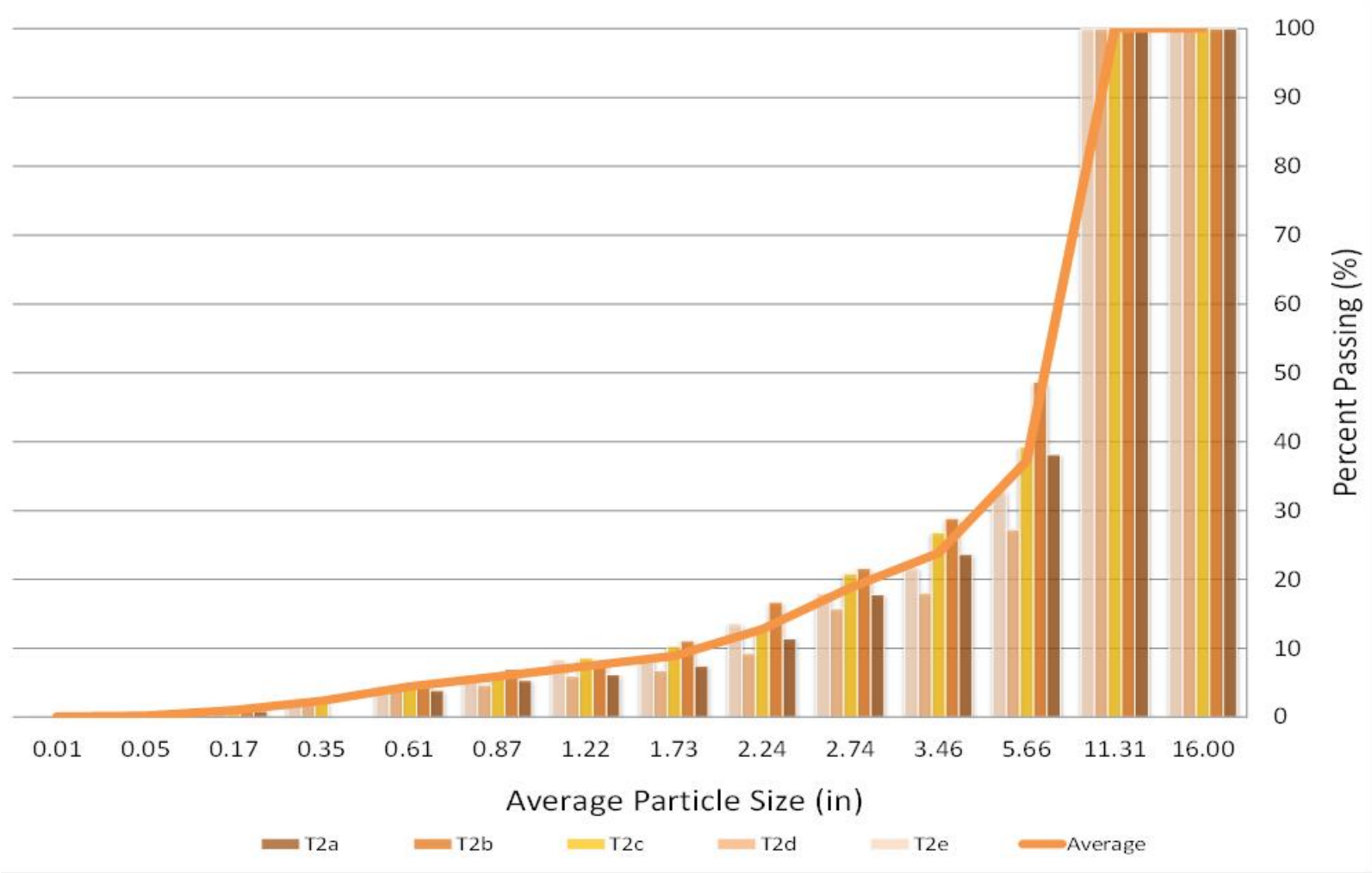

Figure 4-13: Percent passing for Test 2

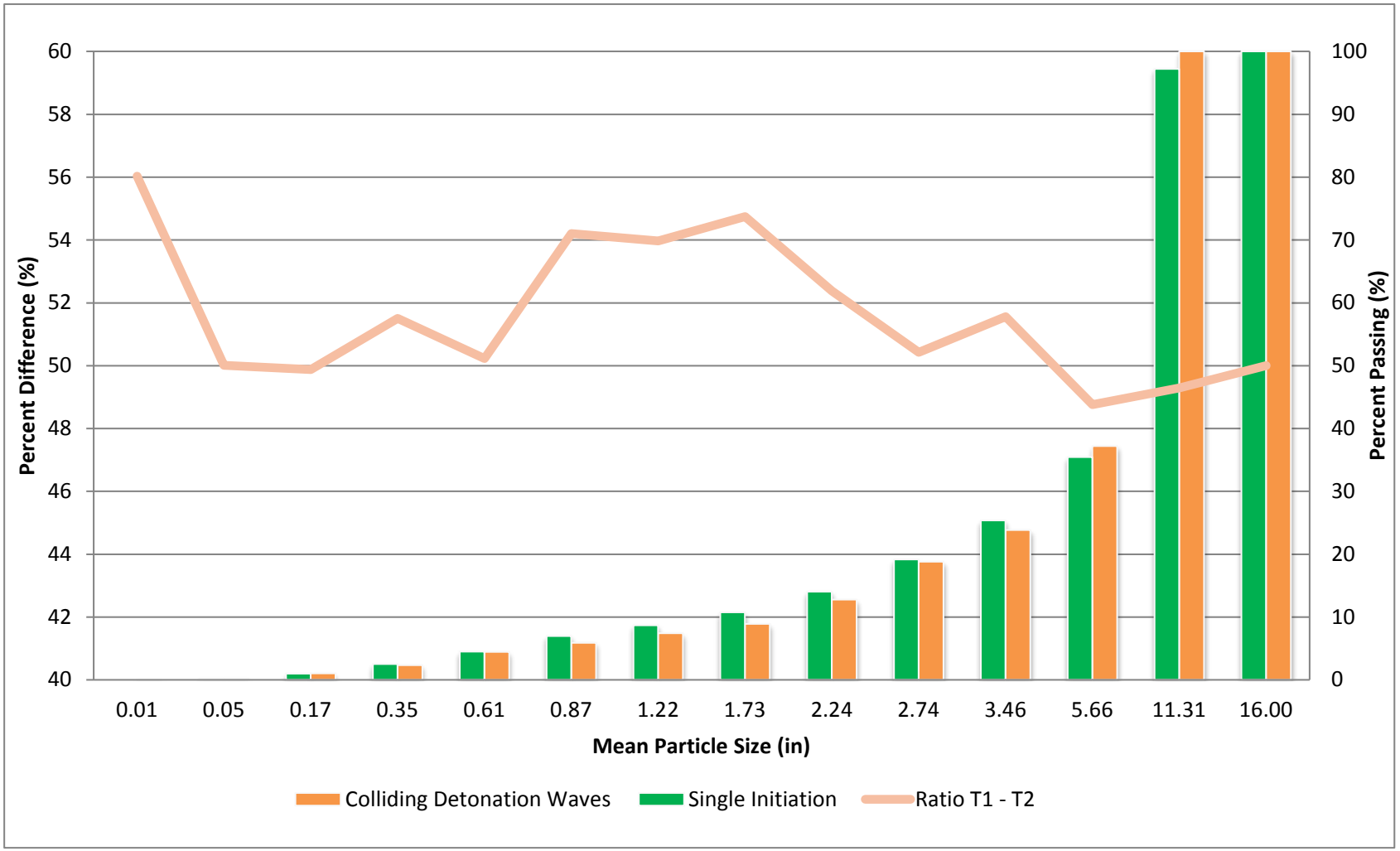

Figure 4-14: Average percent passing for Tests 1 and 2

The percentage of fragments passing both the 50 % (P50) and 80 % (P80) mark were calculated (Table 4-3). P50 is the size used in fragmentation models such as the Kuz-Ram and P80 is the typical size input used for mineral processing. P50 can also be called the median particle size. Similarly to that concluded from the graphical evidence, P50 for T2 is lower than that of T1, demonstrating an increase in fragmentation by 0.17 inches. Although this appears to be a small difference, scaled up to a full scale mining operation, significant saving could be made. P80 demonstrates the size fraction at which 80 % of particles pass; 6.88 and 6.71 inches respectively for T1 and T2. A small fragment size here would be ideal if processing of material requires very fine particle sizes. The smaller the size particle is already, the less the work required through secondary processing required. Again, the smallest average particle size is for T2.

Table 4-3: P50 and P80 for Tests 1 and 2

Test	P50 Size (in)	P80 Size (in)
T1a	4.51	6.61
T1b	4.69	6.68
T1c	5.21	7.22
T1d	5.09	6.83
T1e	5.17	7.08
T1 Average	4.93	6.88

Test	P50 Size (in)	P80 Size (in)
T2a	4.77	6.71
T2b	4.11	6.44
T2c	4.71	6.68
T2d	5.25	6.90
T2e	5.02	6.81
T2 Average	4.77	6.71

Explanation of the Kuz-Ram Fragmentation Model and all required equations are shown in Section 3.2: Fragmentation Modeling and Limitations. Below is the modified Kuznetsov equation and calculation for the small scale block tests. The rock factor is found from Table 3-1 where the blocks are described as totally massive, with close, horizontal joint spacing and a hardness factor of 6.

$$P_{50} = AK^{-0.8}Q^{\frac{1}{6}}\left(\frac{115}{RWS}\right)^{\frac{19}{20}} \quad (4\text{-}1)$$

Where x_m = mean particle size (cm); A = rock factor; K = powder factor (kg/m^3); Q = mass of explosive in the hole (kg); RWS = weight strength relative to ANFO, 115 being the RWS for TNT

$$P_{50} = 6 * 0.273^{-0.8}0.00405^{\frac{1}{6}}\left(\frac{115}{139}\right)^{\frac{19}{20}} = \underline{5.6528\ cm\ (2.2255\ in)}$$

The adapted Rosin-Rammler equation is used for the distribution fragmentation based on the calculated p50 size and uniformity equation 'n':

$$R_x = exp\left[-0.693\left(\frac{x}{x_m}\right)^n\right] \quad (4\text{-}2)$$

Where R_x = mass fraction remained on screen opening x; n = uniformity index, between 0.7 and 2.

Uniformity equation:

$$n = \left(2.2 - \frac{14B}{d}\right)\sqrt{\left(\frac{1+S/B}{2}\right)}\left(1 - \frac{W}{B}\right)\left(abs\left(\frac{BCL-CCL}{L}\right) + 0.1\right)^{0.1}\frac{L}{H} \quad (4\text{-}3)$$

Where B = burden (m); S = spacing (m); d = hole diameter (mm); W = standard deviation of drilling precision (m); L = charge length (m); BCL = bottom charge length (m); CCL = column charge length (m); H = bench height (m). (Cunningham, 1983)

Data input into equations 4-1 to 4-3 are shown in Table 4-4 while Figure 4-15 shows this information graphically compared to the experimental results for both T1 and T2.

Table 4-4: Input data for Kuz-Ram model

Input	Symbol	Value	Units
Rock Factor	A	6	
Powder Factor	k	0.46	lb/yd^3
Mass of Explosive	Q	0.00893	lb
Relative Weight Strength to ANFO	RWS	139	
Burden	B	7.875	in
Spacing	S	7.875	in
Hole Diameter	d	0.1875	in
Standard Deviation	W	0.1	in
Charge Length	L	15	in
Botton Charge Length	BCL	0	in
Collumn Charge Length	CCL	15	in
Bench Height	H	15	in

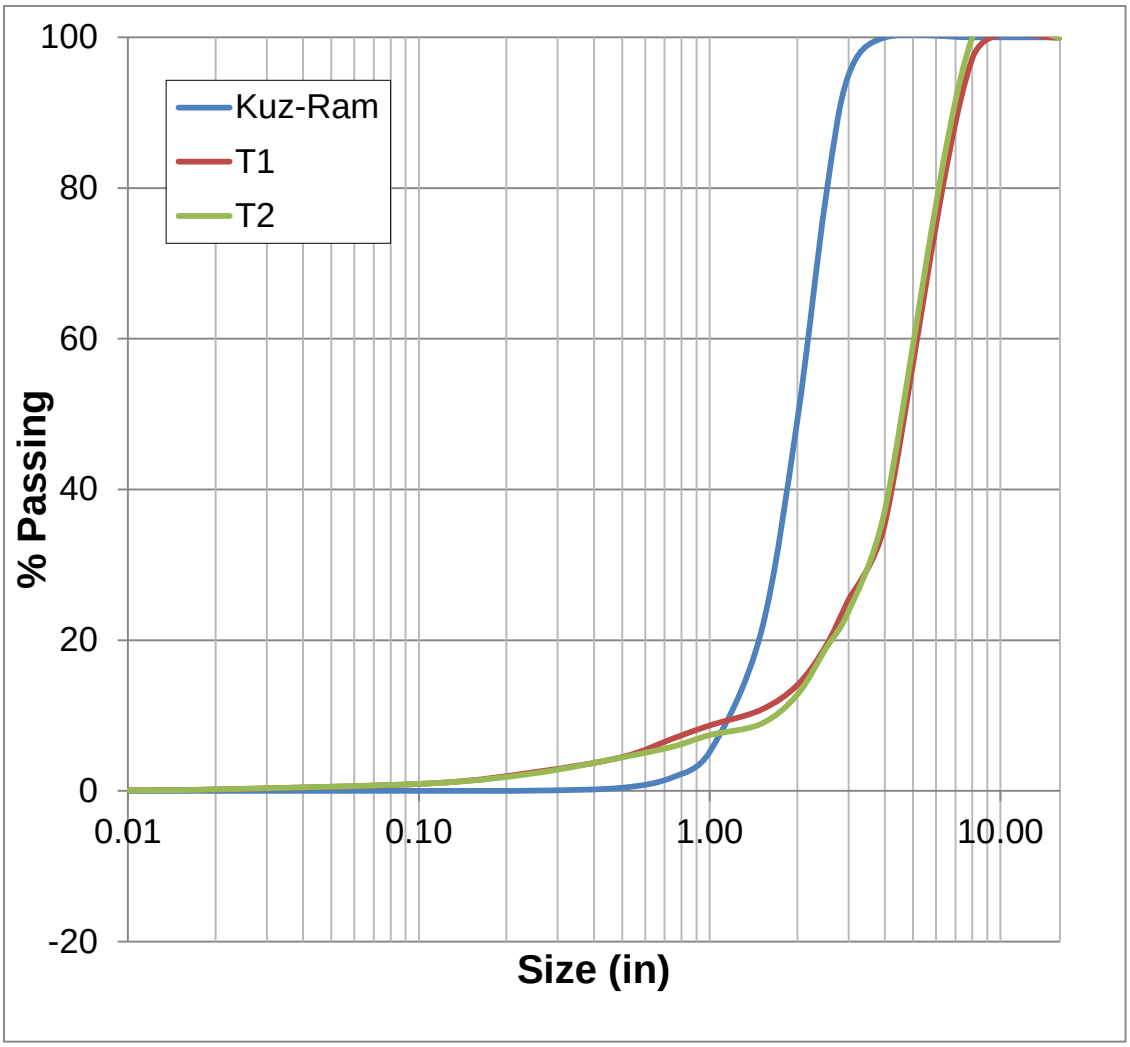

Figure 4-15: Fragmentation distribution of Kuz-Ram and experimental data, T1 and T2

The calculated average particle size is far smaller than that of the experimental results. The calculated P50 size is 2.23 in, compared to 4.93 in and 4.77 in for T1 and T2, respectively. This could be somewhat due to the escape of some of the gas pressure generating a larger fragment size, but the difference should not be that drastic. The curve of the Kuz-Ram model follows the experimental data very closely, suggesting that the problem with the Kuz-Ram model is not in the distribution but in the D50 calculation. Additional parameters for the fine and coarse fractions (Djordjevic, 1999) might not be necessary, but improvements in the calculation of the average particle size are. The average particle size influences the full Rosin-Rammler distribution. Figure 4-16 further emphasizes the discrepancy in calculated average particle size through the Kuz-Ram

model. It displays the same three curves as Figure 4-15 but the P50 size input into Equation 4-2 was 4.8 inches; the average P50 from T1 and T2. The match of the curve is very close, other than for the small size fractions. Attempt was made to reduce this difference using the concept by Djordjevic (1999) but the change was minimal. Matching the small size fractions is not of greatest importance due to the small volume of rock at this size. The steepness of the curve influences the quantity of particles at any one size. A steeper curve shows a larger percentage of your material distribution is of uniform size. It is this portion of the distribution that is important to match as this is where the majority of the particles lie.

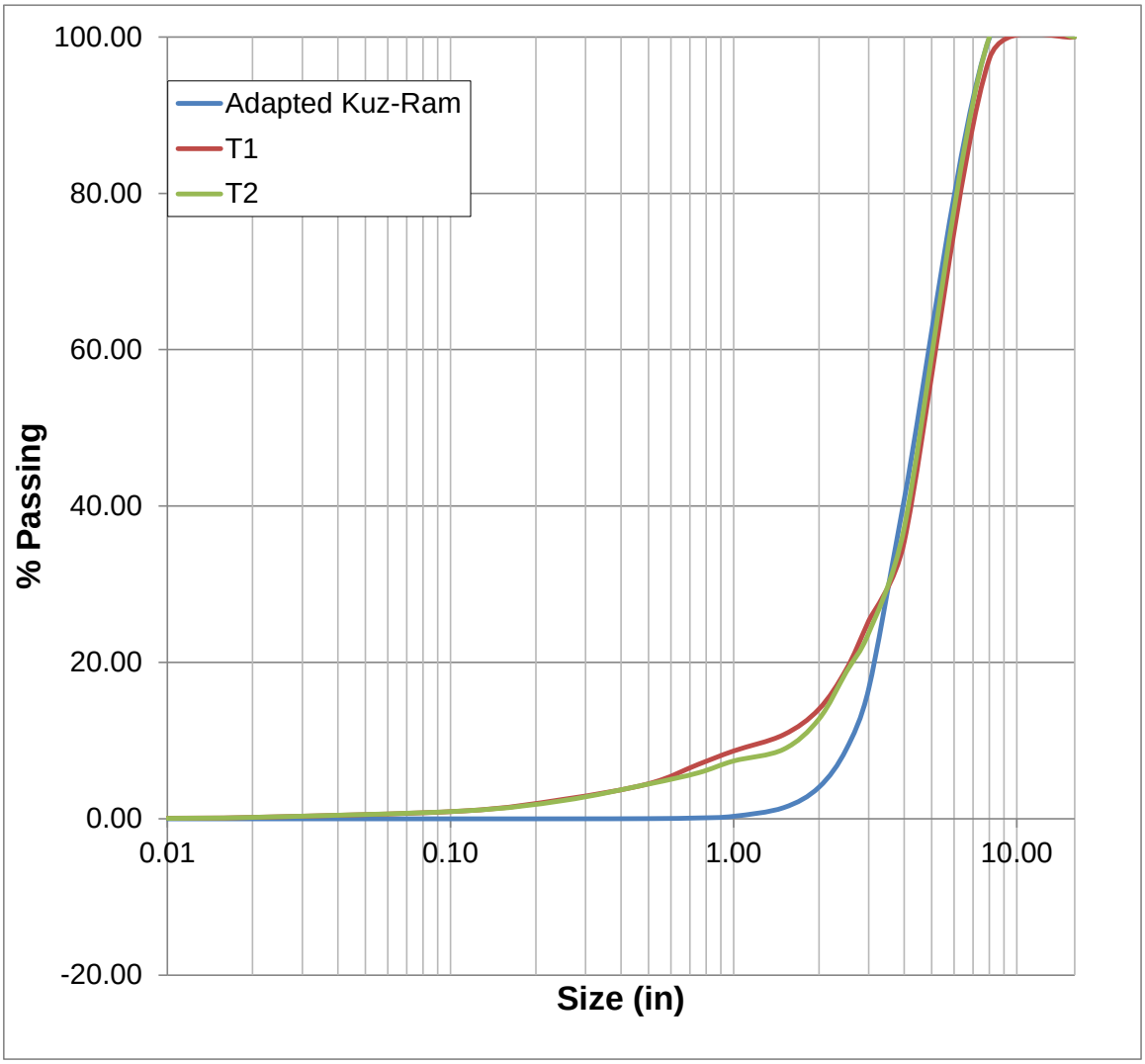

Figure 4-16: Adapted Rosin-Rammler curve with accurate P50 size

In additional to the limitations of the Kuz-Ram model found in literature, it is apparent that the model is not suitable for comparing to small scale experimental data with detailed fragmentation analysis. The only inputs to calculate the average particle size are powder factor, a rock factor unsuitable for massive materials, mass of explosive and relative weight strength of the explosive. Experimental tests show differing fragmentation due to initiation location. No additional input is available to insert in the Kuznetsov equation for the two different experiments. A single output is calculated that is far smaller than the average particle size found in the two experiments. This could be partly due to the decoupled explosive and no stemming, reducing the effectiveness of the gas pressure on the fragmentation process. Despite this, the difference is still drastic and only one average size can be found representing both tests.

4.3.1.3 High speed video Analysis

High speed video analysis was used to determine the timing of certain events in the fragmentation process, such as initial crack time and location, and throw of the material. The highest frame rate possible due to the intense lighting necessary for high frame rates compared to that of the underground quarry used was 250 fps. This gives a time per frame of 4 ms. The first 24 ms of high speed video footage can be seen in Figure 4-17 for both T1 and T2. The bright flash of color in the background is the excess detonating cord in air; T2 has double the amount of detonating cord outside the block, explaining the increase in fireball size. It is difficult to see any additional horizontal cracks through the center of the block in T2 due to the fireball engulfing the center of the blocks. What can be seen, however, is the bowing shape of the block about the center in T2 from 16 ms onwards compared to that of T1, indicating that a higher pressure is present at that location and throw of material from this point could be increased influencing results seen from a cast blast. Figure 4-18 shows the two tests zoomed in at 4 ms after initiation. The vertical cracks are clearly visible in both tests. The bright fireball detracts from the center of the block in T2 but the fact that the bright light is more visible through the block then in T2 could indicate a difference in fragmentation pattern at this location favoring that of T2.

Figure 4-17: First 7 Frames of high speed video footage for Tests 1 and 2

Figure 4-18: T1 and T2 after 4 ms

4.3.2 Test 3 – Shock Waves

Eight blocks were tested for T3 due to some inconsistencies gathered results. Again, visual, sieve and high speed video footage analysis were carried out. In addition to the eight blocks for T3 that have instantaneous detonation, six more blocks were tested where there was a change in initiation time created by altering the length of detonating cord either end of the block. The change in initiation time was used as an indication to the possibility of moving the resultant cracks due to wave collision through the blocks.

4.3.2.1 Visual Analysis

Figure 4-20 shows the eight unwrapped blocks for T3a-T3h. Consistency of the tensile crack distribution is not good as with T1 and T2. Five of the eight blocks (T3a, b, c, g and h) show indication of a horizontal crack where the colliding shock waves would meet in the center of the block, the remaining three blocks do not. The remaining three blocks have diamond shape formation where the pressure from the detonation has found its easiest path to a free face. The center crack in T3a is relatively wide, suggesting that significant pressure contributed to its formation. The remaining blocks with cracks through the center are not as prominent, falling apart further as the fragments were separated. This action would still occur in a production blast through secondary breakage as the fragments tumble to the pit floor.

Test T3a, the first to be viewed, showed promise to support the theory by Yamomoto (1999) and Rossmanith (2002) that the greatest fragmentation occurs where two shock waves meet. Test T3a is represented in Figure 4-19 with a pictorial demonstration of the Mach Angle calculation parameters. The left side of the figure shows the theoretical wave propagation and expansion following the detonation front. The right side of the figure shows the location of the Mach angle calculation variables: Mach angle, Sonic Velocity and Detonation Wave Velocity. Measuring all four angels and taking the average gives an average Mach angle of 23 degrees (°).

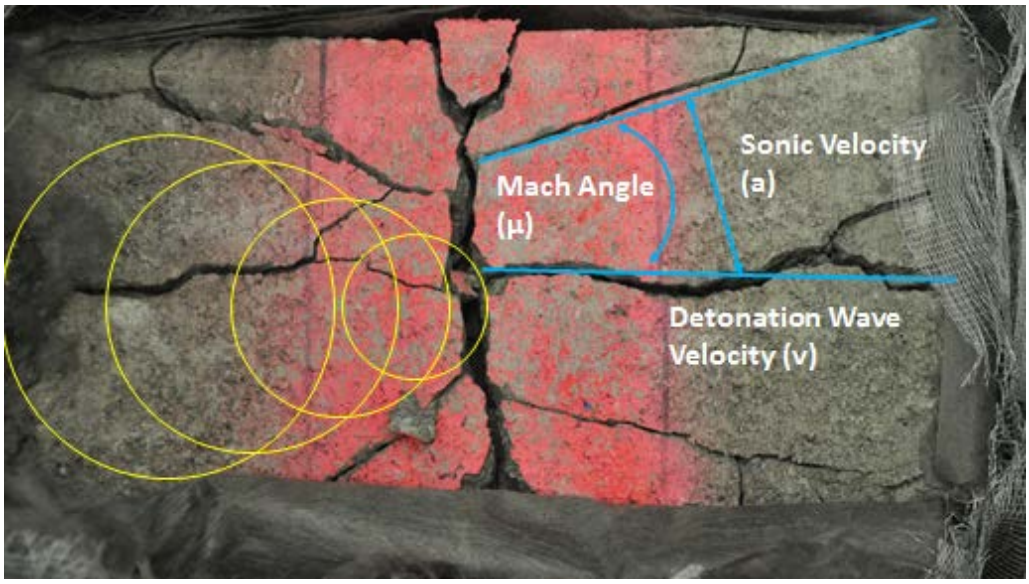

Figure 4-19: Mach Angle Representation for T3a

Equation 4-4 shows the Mach Angle formula:

$$sin\mu = \frac{a}{v} \qquad (4\text{-}4)$$

When the equation was applied to the manufacturers detonating cord VoD of 23,000 ft/s (Dyno, 2014), and a range of Concrete sonic velocities from 10500 – 11800 ft/s (Engineering Toolbox, 2014) a range Mach angles came out as 27-31°. The measured angle after detonation was 23°. Initial thoughts were promising, but the discrepancies in the Mach angle differences and only one of the eight tests showing visible signs to sonic wave interaction in this manner, further investigation was unnecessary.

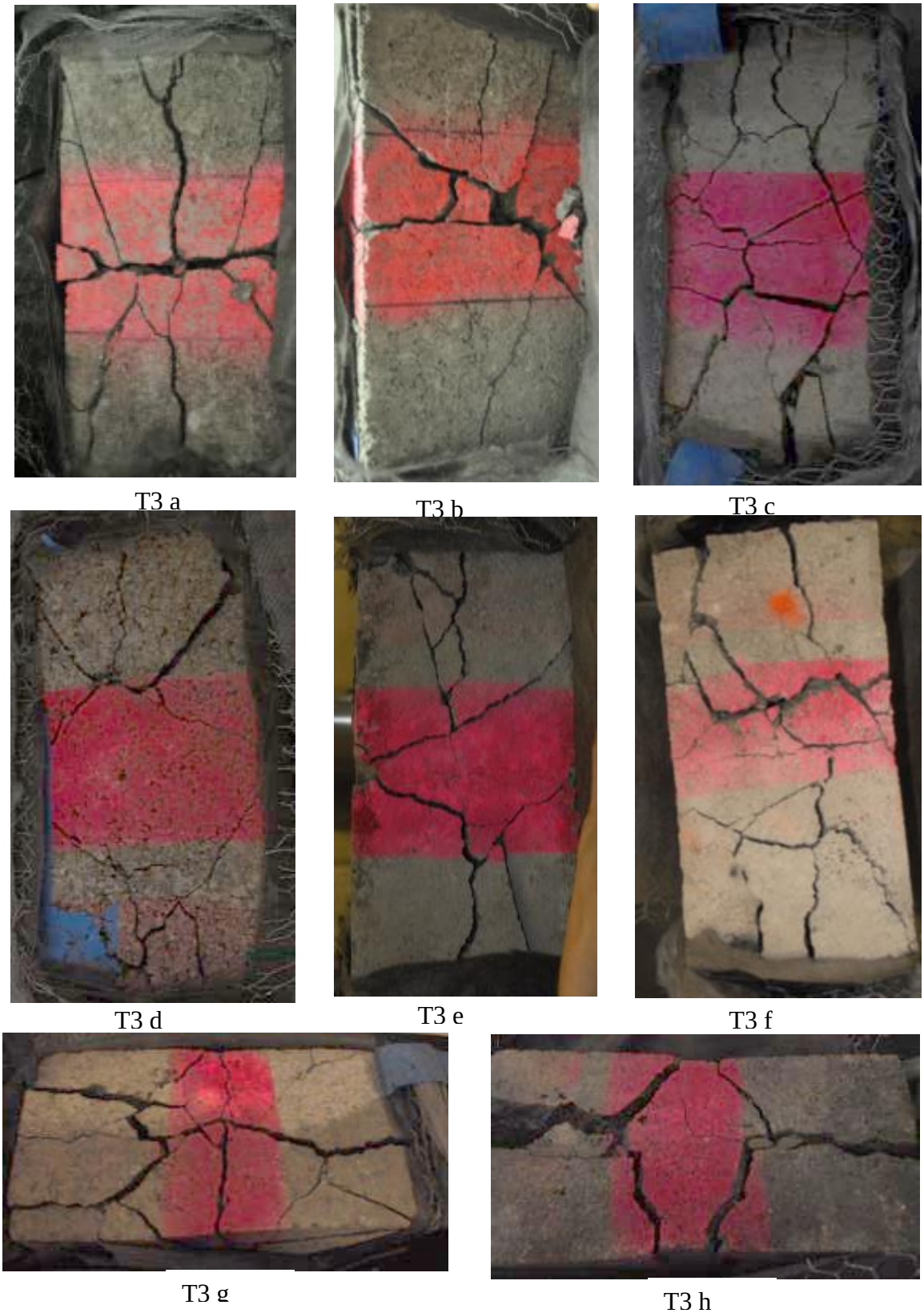

Figure 4-20: Unwrapped Blocks for Test 3

Figure 4-21 and Figure 4-22 show partly unwrapped blocks for a representative block where a center line crack is formed and one where it has not. In both cases, the largest fragment is found in the center where no explosive is present but where the shock waves collide, opposing the hypothesis by Yamamoto et al (1999) and Rossmanith (2003). In the case where a center line crack has formed, any gas pressure that could be used to extend hairline cracks has escaped and no further work gone into fragmentation. Essentially, what the shock collision has achieved is an easy escape for the gas pressure and reduction in fragmentation.

Figure 4-21: Top: straight crack through the center of T3c; Bottom: large fragment from the center of the block

Figure 4-22: Largest fragment from the center of T3h

Rossmanith (2002) stated that the position of the increased fragmentation zone can be changed by altering the timing between detonation columns. Figure 4-23 shows three additional tests where the length of detonating cord at one end was increased by 2, 4, or 6 inches to alter the location of wave collision. The yellow line represents the location at which it is predicted the waves will meet and additional fragmentation be present at that location. The distances off center are 1, 2, and 3 inches, reasoning behind the names T3+1 etc. Results show no evidence of fragmentation change in any of the six tests at the specified location, or any correlation between the tests. Fragmentation was still analyzed and discussed in the following sections.

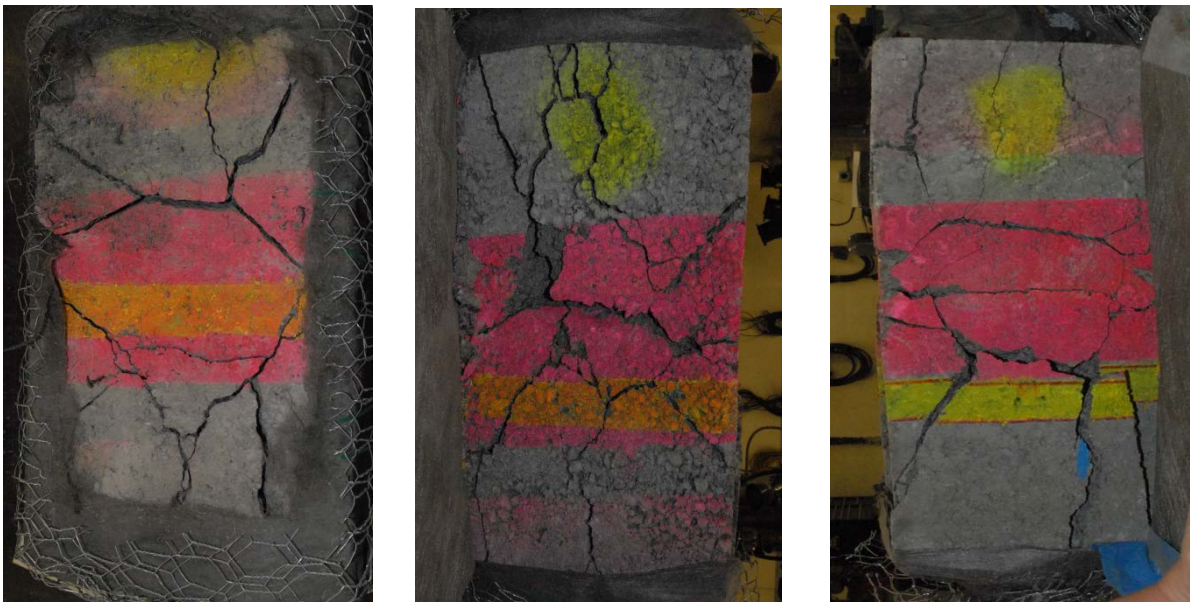

T3 +1a T3 +2a T3 +3a

T3 +1b T3 +2b T3 +3b

Figure 4-23: Timing effects on shockwave collision

4.3.2.2 Fragmentation Analysis

Sieve analysis was carried out for all 14 blocks in T3. Table 4-5 shows the fragmentation distribution for all 8 tests with instantaneous distribution which is shown graphically in Figure 4-24. Significant variation is present between tests, making any firm conclusions from them difficult to attain. The Average P50 and P80, shown in Table 4-6 are 5.63 and 7.21 inches, respectively. This value is understandably higher than either value

found in tests 1 or 2, due to the decrease in powder factor. A significant portion of the fragments again fall between the average particles sizes 5.66 and 11.31 inches.

Table 4-5: Fragmentation distribution for T3

	% Passed								
Average Particle Size (in)	**T3a**	**T3b**	**T3c**	**T3d**	**T3e**	**T3f**	**T3g**	**T3h**	**Average**
16.00	100.00	100.00	100.00	100.00	100.00	100.00	100.00	100.00	100.00
11.31	100.00	100.00	100.00	88.25	86.30	100.00	100.00	85.61	95.02
5.66	25.39	18.18	24.24	15.60	10.89	20.62	24.85	14.38	19.27
3.46	15.23	13.01	10.54	10.79	4.18	10.86	15.14	8.67	11.05
2.74	12.36	11.93	9.62	6.84	3.10	6.17	10.15	3.77	7.99
2.24	8.88	9.21	8.34	5.00	2.56	4.14	5.58	3.08	5.85
1.73	4.07	5.89	4.45	2.94	2.09	2.64	3.88	2.45	3.55
1.22	1.81	2.15	3.25	1.63	1.66	2.37	2.22	2.19	2.16
0.87	1.73	2.05	2.51	1.48	1.46	1.89	1.62	1.76	1.81
0.61	1.35	1.61	1.79	1.12	1.20	1.29	0.97	1.27	1.33
0.35	-	-	1.02	0.67	0.67	0.67	0.46	0.67	0.69
0.17	0.37	0.38	0.44	0.33	0.29	0.30	0.14	0.33	0.32
0.05	0.06	0.06	0.09	0.09	0.05	0.06	0.09	0.08	0.07
0.01	-	-	0.03	0.04	0.01	0.02	0.02	0.03	0.02
Base	-	-	-	-	-	-	-	-	-

Table 4-6: P50 and P80 for T3

Test	P50 Size (in)	P80 Size (in)
T3a	5.32	6.93
T3b	5.56	7.02
T3c	5.36	6.94
T3d	5.89	7.55
T3e	6.07	7.67
T3f	5.48	6.99
T3g	5.34	6.94
T3h	6.00	7.68
T3 Average	5.63	7.21

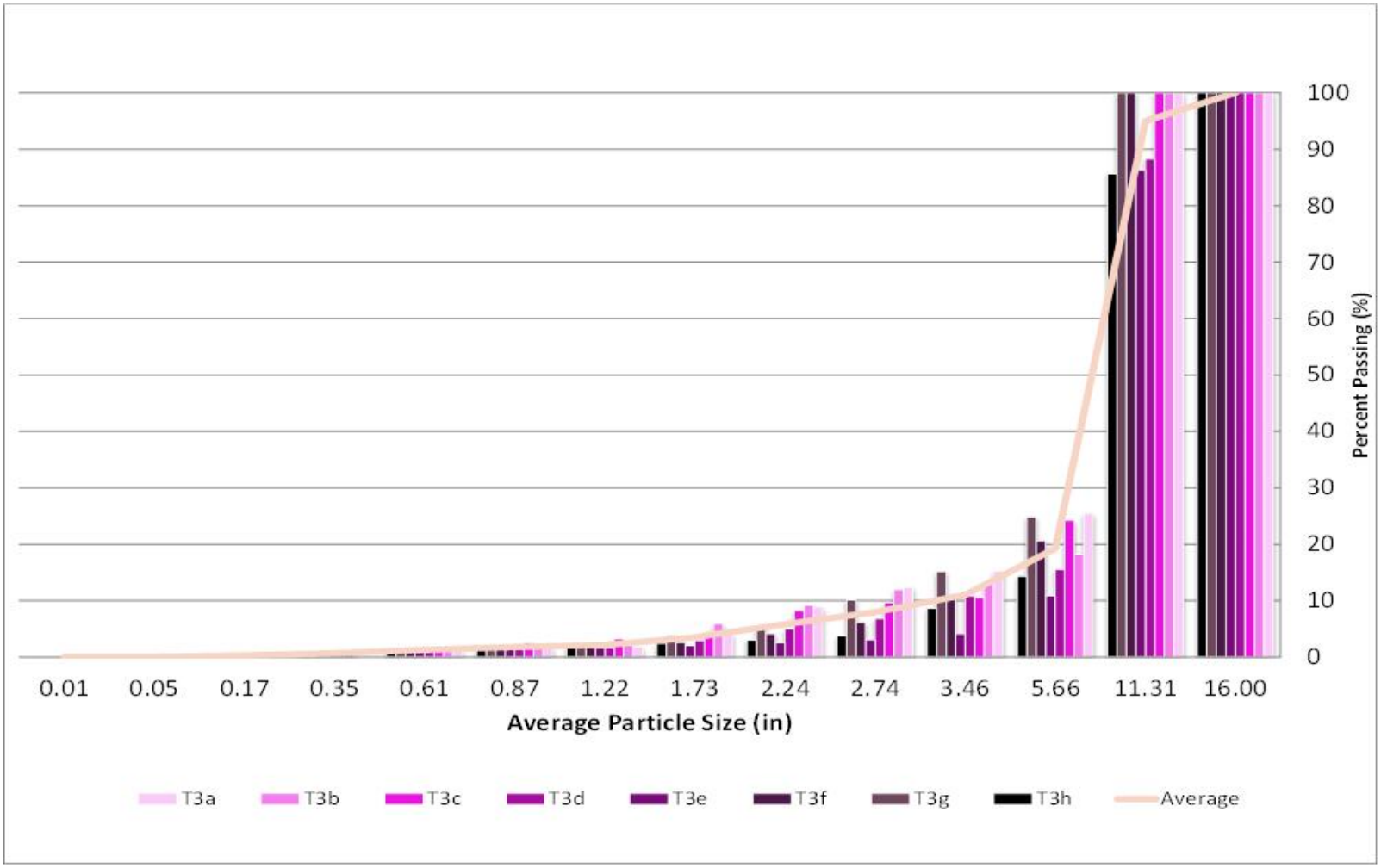

Figure 4-24: Fragmentation distribution for T3

Test 3 utilizing instantaneous detonation was compared to the fragmetnation distribution where timing was altered. Fragmetnation distribution is shown in Figure 4-25 and average P50 and P80 in Table 4-7. For T3+3, the location of predicted collision actually occurs while one side of the detonation is still in action, fragmetnation for this test has decreeased from that of instantaneous detonation. The test with the lowest P50 is that of T3, instantaneous detonation but no strength is held in this concluding statement.

Table 4-7: Average P50 and P80 for T3

Test	P50 Size (in)	P80 Size (in)
T3 Average	5.63	7.21
T3 +1 Average	6.05	7.67
T3 +2 Average	5.64	7.06
T3 +3 Average	5.99	7.56

Figure 4-26 shows the T3 distribution with that of the calculated Kuz-Ram model. The average particle size, again, is much lower than that found experimentally but the curve of the distribution an accurate depiction. The Kuz-Ram calculation for average particle size was 3.08 in compared to 5.63 found experimentally.

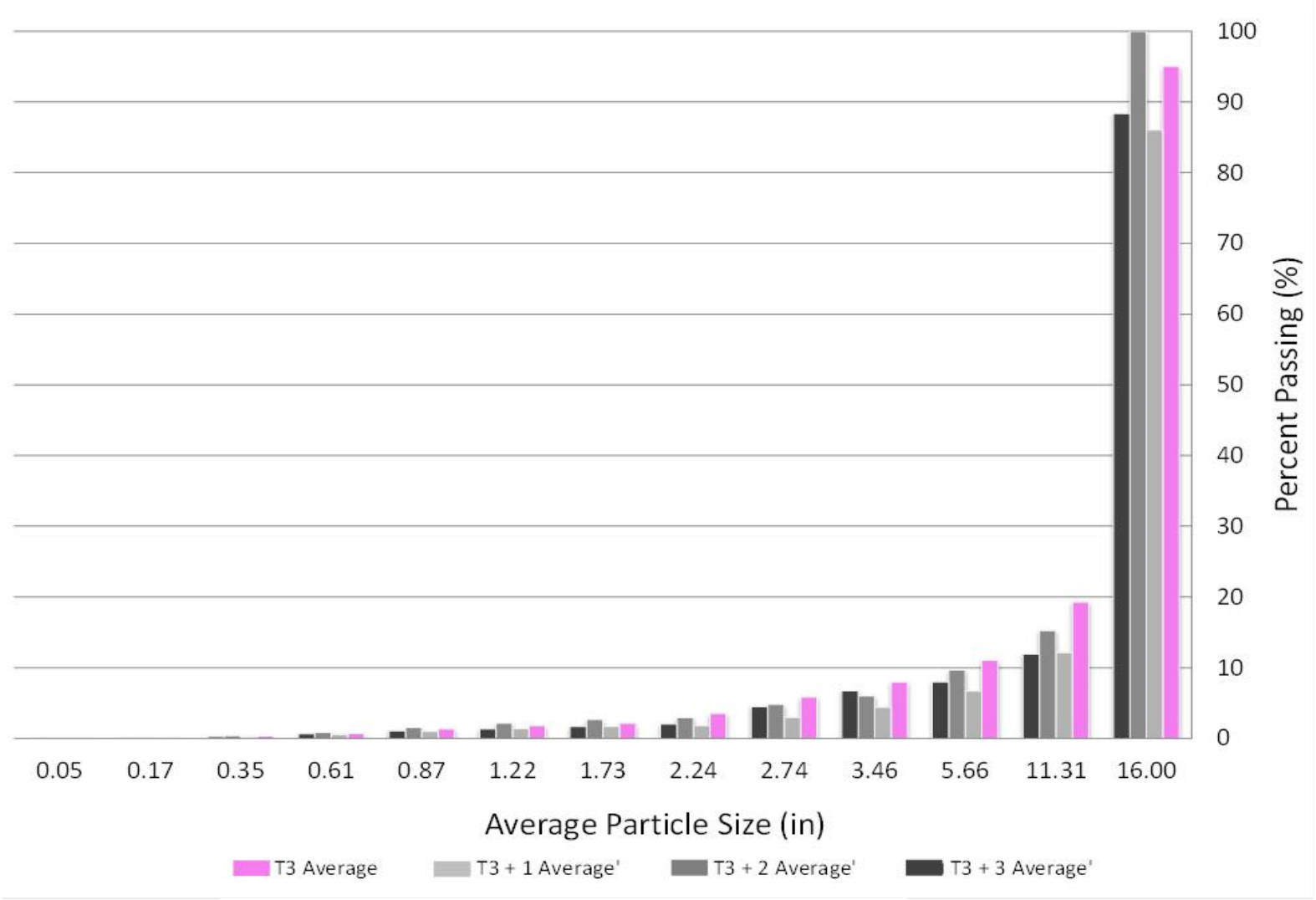

Figure 4-25: Average fragmentation distribution for T3

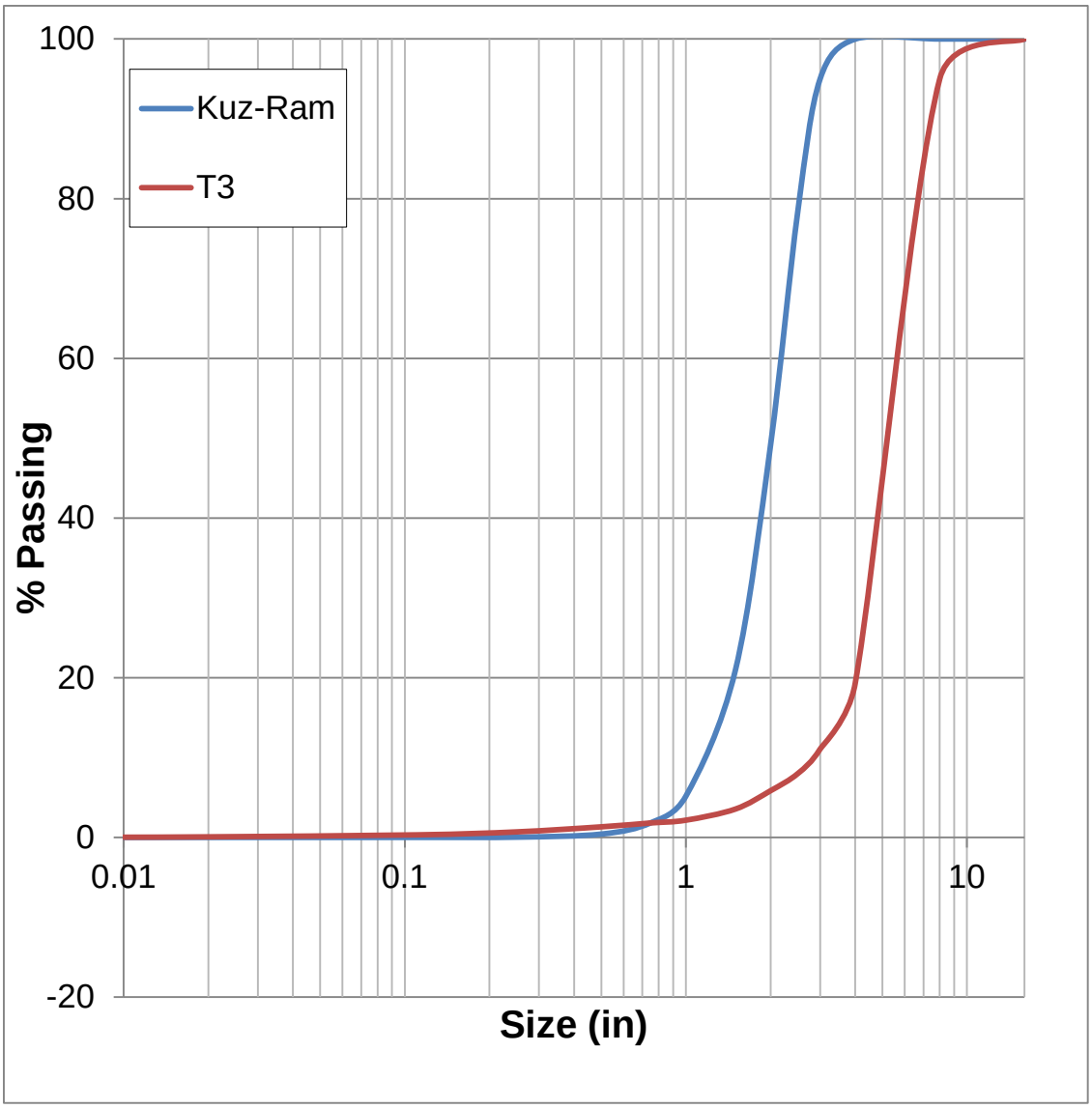

Figure 4-26: Fragmentation distribution of Kuz-Ram and experimental data, T3

4.3.2.3 High Speed Video Analysis

Figure 4-27 shows T3 recorded on high speed video after 4 ms. It can be seen that there are two clear tensile cracks visible, both vertically, and horizontally through the center of the block. Fragmentation beyond this was minimal, suggesting that the shock collision did not improve fragmentation, but hinder it by allowing the gas pressure to escape rather than expanding through smaller fractures in the block. Due to the inconsistency in the 8 other blocks tests, it is expected that this would not be representative of all blocks recorded in this way.

Figure 4-27: High speed video capture after 4 ms for T3.

4.4 Conclusion

Unique experiments have been carried out simulating a single blast hole where the collision of detonation waves, as well as shock waves, have been investigated. The experimental method was successful for fragmentation distribution studies with no major problems arising through consecutive tests.

Evidence through visual analysis of the exact location of tensile cracks, fragmentation and high speed video footage all show increased fragmentation where detonation waves collide through strata to a scenario where no wave collision occurs. Comparison to the Kuz-Ram model is a close fit to the distribution of fragment sizes, but not the average particle size. Additionally, there was no added input in the Kuz-Ram model to account for the difference between T1 and T2. A more accurate representation of calculating the average particle size is necessary.

Experimental investigation on shock wave collision showed a lack of repeatability through tests in both the fragmentation distribution and tensile crack distribution. Attempt was made to correlate these tests to shock theory in air through the Mach number. A close comparison of 23 degrees experimentally compared to 27 degrees mathematically was found for one of the eight tests. Although a significant finding, this was the only block in which a measurement could be established so it is not a reliable design tool for large scale blasting practices. Timing changes were applied to test the theory that the position of areas of increased fragmentation will change with timing. This observation was not found. Blocks tested have shown horizontal cracks through the center of the block where the two shock waves would collide, but confidence in the repeatability of this phenomenon deem the theory put forward by Rossmanith (2002) unreliable.

Chapter 5. Model Set Up and Parameter Selection

ANSYS Autodyn and Explicit Dynamics finite element modeling solvers were used to simulate the experiments described in Chapter 4. Three models were run, simulating the single initiation, dual initiation and colliding shock wave tests. As in the experiments, PETN was used as the explosive, compressive strength tests were carried out on the blocks to determine the material properties. A series of iterations were carried out to determine the most appropriate solver, material characterization, mesh distribution and computational cost. A series of videos, pictures, and stress and pressure values at individual points throughout the blocks were documented and analyzed in Chapter 6. The following Chapter outlines solver capabilities, the inputs into ANSYS, and the decision process on how they were made.

5.1 Concrete Block Material Properties

Compressive strength tests were carried out on three cylindrical samples, cored from the solid masonry blocks (Figure 5-1). Tests followed that of the standard test method for Compressive Strength of Cylindrical Concrete Specimens: ASTM-C39/C39M. A 2 inch outside diameter core drill was used for the three samples then the top and bottom ground down to create a smooth surface. The Testing Machine (Figure 5-2) applied a compressive axial load until failure. Compressive strength is simply the maximum load of the specimen divided by the cross sectional area of the specimen. Compressive strain versus compressive stress is plotted graphically in Figure 5-3 and exact values for density, maximum load and compressive strength are shown in Table 5-1. An average compressive strength was found to be approximately 10,000 psi (70MPa) which is typical for a high strength concrete, but also lies in the range of compressive strength for sandstone, shale and limestone; very common strata in surface mining and quarry operations (Brown, 1981)

Figure 5-1: Concrete blocks being cored

Figure 5-2: Testing Machine and inserted core sample

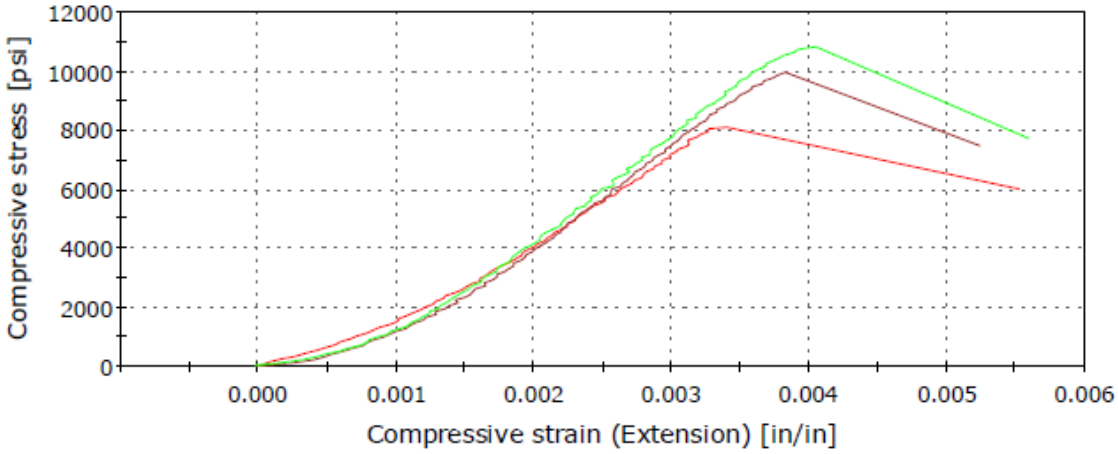

Figure 5-3: Compressive strain versus compressive stress for the three core samples.

Table 5-1: Material properties for three core samples

	Diameter (in)	Density (lb/ft^3)	Maximum Load (lbf)	Compressive Strength (psi)
1	1.72	149.8	18,821.0	8,100.2
2	1.73	147.1	23,367.3	9,940.9
3	1.73	149.0	25,397.9	10.804.8
Mean	1.727	148.6	22,528.7	9,615.3

5.2 Explicit Dynamics and Autodyn Solution Methods

Solutions in both Explicit Dynamics and Autodyn are solved in both time and space. Time is split into a number of much smaller time steps, or cycles. Large geometry is split up into a number of small elements, or cells, in either 2D or 3D known as a mesh. Structured, unstructured and mesh free cells are available. Two types of solver can accurately compute the resultant pressures of blast impact, Lagrange and Euler (Lusk et al, 2008, Preece and Lownds, 2008).

Lagrange solvers contain a mesh that distorts with the forces applied to it from a neighboring cell. This type of solver is ideal for pressure history definition for a solid material, or rock strata in the case of a bench blast. Too much deformation can distort cells, increasing solution time significantly, more often terminating the solution (Figure

5-4). For this reason, high pressure gasses and liquids are not suitable for Lagrange solvers. Lagrange grids can be modeled in Explicit Dynamics using the geometry modeler.

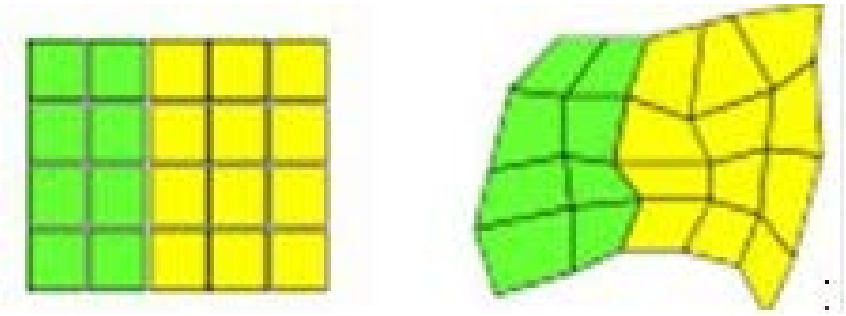

Figure 5-4: Original state (Left) and distorted (right) Lagrangian Mesh (ANSYS, 2014)

A good example of a fully Lagrangian solution is a projectile impacting a target. The space between the two solids does not need to be modeled or contain a mesh; only the interaction between them is calculated. (Figure 5-5). Parts of the grid can be eroded upon material or strain failure and the energy from it transferred to an adjacent cell, reducing the degree of deformation in the model. The solid masonry blocks are assigned a Lagrangian Solver.

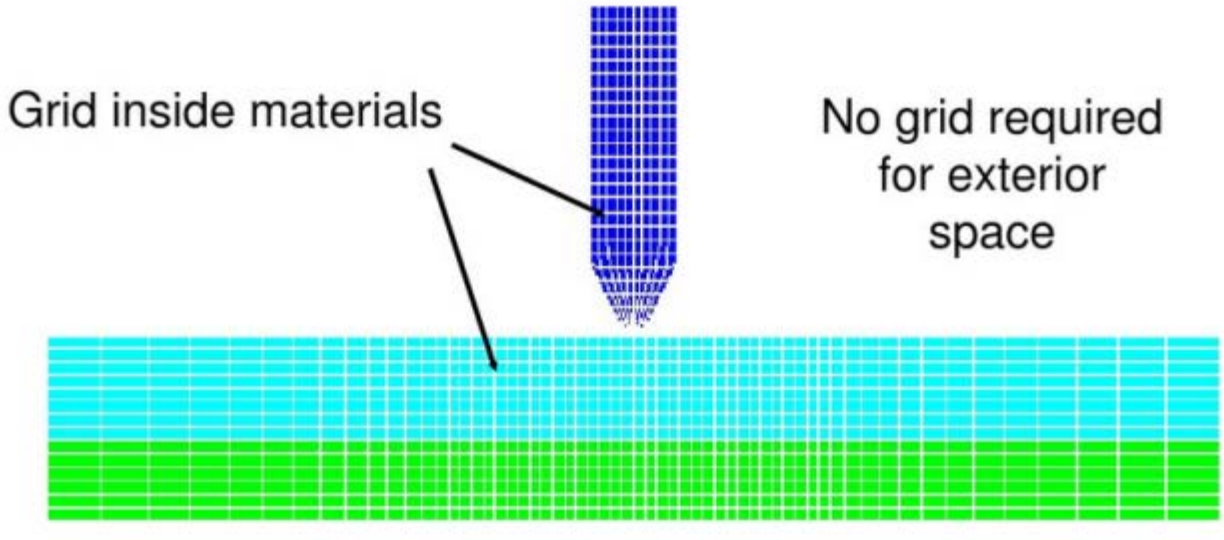

Figure 5-5: Two Lagrangian grids interacting (ANSYS, 2009)

A Euler solver has a fixed mesh with material flowing freely inside of the mesh without deformation. (Figure 5-6) This type of solver is more suited to materials with significant movement, such as that of an explosive. Computational time is greater than that of a Lagrangian solver and can only be run in Autodyn.

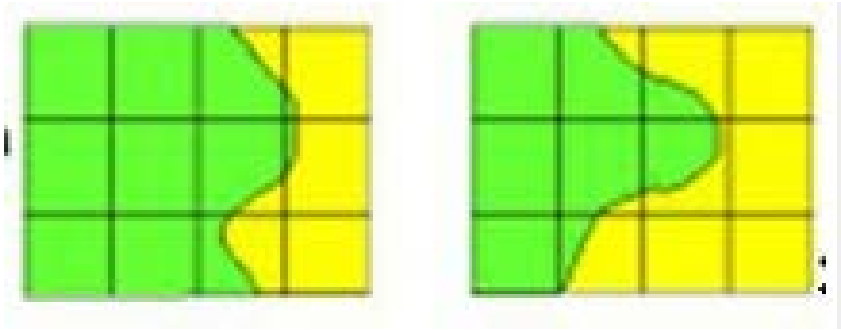

Figure 5-6: Materials flowing freely through Eulerian mesh (ANSYS, 2014)

The space between two Eulerian meshes also needs a mesh to allow the gas or liquid to flow through the space, cell to cell, unlike the Lagrangian solver. The explosive, PETN, was assigned an Eulerian Solver in all simulations.

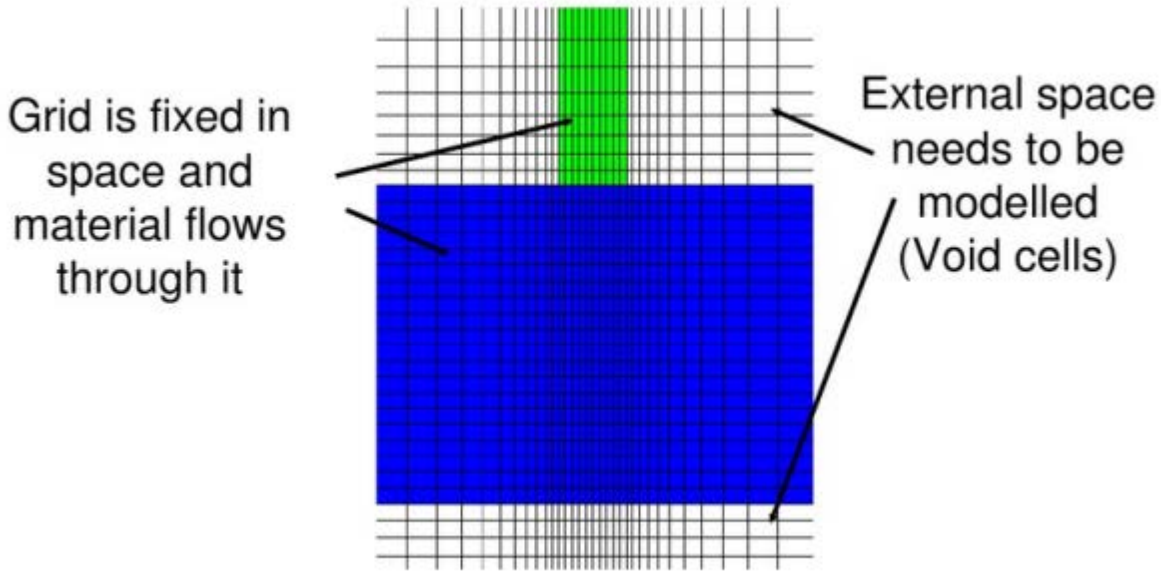

Figure 5-7: Two Eulerian grids with a void space grid in the free space (ANSYS, 2009)

The two solution types can be applied to the same simulation and each part assigned a different solver. Both Explicit Dynamics and Autodyn need to be used for this, the

Lagrangian parts modeled first in Explicit Dynamics and then transferred to Autodyn to add the Eulerian parts. If any Eulerian parts are incorporated in the model then Autodyn is the only system that can run the model. Lagrangian parts can also be modeled in Autodyn but the more advanced geometry modeler associated with Explicit Dynamics allows for more complex shapes and advanced grid systems to be modeled.

5.3 Material models

A number of material models are available within ANSYS due to the different phenomena that may need to be modelled for any given material. Non-linear pressure response, strain and strain rate hardening, thermal softening, directional material properties, damage due to crushing or tensile failure might need to be modelled, often multiple phenomena per project. Materials can deform either by a change in volume (volumetric response) or a change in shape (deviatoric response), therefore two material models are input for any given material, an equation of State (EOS) and a strength model to satisfy the two deformation criteria, respectively.

The concrete block used the RHT material strength model. This decision was based on the multiple successful models published by Preece and Lownds (2008), Lusk et al (2008) and Zhu et al, amongst others. The RHT failure model was also applied to the block, since we know that the material will eventually fail due to the extensive pressures exerted by the explosive. The EOS used for detonation product expansion is the Jones, Wilkins and Lee (JWL). It is the model used by Preece and Lownds (2008) who modeled an explosive column of emulsion coupled to a Lagrangian solid material.

5.3.1 RHT Material Strength Model

The Riedel, Hiermaier and Thoma (RHT) concrete strength material model is a commonly used model for brittle or granular materials, including that of blasted material. Zhu et al (2007), Preece and Lownds (2008), Borrvall and Riedel (2011) Lu et al (2005), Riedel and Mayrhofer (2008) and Lusk et al (2008) all use the RHT material strength model for blast response. Riedel et al (1999) developed the RHT model. The equations used in ANSYS are demonstrated below.

Dynamic loading of brittle materials are calculated using both plasticity and shear damage models, limited by a deviatoric stress failure using Equation 5-1. The RHT model is modular, allowing individual parts of the equation to be turned off, increasing its usage. Pressure hardening, strain hardening, strain rate hardening in tension and compression, third invariant dependence for compressive and tensile meridians, strain softening and coupling of damage due to porous collapse can all be represented with the RHT model.

$$f(P, \sigma_{eq}, \theta, \varepsilon) = \sigma_{eq} - \gamma_{TXC(P)} * F_{CAP(P)} * R_{3(\theta)} * (F)_{RATE(i)} \quad (5\text{-}1)$$

Where σ_{eq} is the material stress (force/area), $\gamma_{TXC(P)}$ is the fracture surface (Equation 9); $F_{CAP(P)}$ allows you to cap the elastic deviatoric stress under large compressions; R_3 represents the tensile and compressive meridians in the third invariant term (Equation 5-3); and F_{RATE} represents the strain rate enhancement factor (Equation 5-4).

The fracture surface equation reads:

$$\gamma_{TXC} = f'_c \left[A_{Fail}, \left(P^* - P^*_{spall} F_{RATE}\right)^{N_{Fail}}\right] \quad (5\text{-}2)$$

Where fc in the cylinder strength; A_{Fail} and N_{Fail} are user defined parameters; P^* is pressure normalized with respect to f_c; P^*_{Spall} is the normalized hydrodynamic tensile limit and F_{RATE} is a rate dependent enhancement factor (Equation 5-4).

It is possible to truncate the fracture surface, allowing the fracture to fit through a series of experimental points for low pressures and meet back with a standard curve at higher pressures, this process is shown in Figure 5-8.

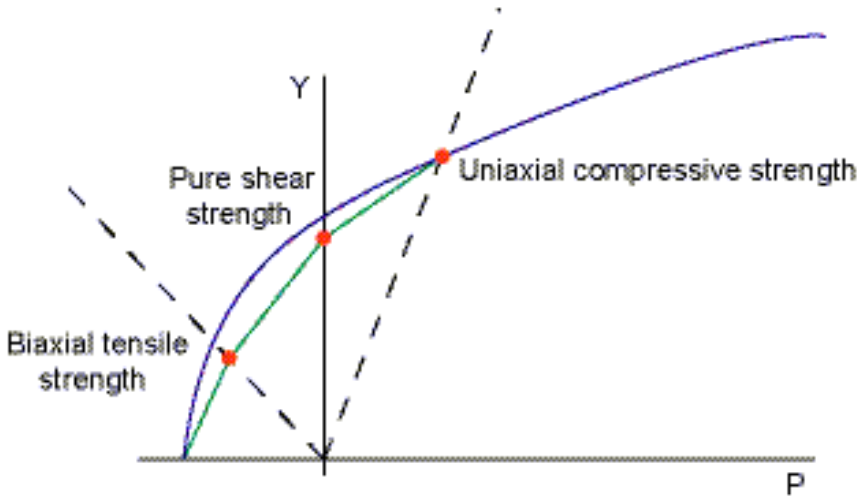

Figure 5-8: Experimental observation of low pressure fracture surface (Ridel et al, 1999)

The third invariant dependence term (R_3) represents a reduction in strength under triaxial extension compared to triaxial compression, through Equation 5-3:

$$R_3 = \frac{2(1-{Q_2}^2)cos\theta+(2Q_2-1)\sqrt{4(1-{Q_2}^2)cos^2\theta-4Q_2}}{4(1-{Q_2}^2)cos^2\theta+(1-2Q_2)^2} \quad (5\text{-}3)$$

Where $(3\theta) = \frac{3\sqrt{3}.J_3}{2^{3/2}\sqrt{J_2}}$;

$Q_2 = Q_{2.0} + BQ.P^*$ for $0.5 < Q_2 < 1$

where $Q_{2.0}$ is an input parameter for a strength ratio at zero pressure; and BQ is the rate the fracture surface transitions from triangular to circular due to pressure increase, usually 0.0105.

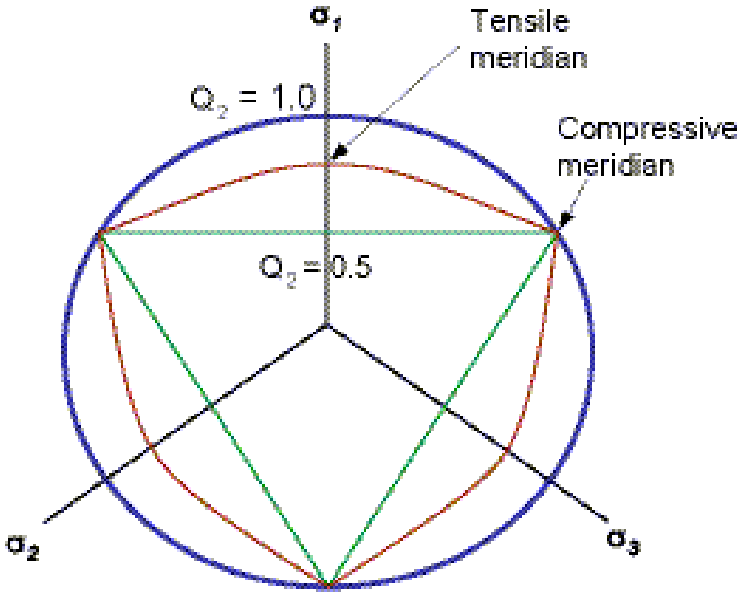

Figure 5-9: The third invariant dependence parameter for RHT strength model. (Ridel et al, 1999)

Strain hardening can be modeled using an elastic surface limit and hardening slope, represented in Figure 5-10.

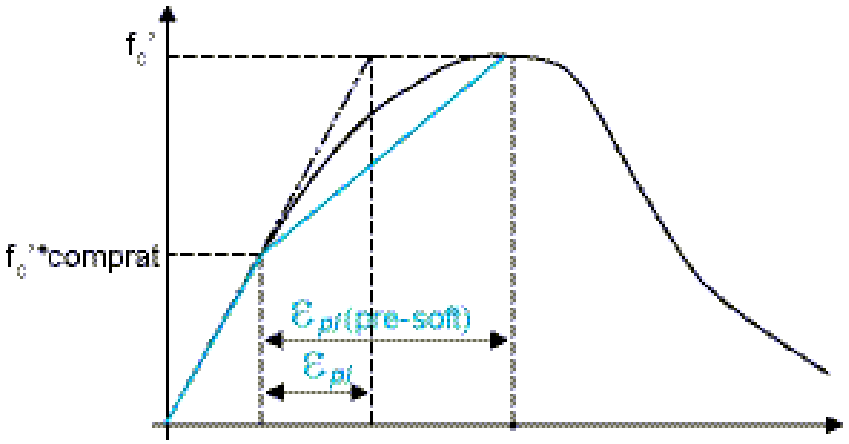

Figure 5-10: Strain hardening function for RHT Model (Ridel et al, 1999)

Damage is a useful output of the RHT model for detonation phenomena. Damage inputs occur in the 'Failure' subsection input. Damage in the model accumulates due to inelastic deviatoric straining using equation 11. Damage accumulation can be for both strain softening and a reduction in shear stiffness.

$$D = \sum \frac{\Delta \varepsilon_{pl}}{{\varepsilon_P}^{failure}} \tag{5-4}$$

Where ${\varepsilon_P}^{failure} = D_1(P^* - {P^*}_{spall})^{D_2}$ and D_1 and D_2 are material constants representing effective strain to fracture with reference to pressure.

F_{RATE}, the strain rate effects for both compression and tension are shown in Equation 5-5.

$$F_{RATE} = \begin{Bmatrix} 1 + \left(\frac{\varepsilon}{\varepsilon_0}\right)^{\alpha} for\ P > {}^1\!/_3\, f_c\ (compression) \\ 1 + \left(\frac{\varepsilon}{\varepsilon_0}\right)^{\delta} for\ P > {}^1\!/_3\, f_t\ (tension) \end{Bmatrix} \tag{5-5}$$

Where $\varepsilon_{0,}$ is the initial strain rate; f_c is the compressive strength and f_t is tensile strength.

An overall representation of the elastic, fracture and residual failure surfaces can be seen in

Figure 5-11.

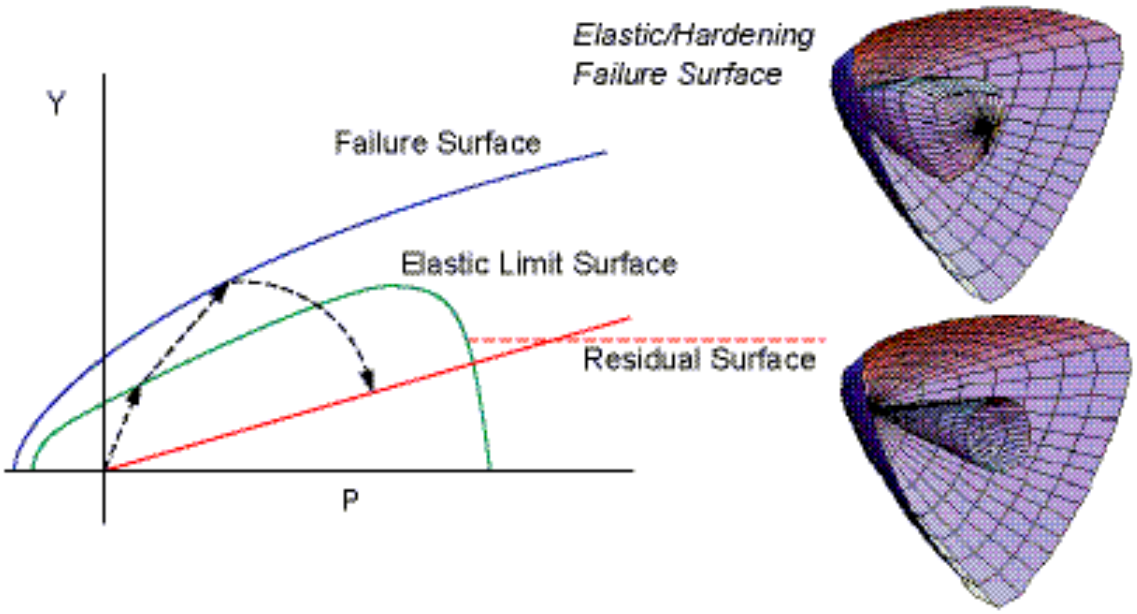

Figure 5-11: Failure, elastic and residual surfaces in the RHT concrete model (Riedel et al, 1999)

Table 5-2 shows the input variables for the RHT material strength model with the final values input into Explicit Dynamics. Density and compressive strength values were taken from the tests described in Section 5.1: Concrete Block Material Properties. The minimum strain to failure was set to 0.02, a number of values were tested, ranging from 0.001 to 0.1. Erosion was either too minimal or too excessive, shown in Figure 5-12 and Figure 5-13, no correlation to the experiments in Chapter 4 were present in either case. The rate was reduced to 0.02, this was found to be a good erosion rate for concrete exposed to high explosive pressures (Lusk et al, 2008) and more representative of the experiments carried out. All other values were taken from the material library available in Explicit Dynamics.

Table 5-2: Input Variables for RHT Strength Model

Name	Symbol	Value	Units
Density	ρ	148.6	Density (lb/ft3)
Compressive Strength	fc	10,000	Stress (psi)
Tensile Strength	ft/fc	0.1	None
Shear Strength	fs/fc	0.18	None
Intact failure surface constant A	A_{FAIL}	1.6	None
Intact failure surface exponent N	N_{FAIL}	0.61	None
Tens./Comp. Meridian ratio	$Q_{2.0}$	0.6805	None
Brittle to Ductile Transition	BQ	0.0105	None
Hardening Slope		2.0	None
Elastic Strength/ft		0.7	None
Elastic Strength/fc		0.53	None
Fracture Strength Constant	B	1.6	None
Fracture Strength Exponent	m	0.61	None
Compressive strain rate exponent	α	0.032	None
Tensile strain rate exponent	δ	0.36	None
Maximum fracture strength ratio	SFMAX	1e+20	None
Use cap on elastic surface		YES	None
Damage constant D1	D1	0.04	None
Damage constant D2	D2	1.0	None
Minimum strain to failure		0.02	None
Residual Shear modulus fraction		0.13	None

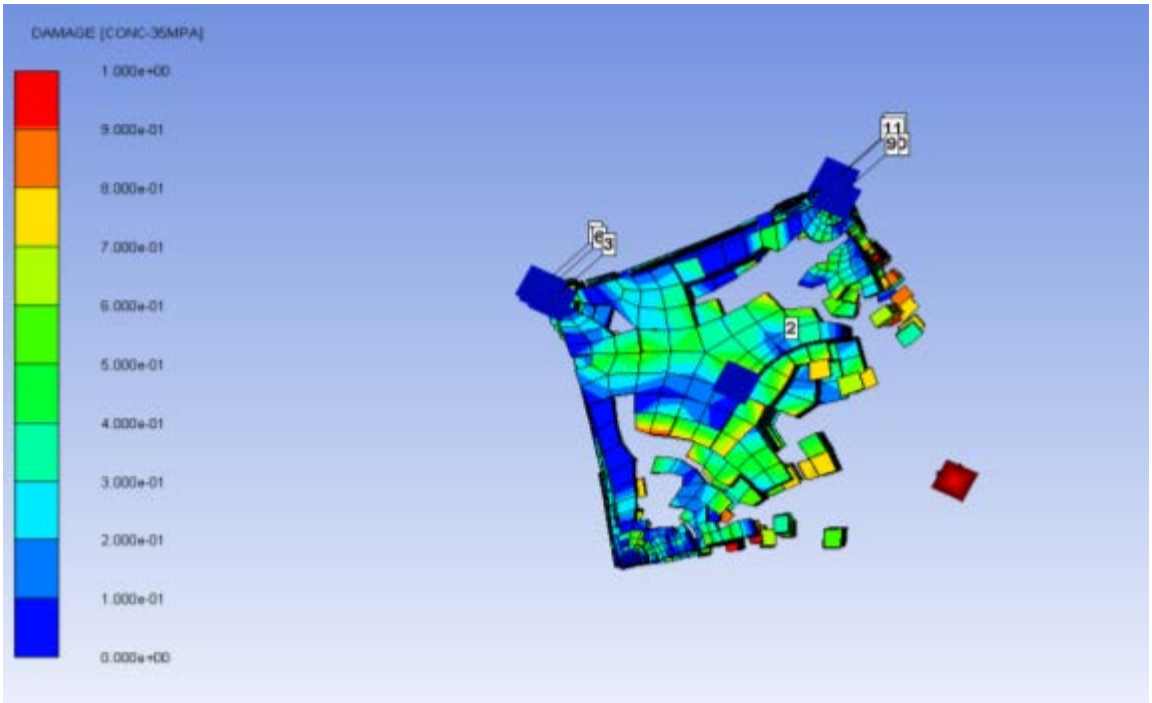

Figure 5-12: Excessive erosion with strain rate of 0.001

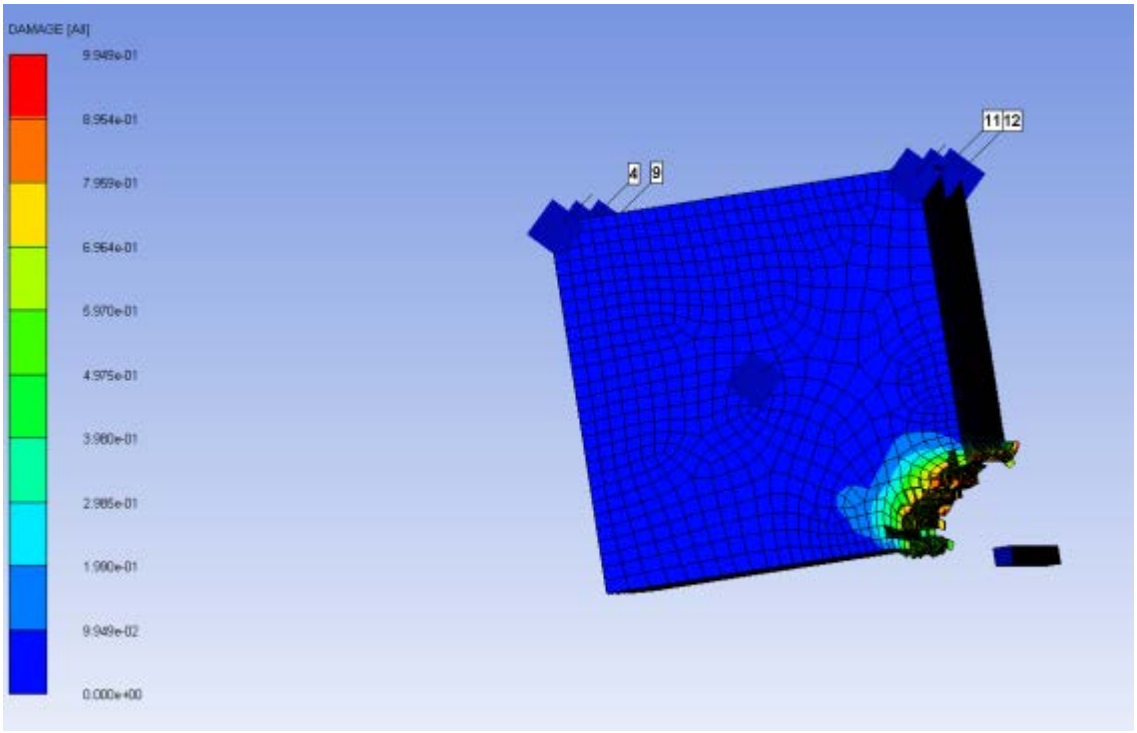

Figure 5-13: Minimal erosion with stain rate of 0.1

5.3.2 P-alpha Equation of State Model

The p-alpha equation of state model is the most widely used material model for shock compaction since it has good results at both low and excessing stress levels (Herman (1960). It is assumed in the model that the internal energy is the same for a porous material as it is for a solid material with the same pressure and temperature conditions. Material behavior is elastic up to a defined point P_e (Figure 5-17), beyond this, plastic behavior takes the material to complete compaction at P_s. Equation 5-6 describes the relationship between these parameters and the values are shown in Table 5-3fo194.

$$\alpha = 1 + (\alpha_p - 1)\left[\frac{\rho_1 - \rho}{\rho_s - \rho_e}\right]^2 \qquad (5\text{-}6)$$

Where αp is the initial compaction pressure, ρ_e is the initial compaction pressure, and ρ_s is the solid compaction pressure.

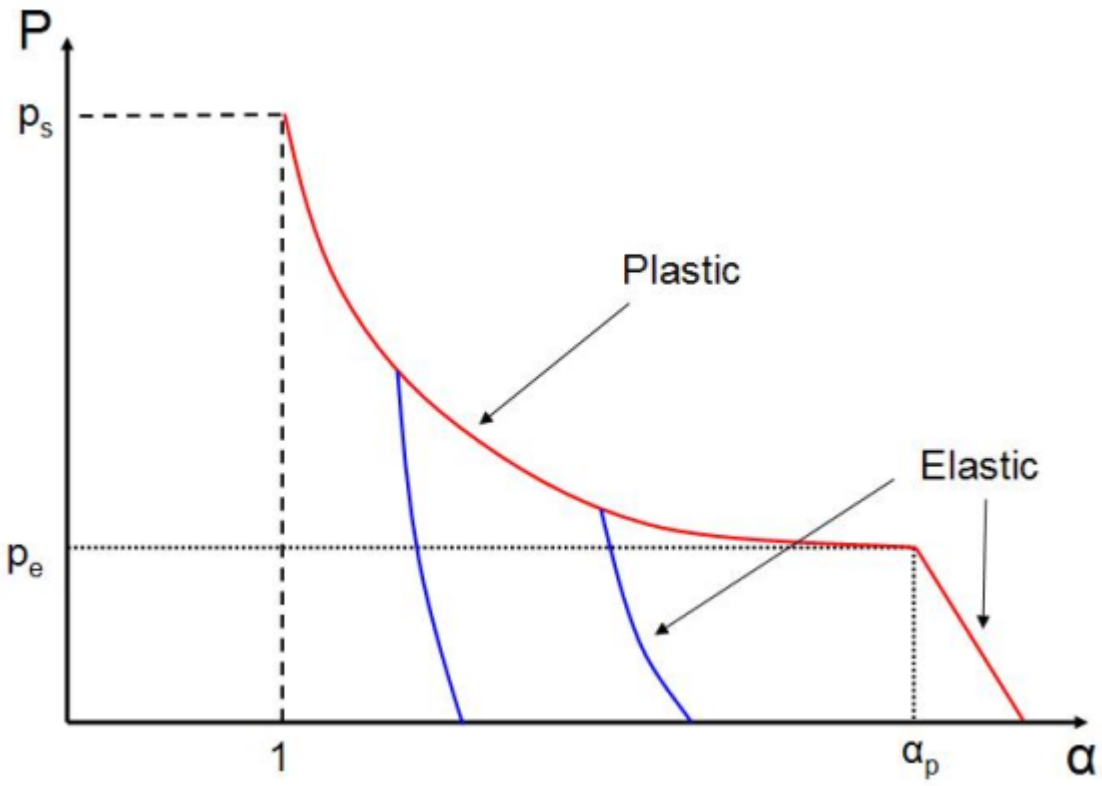

Figure 5-14: P-Alpha EOS (After Herman 1960)

Table 5-3: Input parameters for the P-alpha EOS

Name	Symbol	Value	Units
Solid Density	ρ_{solid}	120	Density
Porous Soundspeed		2.92e+3	Velocity
Initial Compaction Pressure	P_e	2.33e+4	Stress
Solid Compaction Pressure	P_s	6.0e+6	Stress
Compaction Exponent	n	3.0	None

The output results variables associated with the RHT concrete strength model and the P-alpha EOS relevant to fragmentation correlation are Damage, Pressure and Stress. Damage is a unit less scale from 0 to 1 where 0 is unaffected material and 1 is completely rubblized. It is deemed that anything above 0.7 is suitable fragmentation for a mining operation (Preece and Lownds, 2008). Stress and pressure in this instance are output in psi.

5.3.3 JWL Equation of State

Jones, Wilkins and Lee proposed the JWL EOS describing detonation pressure expansion for high energy explosive materials. Values for common explosives, including that of PETN have been found experimentally and are already input into Autodyn. The relationship between pressure and density can be found from Equation 5-7 and Figure 5-15. (Dobratz and Crawford, 1985)

$$\rho = A(1 - \frac{\omega\eta}{R_1})e^{-\frac{R_1}{\eta}} + B(1 - \frac{\omega\eta}{R_2})e^{-\frac{R_2}{\eta}} + \omega\rho e \qquad (5\text{-}7)$$

Where ρ_0 is the reference density, $\eta = \rho/\rho_0$ and A, B, R_1, R2 and ω are constants found experimentally.

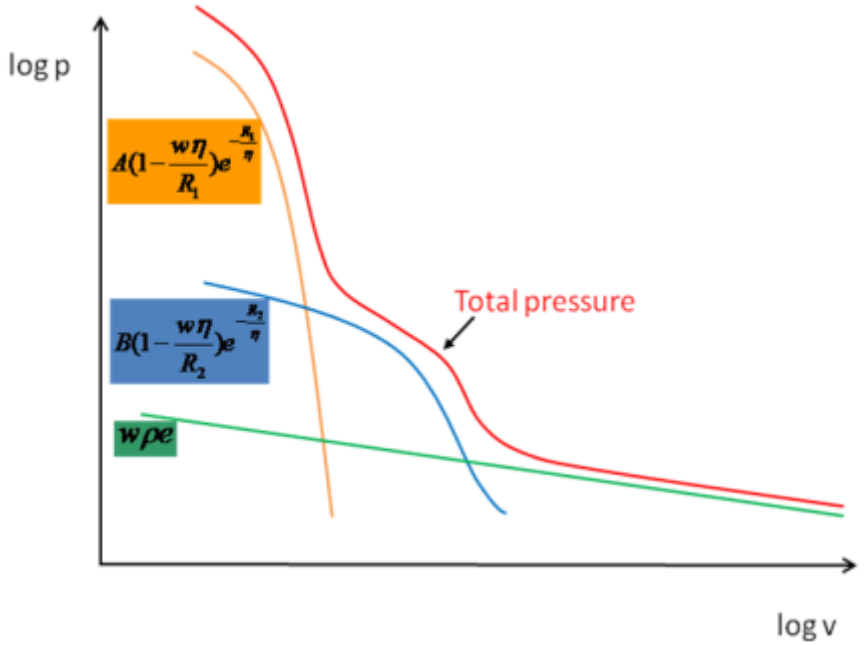

Figure 5-15: Pressure and density relationship for the JWL EOS (ANSYS, 2014)

Input parameters, as well as the values obtained from ANSYS Autodyn for 1.77 g/cc density PETN are shown in Table 5-4

Table 5-4: Input parameters for 1.77 PETN (ANSYS, 2014)

Name	Symbol	Value	Units
Parameter A	A	6.1705e+8 psi	Stress
Parameter B	B	1.6926e+7 psi	Stress
Parameter R1	R1	4.4	None
Parameter R2	R2	1.2	None
Parameter ω	ω	0.25	None
C-J Detonation Velocity	D_{CJ}	8.3e+3 ft/s	Velocity
C-J Energy/unit mass		1.01e+7 lb/in^2	Energy/mass
C-J Pressure	P_{CJ}	3035e+7 psi	Stress

5.4 Geometry

The geometry for the models is relatively simple. A geometry modeler is available in Explicit Dynamics making complex geometries relatively simple to execute. The block, with dimensions shown in Figure 5-16, was input through the geometry modeler. It has already been established that Explicit Dynamics is only suitable for modelling Lagrangian parts; therefore the explosive column was modelled in Autodyn as a Eulerian part. Figure 5-17 demonstrates the two solvers linked in ANSYS Workbench, any input from Explicit Dynamics transfers into the Autodyn model. The reverse action is not possible.

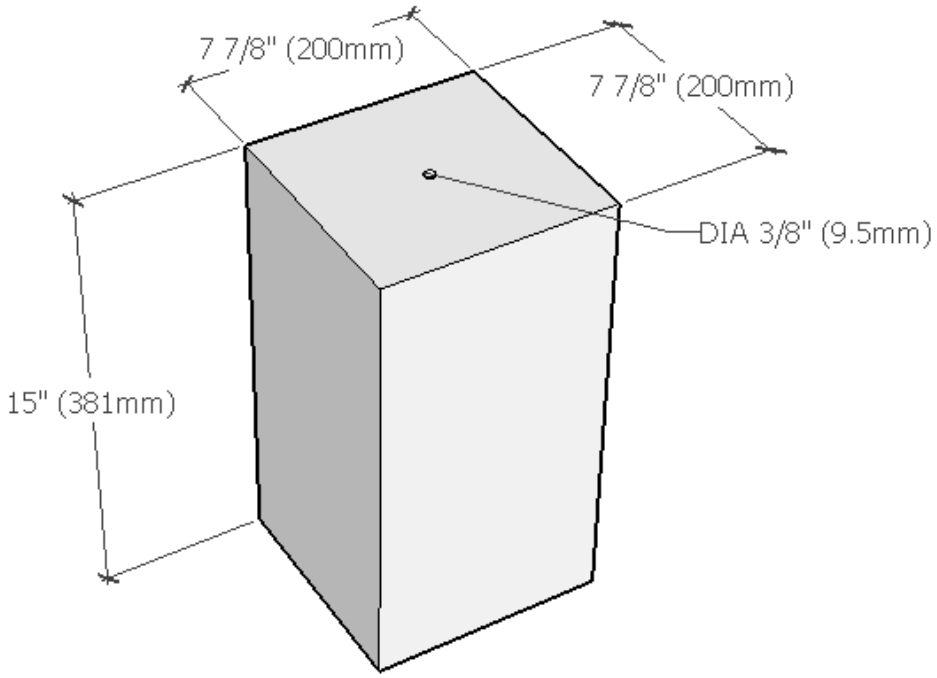

Figure 5-16: Block dimensions

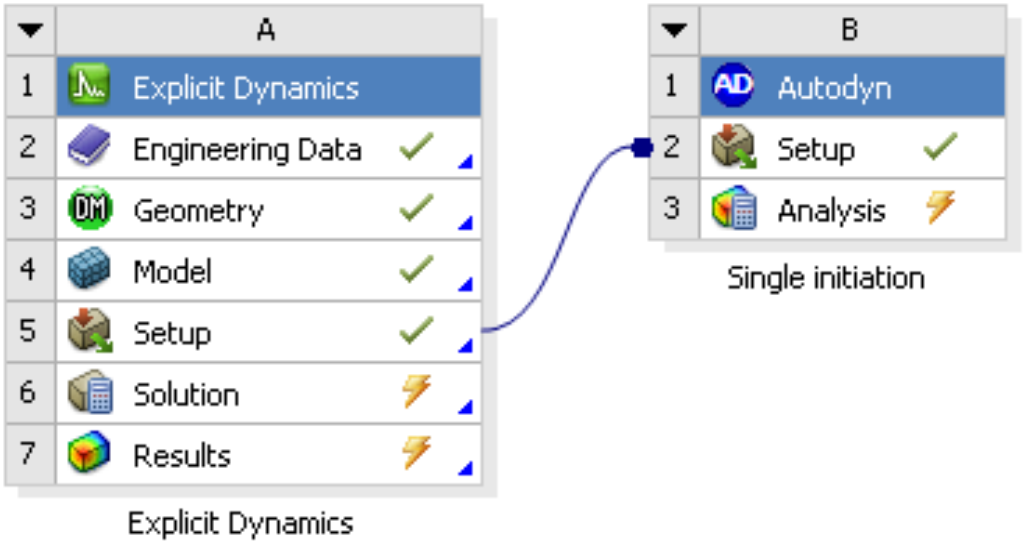

Figure 5-17: Explicit Dynamics and Autodyn systems joined in ANSYS Workbench

Since the block is uniform in character and the explosive column drilled directly through the middle of the block, the use of symmetry planes allow the simulation time to decrease significantly due to the reduction in grid cell numbers. Two symmetry planes were added to the ZX and YZ Planes. The explosive, coupled with the masonry block, is shown in Figure 5-18. The radius of the explosive was set to 3/8 in (4.7625 mm), the same as that of the drilled hole in the experiments in Chapter 4.

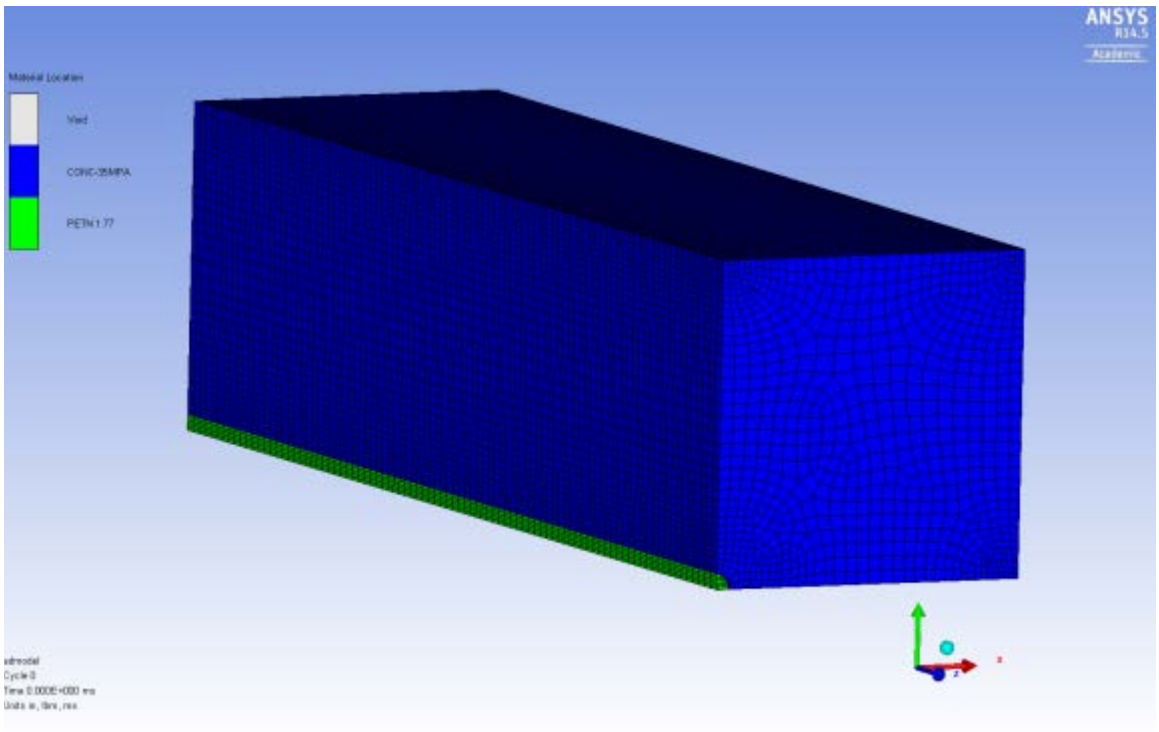

Figure 5-18: Explosive and block geometry in Autodyn

5.5 Mesh Size

The solver, or mesh type, is already known, but the number of grid cells has to be determined. A number of iterations were made to the number and distribution of cells in the grid for the Lagrangian block. Since the solver calculates shape change per cell, clearly a more accurate model overall will be the one with the smallest grid size, or largest number of cells. Computational time however increases significantly as cell size decreases so a balance is made. The final model contained 144,000 cells, 40 cells along each 3.9 in quarter side and 90 along the 15 inch length. The explosive column also had 90 cells along its length and 5 cells along the radius of the cylinder. Mesh refinement was applied to the corners of the block and around the detonation column. Cell erosion around the detonation column will be significant, since that is where the highest pressures occur. Large cells here will create a larger volume of eroded material, not representative of the experimental tests. Time to run the models for 2 ms of detonation time was approximately 15 hours. Early models were executed to 6 ms but the additional computational time to run, coupled with the minimal difference in Damage and Pressure

contours throughout the block between 2 and 6 ms, deemed the additional time unnecessary.

5.6 Gauge Points

Gauge points can be input into specific cells throughout the modelled geometry. This allows pressure and stress output at individual points throughout the material to be compared. A total of 33 gauge points were used, along the length of the block and radially out to the corners from the center explosive column. The locations of the points are shown in Figure 5-19. Table 5-5 shows the exact grid and material location of the gauges. The selected points allow collision of stress waves through the center of the block to be compared to each other, and to the outer edges of the same block. Gauge points extending through the block will show the compressive and tensile stress dissipation through the block whilst the gauge points running along the length of the block will demonstrate the pressure exerted on the block from the explosive, and whether this increases at the point of wave interaction. Applying gauge points experimentally is not practical since the high pressures would simply destroy the sensors. Using a model to examine the pressure and stress change through the block is something not possible at these small distances experimentally.

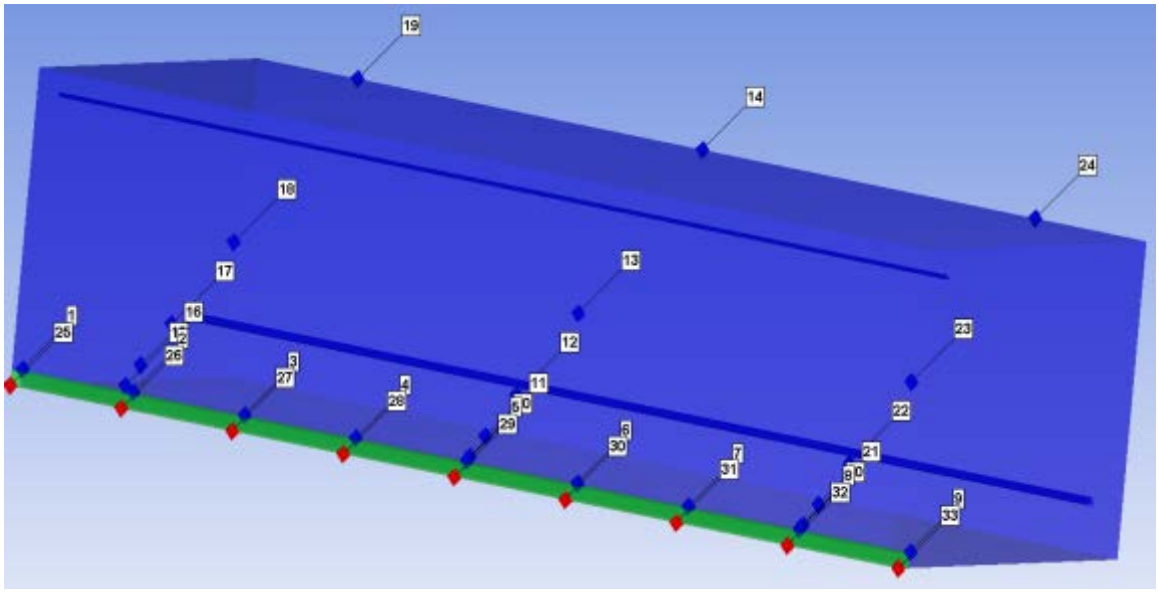

Figure 5-19: Gauge point locations

Table 5-5: Gauge Point Locations

Coordinate				
X (in)	Y (in)	Z (in)	Location	
0.20	0.20	0.00	Block	Borehole Wall
0.20	0.20	1.88	Block	Borehole Wall
0.20	0.20	3.75	Block	Borehole Wall
0.20	0.20	5.63	Block	Borehole Wall
0.20	0.20	7.50	Block	Borehole Wall
0.20	0.20	9.38	Block	Borehole Wall
0.20	0.20	11.25	Block	Borehole Wall
0.20	0.20	13.13	Block	Borehole Wall
0.20	0.20	15.00	Block	Borehole Wall
0.25	0.25	7.50	Block	Radial through block - Center
0.49	0.49	7.50	Block	Radial through block - Center
0.98	0.98	7.50	Block	Radial through block - Center
1.97	1.97	7.50	Block	Radial through block - Center
3.94	3.94	7.50	Block	Radial through block - Center
0.25	0.25	1.88	Block	Radial through block - Left
0.49	0.49	1.88	Block	Radial through block - Left
0.98	0.98	1.88	Block	Radial through block - Left
1.97	1.97	1.88	Block	Radial through block - Left
3.94	3.94	1.88	Block	Radial through block - Left
0.25	0.25	13.13	Block	Radial through block - Right
0.49	0.49	13.13	Block	Radial through block - Right
0.98	0.98	13.13	Block	Radial through block - Right
1.97	1.97	13.13	Block	Radial through block - Right
3.94	3.94	13.13	Block	Radial through block - Right
0.00	0.00	0.00	Explosive	Middle of cylindrical column
0.00	0.00	1.88	Explosive	Middle of cylindrical column
0.00	0.00	3.75	Explosive	Middle of cylindrical column
0.00	0.00	5.63	Explosive	Middle of cylindrical column
0.00	0.00	7.50	Explosive	Middle of cylindrical column
0.00	0.00	9.38	Explosive	Middle of cylindrical column
0.00	0.00	11.25	Explosive	Middle of cylindrical column
0.00	0.00	13.13	Explosive	Middle of cylindrical column
0.00	0.00	15.00	Explosive	Middle of cylindrical column

5.7 Conclusion

Three model simulations can be executed utilizing accurate input data from rock strength tests and ANSYS embedded material models. Through the use of symmetry planes, the computational time is significantly reduced to have allowed for multiple iterations of grid size, and distribution. Significant data will come from the model simulations from both the stress and pressure data at specific locations in the blocks, and visual contours of these two variables as well as an RHT specific output of Damage. All results are explained in Chapter 6.

Chapter 6. Model Simulation of Colliding Detonation ad Shock Waves

6.1 Introduction

Three separate model simulations were computed to a time of 2 ms. Single initiation (Test 1), colliding detonation waves (Test 2) and colliding shock waves (Test 3) to the specifications described in Chapter 5. Detonation time for single initiation, the longest length of detonation cord, was in under 0.04 ms, providing 50 times this time length in run time until completion of the simulation. Computation time for the models was approximately 10 hours to complete. Three parameters were used for analysis, pressure, stress and damage. Damage is a useful tool to compare directly with the experimental tests for validity. Pressure and Stress contours cannot be calculated experimentally due to the high heat and pressure exerted from the explosive, subsequently destroying expensive sensors in their wake. Visual contour patterns throughout the full block, focusing in particular on the collision regions, as well as pressure and stress values throughout the blocks are analyzed throughout Chapter 6.

In reality, there was a small air gap between the explosive and the block. When modelled in this manner, error messages were endless due to the more complex interaction between the parts; and the time per cycle increased due to the additional Euler part. A decision was made to eliminate this air gap. Since ANSYS can only model either Lagrangian grids or Eulerian grids, not both intertwined, the gas pressure phase of the fragmentation process cannot be modelled effectively throughout the Lagrangian block. Previous research involving air coupling has either been in 2D (Zhu et al, 2008) or through the use of extensive wedge calculations calculating the explosive pressure travelling through the air (Schronberg et al, 2008 and Lusk et al, 2008) and only the stress wave part of the fragmentation process discussed. For this reason, only the effects of the detonation pressure and resultant stress on the surrounding medium are modelled. A completely coupled explosive will assert a higher pressure on the blast hole wall than a decoupled one, nevertheless the interest from the model are the distribution of higher stress levels and pressures throughout the block, not exact detonation pressures at the blast hole wall.

6.2 Results and Analysis

The results and analysis section is split into three subsections, Pressure, Stress and Damage. Results for Tests 1, 2 and 3 are discussed and comparisons made throughout this Chapter.

6.2.1 Pressure

The theory of shock pressure from detonation has been explained extensively in Chapter 3. Cooper (1996) stated that when two approaching shock waves collide, a pressure greater than double that of the original detonation pressure will be present at the point of collision. Additionally, Cooper (1996) stated that upon collision, the wave will reflect back in the opposing direction. Rossmanith (2003) published Lagrange diagrams with areas of increased fragmentation zones where P and S waves overlap with no experimental or simulated results. Johannsson and Ouchterlony (2013) published concern for Rossmanith's oversimplification of the problem in hand, experimental results published showed no increase in fragmentation at times were a shock collision between adjacent holes would exist. As already discussed in Chapter 4, shock collision has been carried out experimentally and simulated in a single hole. Before additional parameters can be incorporated, it has to be first established what happens in the simplest shock collision: head on collision with no initial fractures in which to contend.

A collision of detonation waves can only occur in the detonation column, as soon as that pressure reaches the borehole wall, a compressive shock pressure is exerted on the rock mass. This dissertation has described Test 2 as a collision of detonation waves. Although this collision is also occurring, it is how this additional detonation pressure where they collide affects the surrounding strata as the compressive shock pressure travels through block that is of interest. This concept of shock collision becomes more apparent throughout this Chapter where shock collision is discussed in both Test 2 and Test 3.

6.2.1.1 Tests 1 and 2

Screen shots of Tests 1 and 2 at varying times through the model simulation are shown in Figure 6-2. The portion of the blocks represented is exactly half, with a symmetry applied through the y-plane straight through the explosives column. Times each screen shot was taken in ms, are 0.015, 0.025, 0.035, 0.045 and 0.1. The times selected allow for the shock collision in Test 2, the full detonation of the detonation column in Test 1 as well as a representation of the depleting pressure after full detonation of the explosive column to be visualized. Detonation for Test 1 is from the bottom of the explosive column. Top and Bottom initiation is utilized in Test 2, both at a time of 0 ms. Contours displayed are Pressure in psi, ranging from a compressive pressure of 10000 psi in red to a tensile pressure of -1000 psi shown in blue. This gives the full range to failure at both the compressive and tensile strength of the blocks tested experimentally. The key for pressure is shown in Figure 6-1 in scientific units.

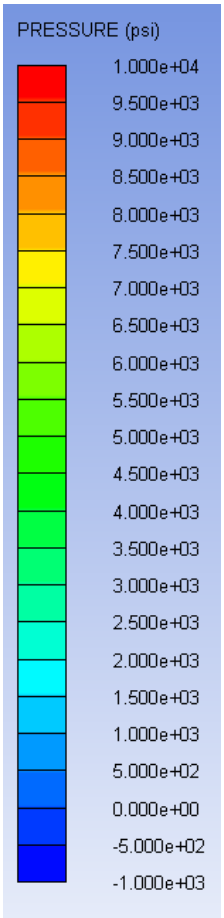

Figure 6-1: Color key for pressure in psi

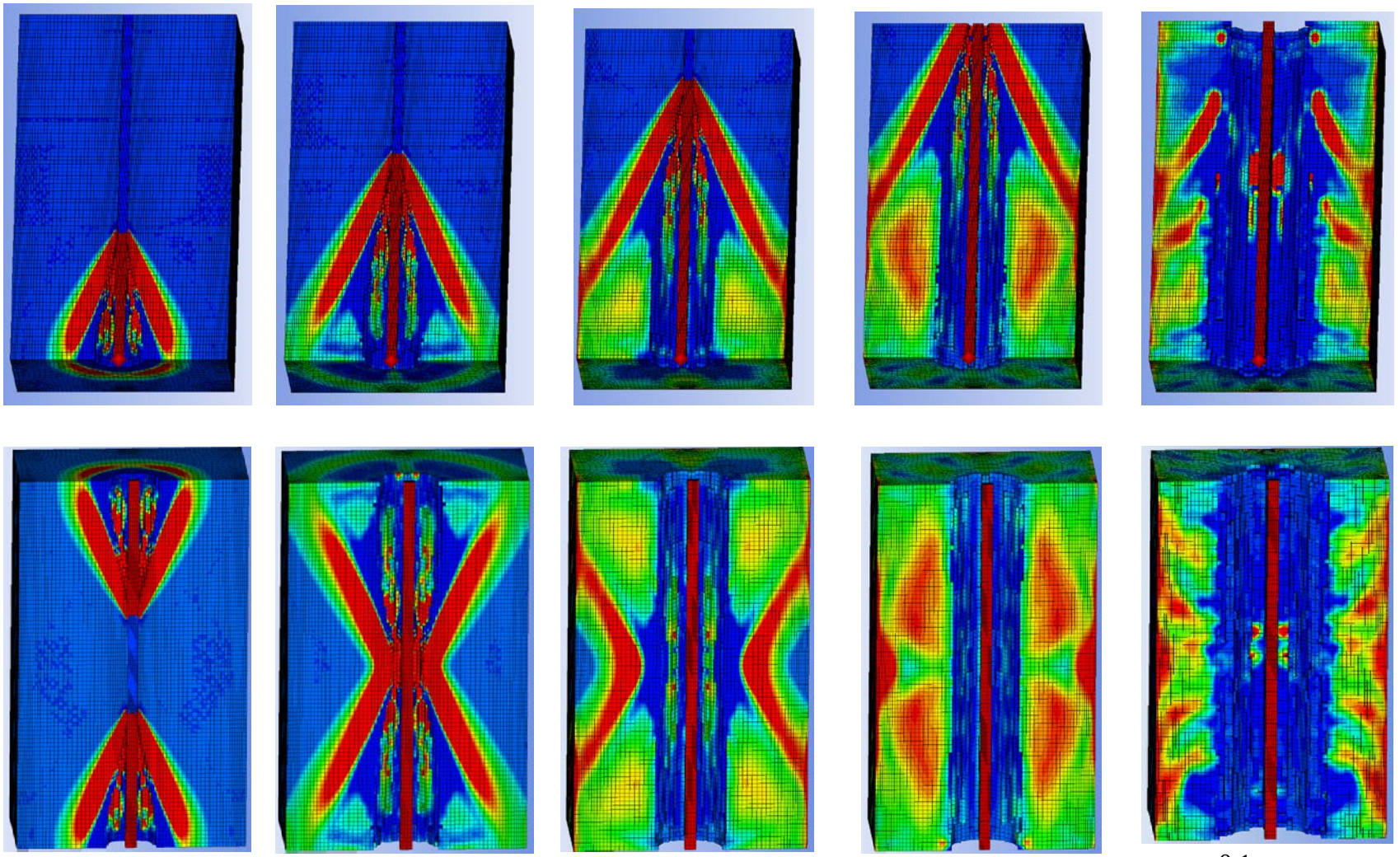

Figure 6-2: Sequence of model simulation for Test 1 (Top) and Test 2 (Bottom)

Test 1 shows a constant shock front travelling through the block. In front of the detonation, particle velocity, internal energy and pressure are at rest. As the shock front passes through, a sudden increase of all these parameters occurs. Only pressure is shown here, but the sudden increase in pressure is shown by the conical wave in red. The pressure, of at least 10,000 psi, exceeds the compressive strength of the material. This high compressive strength has eroded material through the center of the block immediately surrounding the blast hole. With increasing distance from the blast hole, pressure decreases as the wave turns from deep red to green and dropping below the failure point of the material. At some point all parts of the block have a red, high pressure, wave front that exceeds the strength of the block. Erosion has not occurred here due to the short duration that the high pressure is applied. Behind the compressive front is an area of tensile pressure, as expected from the theory. At a time of 0.015 ms in both Test 1 and Test 2 wave fronts are identical, simply with an additional wave from the top of Test 2, giving confidence in the model and constant inputs between the two models.

As the two shock fronts meet in Test 2, no evidence of a reflection is apparent, instead this pressure travels out towards the free face, after which a reflection from the free face of higher pressure can be seen at 0.1 ms. Rossmanith's hypothesis (2003) had reference to the reflecting tensile wave, not compressive. This reflection is not visible either. One explanation for the lack of reflection is due to the Lagrange grid that is modeled. Behind the shock front it has been established that the particle velocity, internal energy and pressure instantly turned from an unshocked state to a shocked one. With this, the Lagrangian state also changes to Eulerian. This final change cannot be displayed using ANSYS, or any other computer simulated finite element modelling program suitable for such high dynamic pressures. Since the Eulerian process is not simulated, any potential reflected pressure will have to reenter the shocked front where particle velocities will be excessive.

An attempt was made to model the blocks in an Euler grid, containing no Lagrangian parts at all. There is no Euler/Euler interaction input process, only Euler/Lagrange and Lagrange/Lagrange so the detonation pressure did not propagate outside of the explosive column as the program could not detect that the two grids were related. It cannot be said

from this simulation that no reflection is possible, but a valid explanation supporting this has been found and identified a major problem with simulating blasting processes in this way. The sudden change in direction of the shock fronts could however be the reason for the directional throw observed experimentally from the center of the block in Section 4.3.1.3: High speed video Analysis.

Figure 6-3 shows the top of the full block for Test 1 and Test 2 after 1 ms. The blue tensile areas extend radially from the center where the explosive is present to the extents of the block, most prominently to the corners of the block. This correlates well with theory and experiments, displayed again in Figure 6-4. If the gas pressure could be modelled it is expected that the eroded cells would follow these areas under high tensile pressure. The volume of eroded material in Figure 6-3 is greater than that present experimentally in Figure 6-4. This is due to both the difference between a coupled and decoupled explosive and the harsh inputs of erosion of a cell when strength failure limits are met in the model. If cell size was smaller, a smaller volume of eroded cells would be present as it is the overall pressure in the entire cell that contributes to failure, but the computational cost far exceeded the benefits of accurate compressional erosion of cells. Tensile strength of a material is the important factor, and this is simulated well here. What can also be seen is the additional erosion of cells in Test 2 compared with that of Test 1 as well as larger tensile regions, further supporting the potential for increased tensile fragmentation when two shock fronts collide

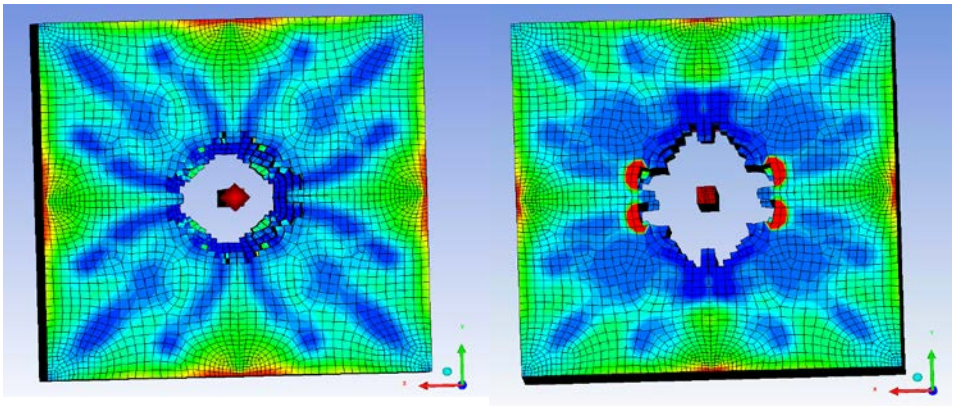

Figure 6-3: Top of Block for Test 1 (Left) and Test 2 (Right)

Figure 6-4: Top of block from experimental tests

Gauge points were inserted throughout the blocks and explained in Table 5-5. Pressure at each gauge point was recorded. Detonation pressure within the blast hole is of importance in a full scale mining blast to gather complete the combustion of the non-ideal explosives used, poor detonation will produce both poor fragmentation to that designed for and unwanted secondary environmental effects. Gauge point locations were included within the blast column but results are of little significance. The main point of interest is the shock wave travelling through the block. Despite this, Figure 6-6 and Figure 6-7 demonstrate the results for Tests 1 and 2 respectively. Test 1 displays a drop in pressure at gauge 28 and 29 towards the center of the block. Values for each gauge point is dependent on the exact location of the point within the cell it is contained. The only explanation for this is that the points for these cells were close to a cell boundary and calculation altered. Erosion of cells does not occur in the Euler explosives column which takes into consideration the pressure in the entire cell and upon erosion the pressure travels to the next cell. For Euler, the pressure can vary within the cell and the gauge point location of greater influence. Test 2 shows an increase in pressure where the two detonation waves have collided, the increase is only 25% greater than the constant pressure of $1.7*10^7$ psi. This increase is significant, but not greater than double the initial pressure as explained by Cooper (1996). Gauge 25 did not produce data in either test but it is expected to resemble gauge 33 for Test 2.

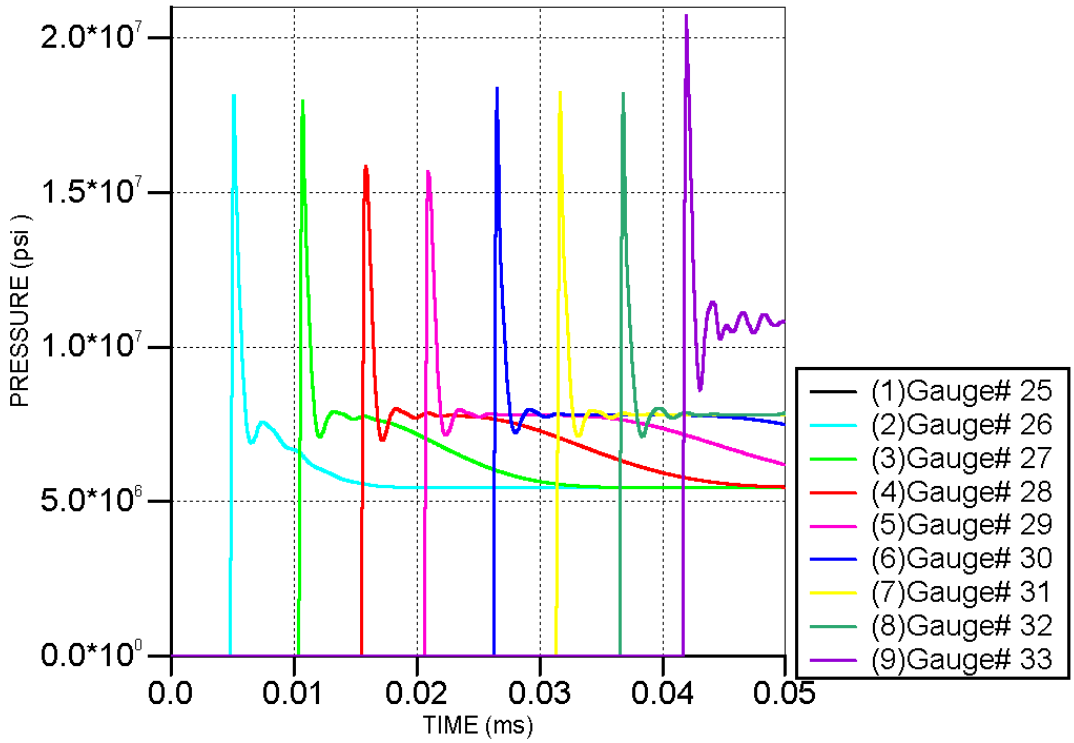

Figure 6-5: Pressure – Time Plot for the detonation column. Test 1

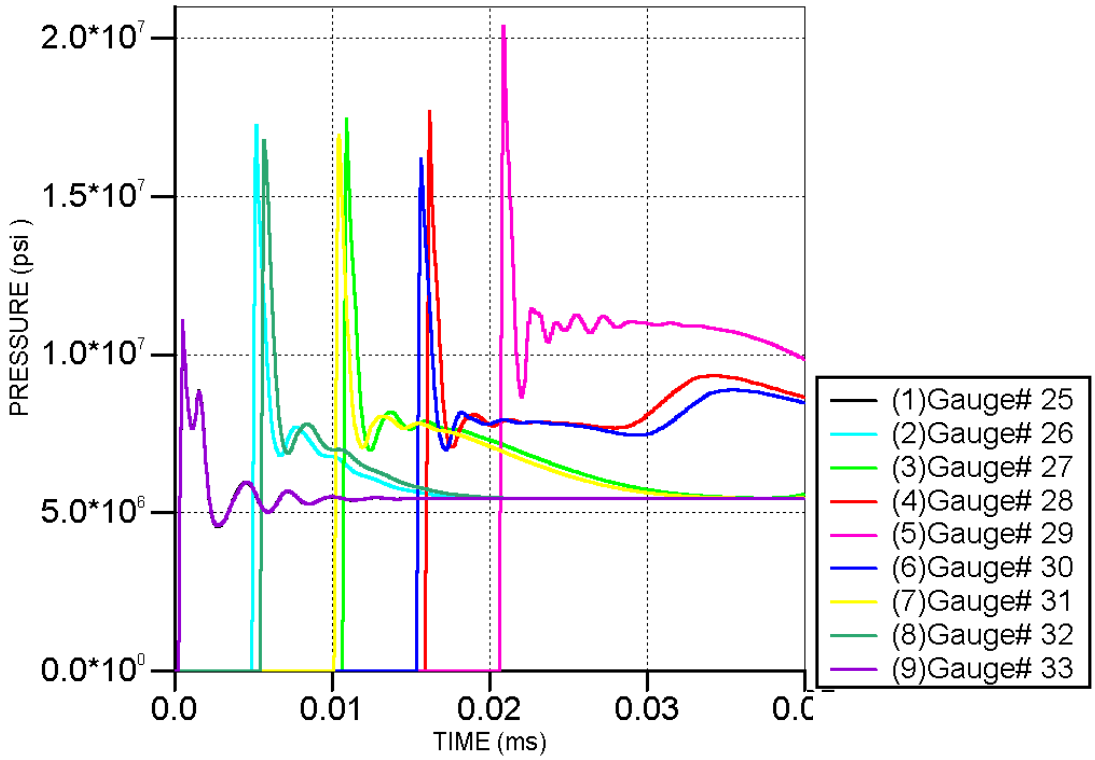

Figure 6-6: Pressure - Time plot for the detonation column. Test 2

Figure 6-7 shows a graph of peak pressure (psi) against distance (in) along the borehole wall. Distance is taken from the bottom of the blast hole for gauge points 1 through 9 for both Test 1 and Test 2. A lower pressure is present at the point of detonation as the full diameter of explosive has not yet fully initiated and cannot exert the same detonation pressure on the blast hole wall. Beyond this, a constant pressure is observed around $5.5*10^6$ psi, well above the compressive strength of the block of $1*10^4$for Test 1. The detonation pressure for PETN in the LLNL Explosives Handbook (1985) is $4.9*10^6$ psi. Test 2, shown in orange, has an increase in pressure at the center of the block, 7.5 inches from each detonation point. At this point, the highest pressure exerted on the rock mass is present; the pressure again is not more than double that of the original pressure as suggested by Cooper (1996). An increase is still observed through the center of the block and this observation continues in Figure 6-8. The bar chart shows increasing distance radially away from the center blast hole at the top, center and bottom of the column. The compressive strength remains above 10000psi until 0.49 inches from the centerline, all cells until this point are eroded, shown in Figure 6-2. Through these three closest gauge points, the pressure in the center for Test 2 is higher than any other location in the block demonstrating that this increase does influence the full width of the block in question, rather than reflecting back directly at that point.

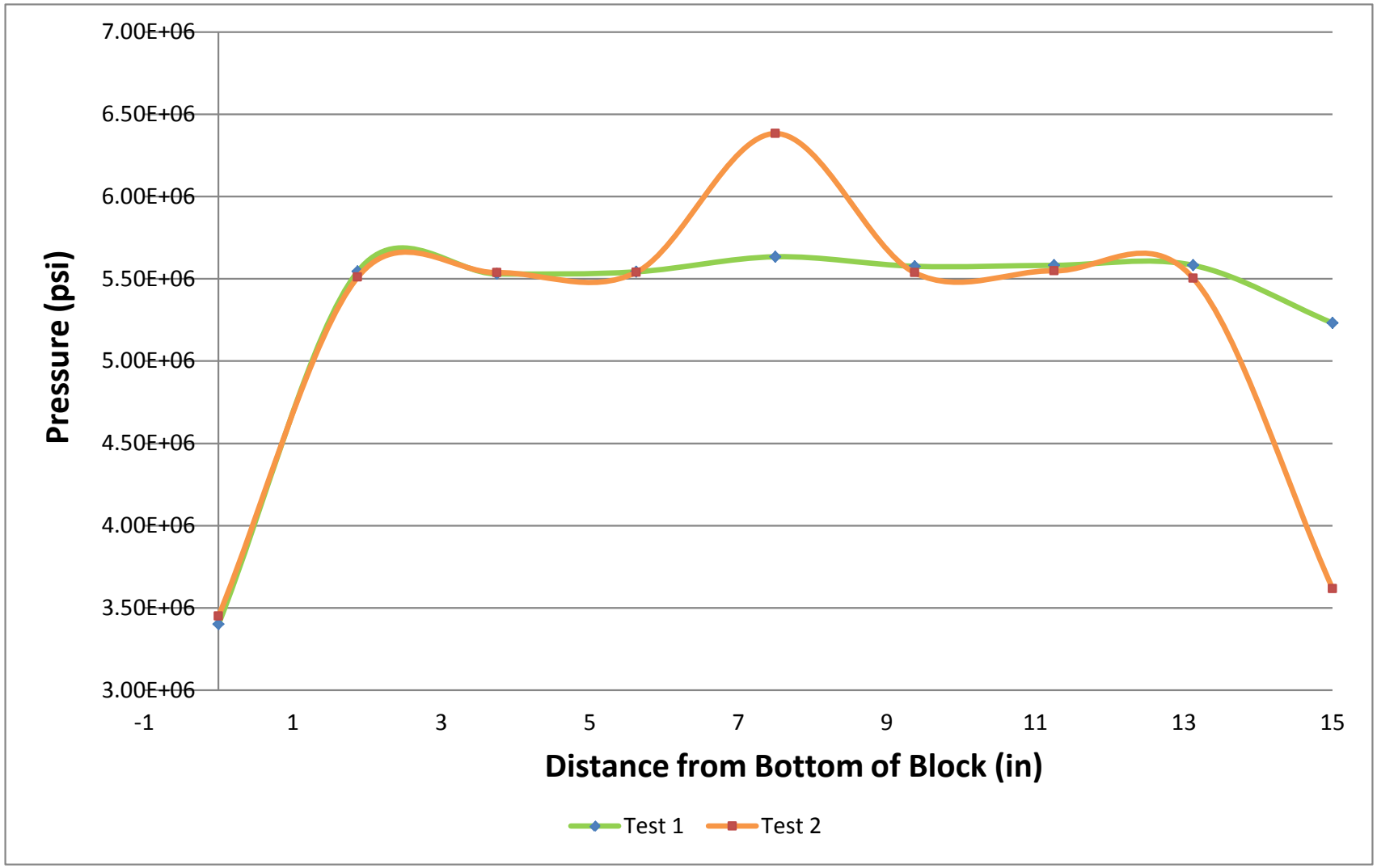

Figure 6-7: Pressure distance plot for test 1 and 2 along the blast hole wall

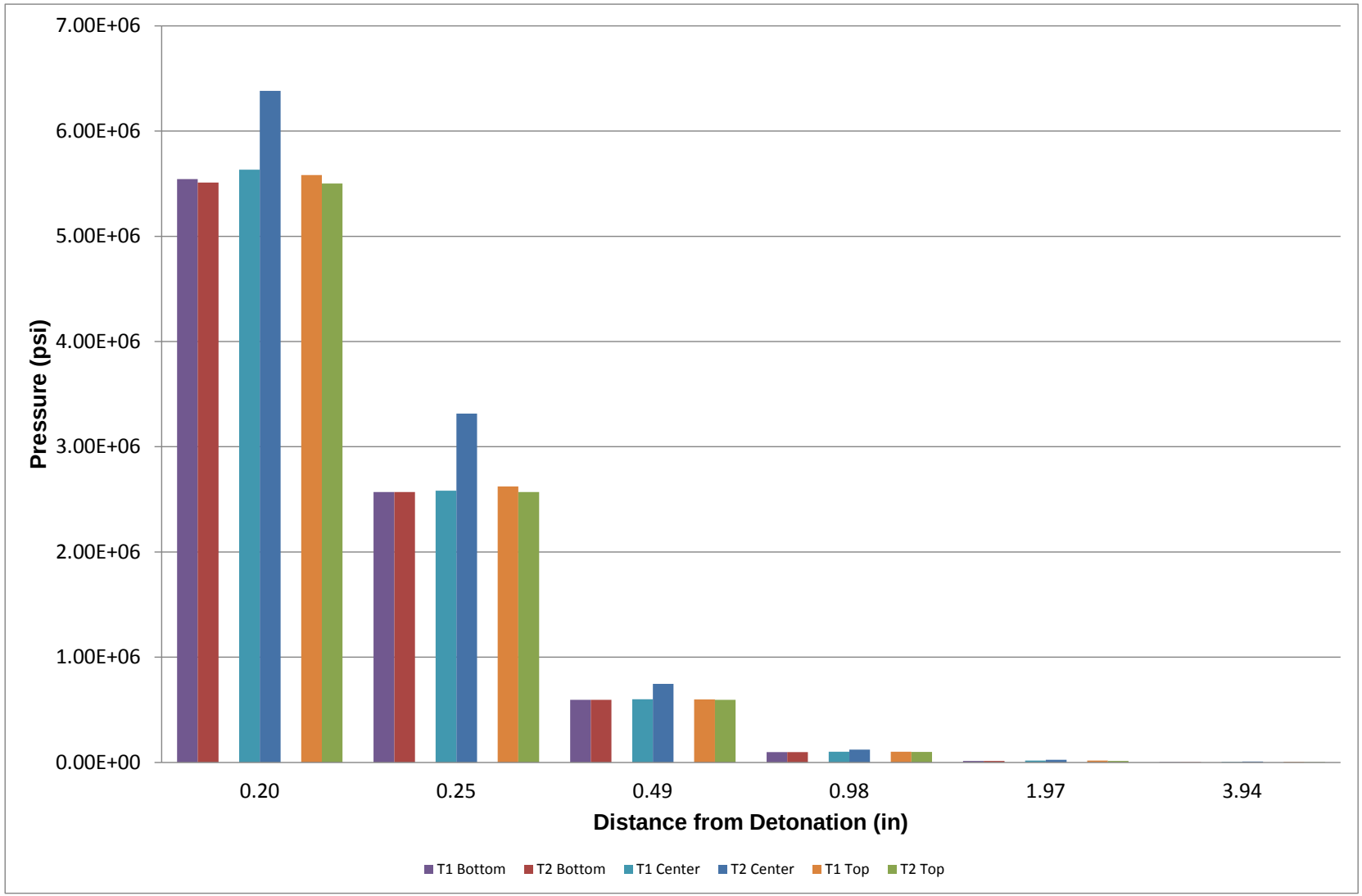

Figure 6-8: Bar graph of pressure and distance from detonation. Test 1 and 2

Figure 6-9 shows a screen shot of the pressure time graph produced in ANSYS for gauge points of increasing distance from the blast hole for Test 1. The three sets of shock waves are identical, just located at different points on the block and therefore recording at different times. Pressure peaks closest to the blast hole show a rapid increase in pressure and fail almost instantly. This sharp rise coincides with Cooper's theory that when a shock front passes through, the material instantly changes from an unshocked state to a shocked one. It can be said that the first two gauge points demonstrate a textbook shock phenomenon with the almost vertical rise. Beyond this, the time for the pressure to rise to a maximum increases and the shape of the curve shallows. This is observed due the rarefaction wave catching up with the shock front as it is entering an already shocked medium and can travel at a faster rate than the front of the shock. By this point the wave has slowed to the speed of sound of the block and no further compressive failure or erosion occurs.

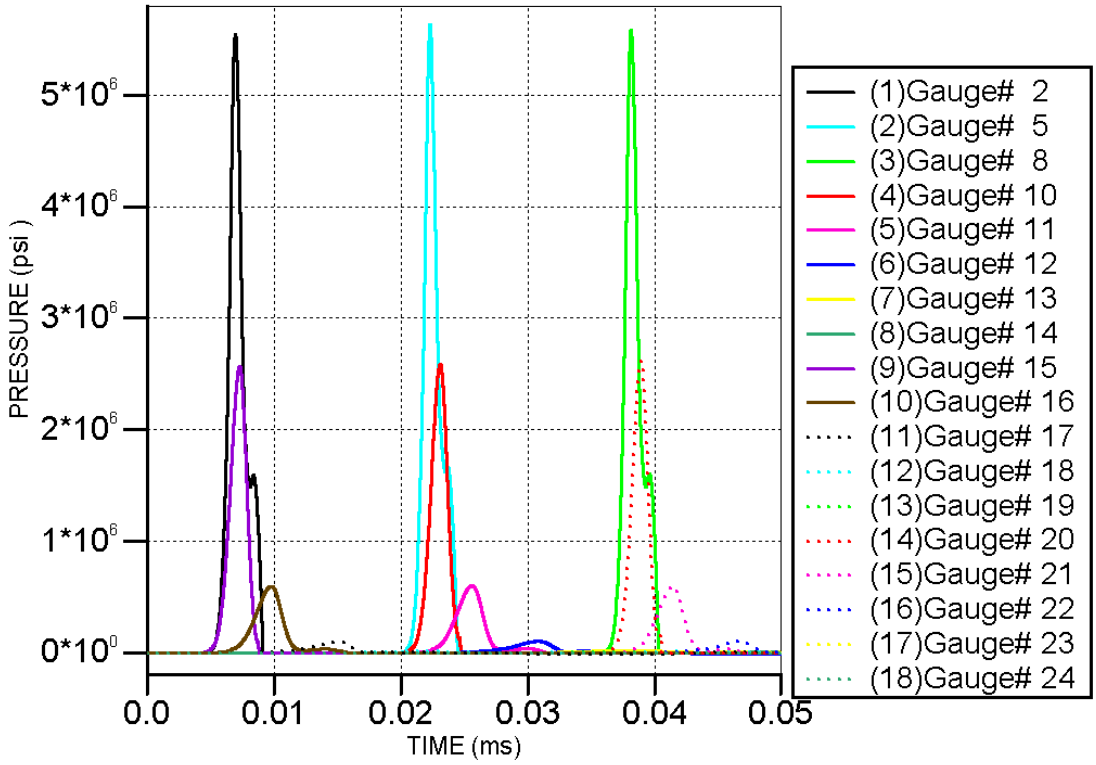

Figure 6-9: Pressure - Time increasing radially from the blast hole. Test 1

This phenomenon is represented by Cooper (1996) in Figure 3-9 and again in Figure 6-10. At the point where the shockwave has slowed to that of the rock, preconditioning due to shock pressure is complete and the fragmentation process continues with the expansion of gas pressure. This can unfortunately not be modelled in ANSYS as there is no equation or input for gas expansion through the block. Gas would be best modeled with an Euler grid. The only way for the full process for rock fragmentation to be simulated would be to have an embedded Euler and Lagrangian grid and the state change from one to the other once the shock pressure has passed through. Stress waves weaken in amplitude with time, and their role on further fragmentation replaced by expansion of explosion gasses into the cracks.

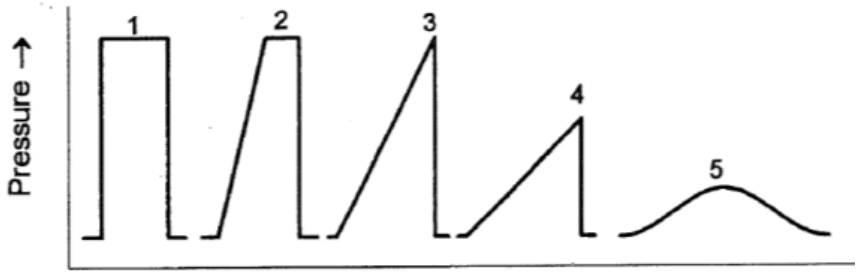

Figure 6-10: Progression of a shock wave

6.2.1.2 Test 3

Screen shots for Test 3 at times of 0.015, 0.025, 0.03, 0.035, 0.045, 0.055, 0065 and 0.1 ms are shown in Figure 6-11. Again, half of the block is shown as a cross section along the blast hole. The additional times shown compared with that of Tests 1 and 2 include a better representation of the shock collision due to the slower speed to the collision point compared to the Test 2. Symmetry exists at the midpoint due to initiation from both the bottom and top of the blast column. Contours displayed are the same as for Tests 1 and 2, ranging from a compressive pressure of 10000 psi in red to a tensile pressure of -1000 psi shown in blue displayed in Figure 6-1 in psi.

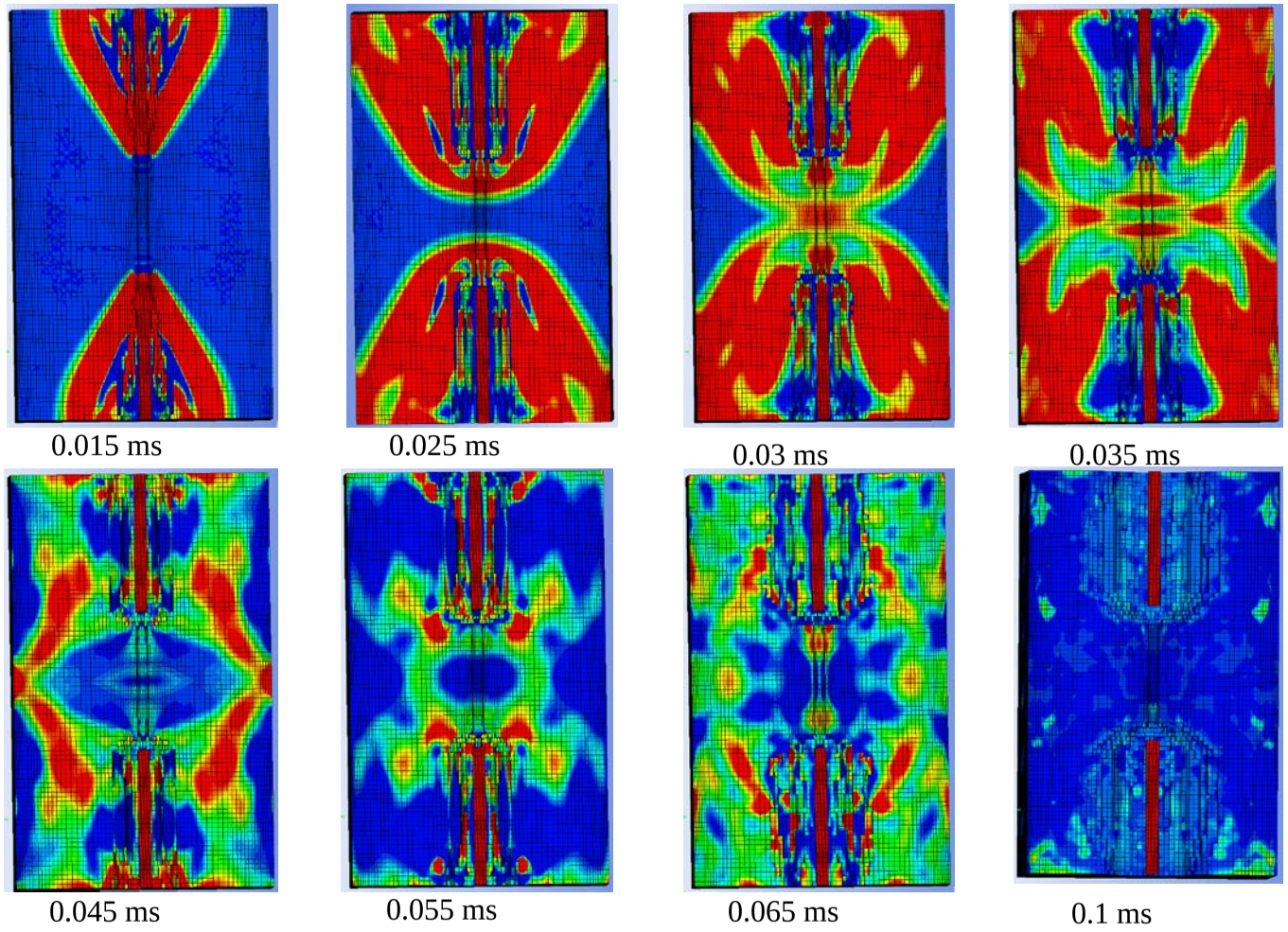

Figure 6-11: Sequence of model simulation for Test 3

At 0.015 ms the pressure contours are identical to that of Test 2. The shock pressure is still related to the detonation pressure and has a relatively shallow angle. The smaller the angle, the faster the wave is travelling. It can be seen from the very next picture, at a time of 0.025 ms, that the wave has slowed drastically as the detonation pressure ceases. The wave front is now almost completely flat as the two approach each other. At 0.03 ms the collision has occurred and what appears to be a reflection back from the two waves present, shown by the presence of blue tensile pressures just off the center line. This is assumed to be a reflection based on literature but the waves could also be passing through each other. Reflection occurs at the free face due to an impedance change, but this is not present within the block. A more intense observation of this reflection is visible at 0.35 ms. At 0.045 ms very interesting observations can be seen and are shown again in Figure 6-12 with an experimental picture.

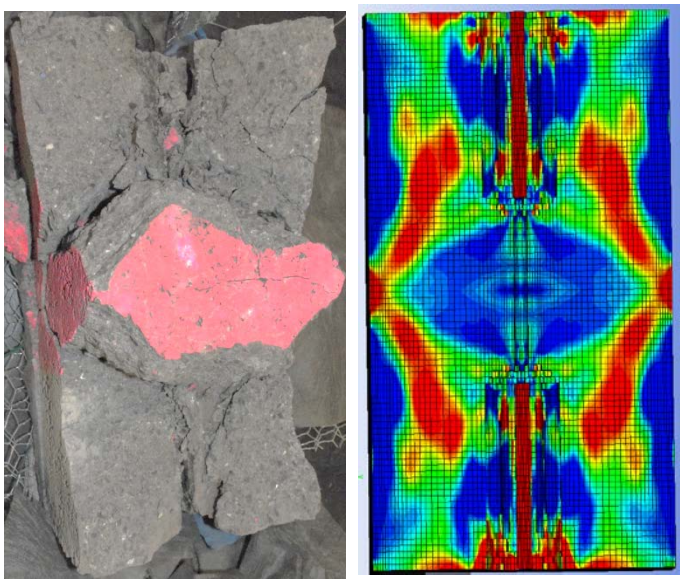

Figure 6-12: Large center fragment in Test 3 and tensile area in model simulation

The large block in the center of many of the experimental tests appears to match the shape of a tensile region resulting from the shock wave collision. Clearly, the stress is not great enough to break the block, but puts the material in a tensile stressed state.

The top of the block is shown in Figure 6-13 where the tensile pressure is again extending to the corners of the block, as in Tests 1 and 2, as well as the experimental investigation. Erosion ends only just beyond the explosive column before the pressure drops drastically.

This is the reason for not being able to see the whole way through to the other side, like in Test 1 and 2.

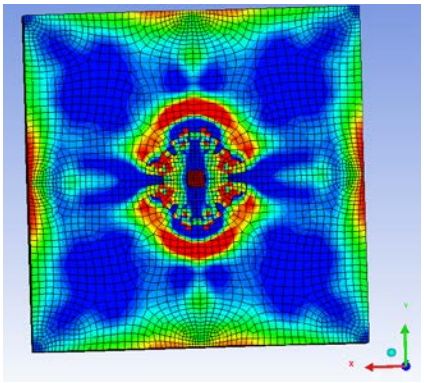

Figure 6-13: Top of block for Test 3

Figure 6-14 shows the pressure – time plot for the top and bottom of the block extending radially out from the center line on Test 3 where Figure 6-15 shows the middle portion of the block. Distance from the centerline in inches are approximately 0.2, 0.25, 0.5, 1, 2, and 4 at the edge of the block. The top and bottom of the block shows the same pattern as Test 1 and 2, where only compressive pressures are present and fail under compression out to 0.5 inches off center. It is Figure 6-15 that represents unique results for the shock collision area. This is the only gauge points that have represented tensile pressures as well as compressive. All six gauge points begin with compressive pressures and then become tensile as the trailing tensile waves meet at around 0.045 ms, the same time represented in Figure 6-12 where tensile contours are shown the entire width of the block. The greatest tensile pressure comes from gauge 11 in green; this is also the only point that tensile pressure exceeds the tensile pressure of the block of -1000psi, gauges 12 and 13 fall just short of the tensile failure zone. This makes clear the reason for some of the blocks creating a center tensile crack and some not. Only half of the block width has a tensile pressure great enough for failure. Inaccuracies in drilling and exact detonation length for a collision exactly in the center of the block will have a significant contribution as to whether a failure crack will occur. It should also be noted that the greatest tensile pressure occurs 1 inch out from the centerline. In all other tests, and the top and bottom of test 3, the greatest compressive strength occurs at the last hole wall, demonstrating the importance of the shape of the shock front on collision. The flat front of the shock front

in Test 3 has reflected back due to the larger collision area. Test 2, that has a sharp point at the front, has not reflected at all but sheared past each other and extended to the edge of the block possibly explaining the greater throw observed in the experimental tests. The gas pressure is not taken into account here, however.

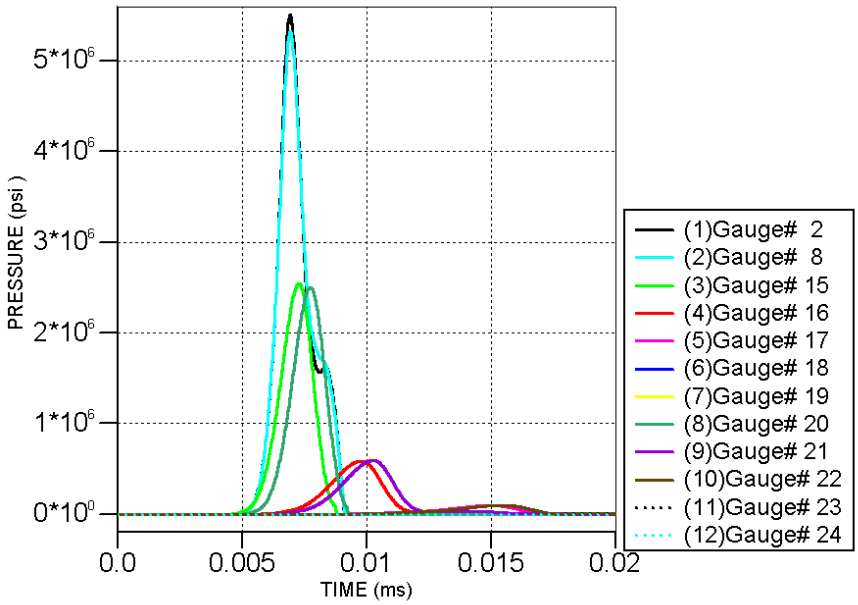

Figure 6-14: Pressure – Time plot for top and bottom of Test 3

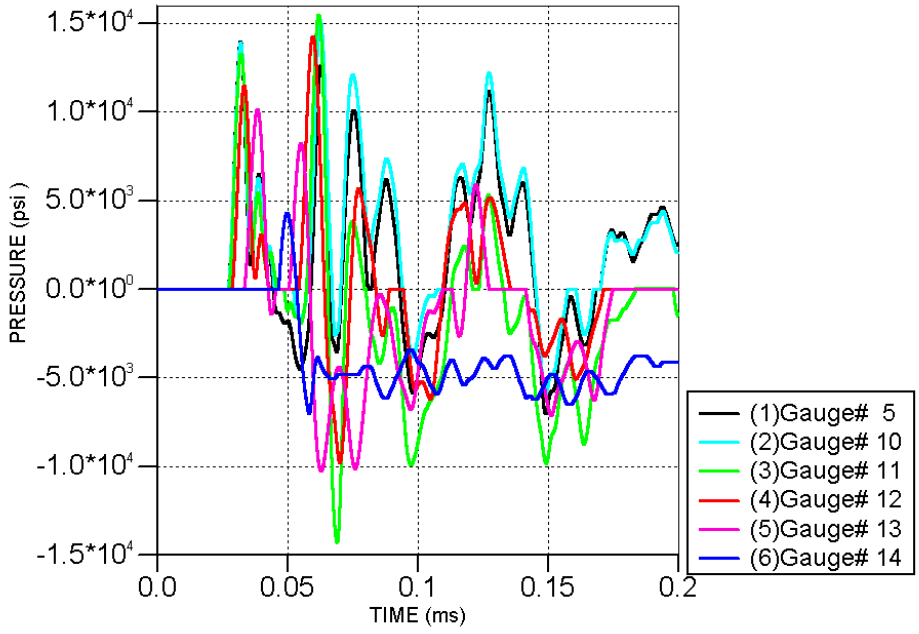

Figure 6-15: Pressure - Time plot for center of Test 3

6.2.2 Stress

Stress and pressure are a very similar relationship; both calculated by Force/Area and in this case are expressed in psi. Pressure is essentially an external force applied to a body, where stress is how that body counteracts the force that has been applied. Stress is also directional where P-Waves travel in the same direction as the external force, and S-Waves are proportional to the direction of the force. A compressive stress exerts a negative value, where a compressive pressure exerts a positive value, and vice versa. Stress was monitored through the model and the same conclusions made as with pressure. Pressure simply has higher values and clearer color change in the contours shown. A maximum Pressure exerted on the block reached above $5*10^6$ psi, whereas stress reached $-1*10^6$ (Figure 6-9 and Figure 6-16). Pressure and stress relate to the failure through the compressive and tensile strength of the material.

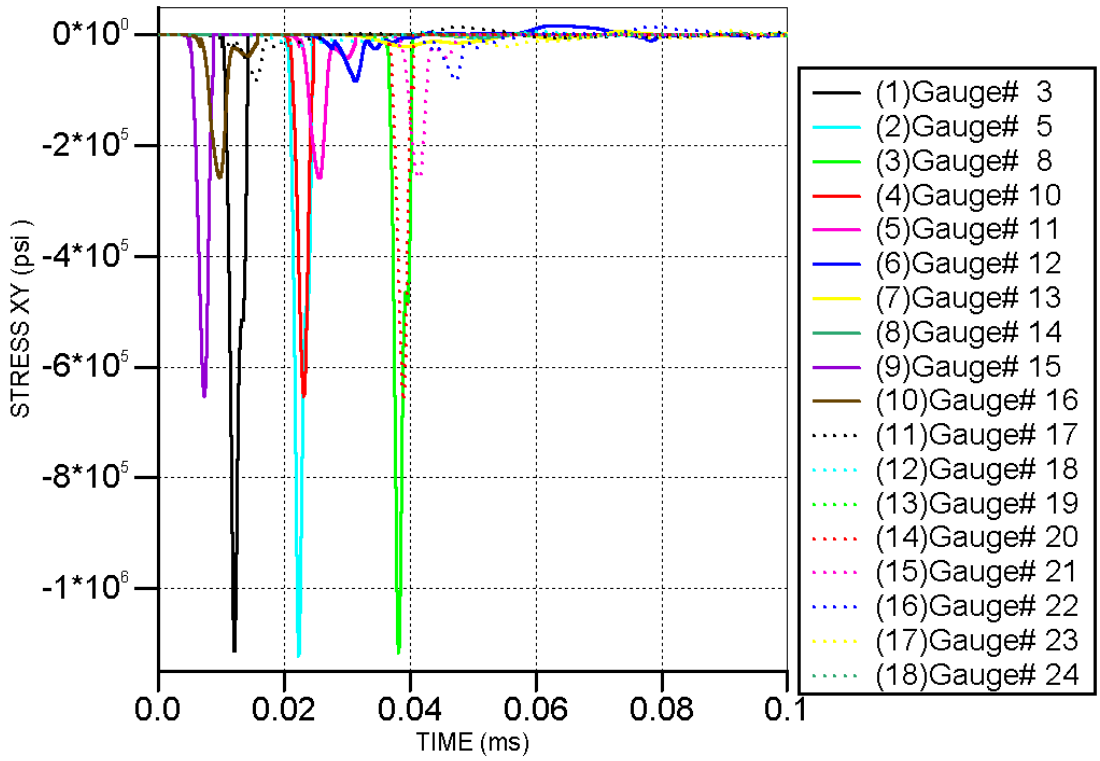

Figure 6-16: Pressure - Time increasing radially from the blast hole. Test 3

Figure 6-17 shows stress contours for all three tests at 0.025 ms. The scale goes from a negative compressive stress of -5000 psi to a positive tensile stress of 5000 psi. The high compressive stress surrounding the blast hole, along with a lower compressive stress with trailing tensile stress as the detonation travels can be seen. The same sharp angel for Test 2 compared to the shallow angle for Test 3 at the point of collision can also still be seen here.

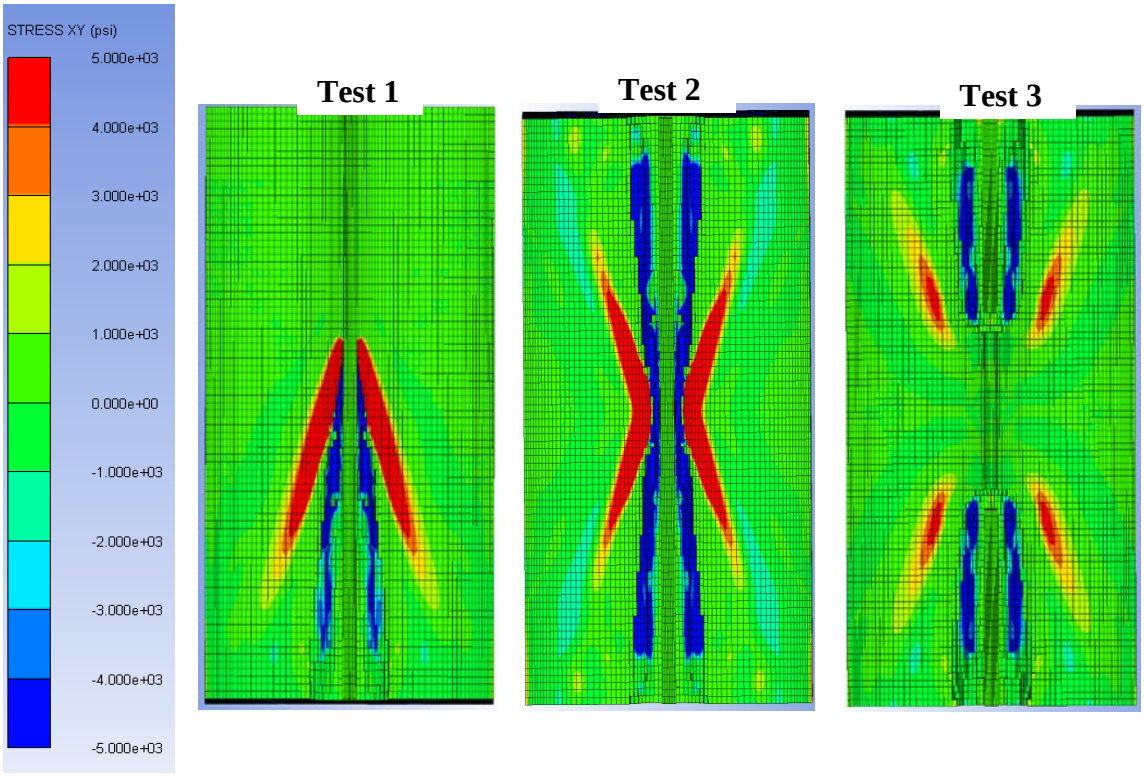

Figure 6-17: Stress at 0.025 ms for Test 1, 2 and 3

6.2.3 Damage

Damage is an output available from the RHT material model applied to the blocks. Contours are in a unit less scale from 0 to 1 where 0.7 is described as rubblized material and 0 no damage at all. The key is shown in Figure 6-18 with 1 in red and 0 in blue. It must be reiterated that only damage from the shock pressure is displayed but contour patterns give an indication of weakening where the gas pressure could expand. A lot of cells that would show a value greater than 0.7 around the blast hole have eroded so colors begin in the green range around 0.6.

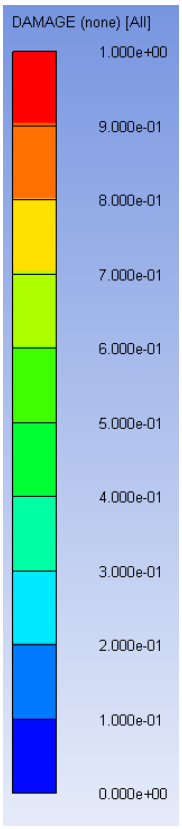

Figure 6-18: Damage contour key for Figure 6-19

Figure 6-19 shows a cross section through all three tests at a time of 0.025 and 0.075 ms. Greatest damage occurs in Test 2 where the two detonation waves have met and damage extends further from the blast hole. No damage is present in the center of the block in Test 3 but damage does extend around 1 inch further from the length of the blast holes.

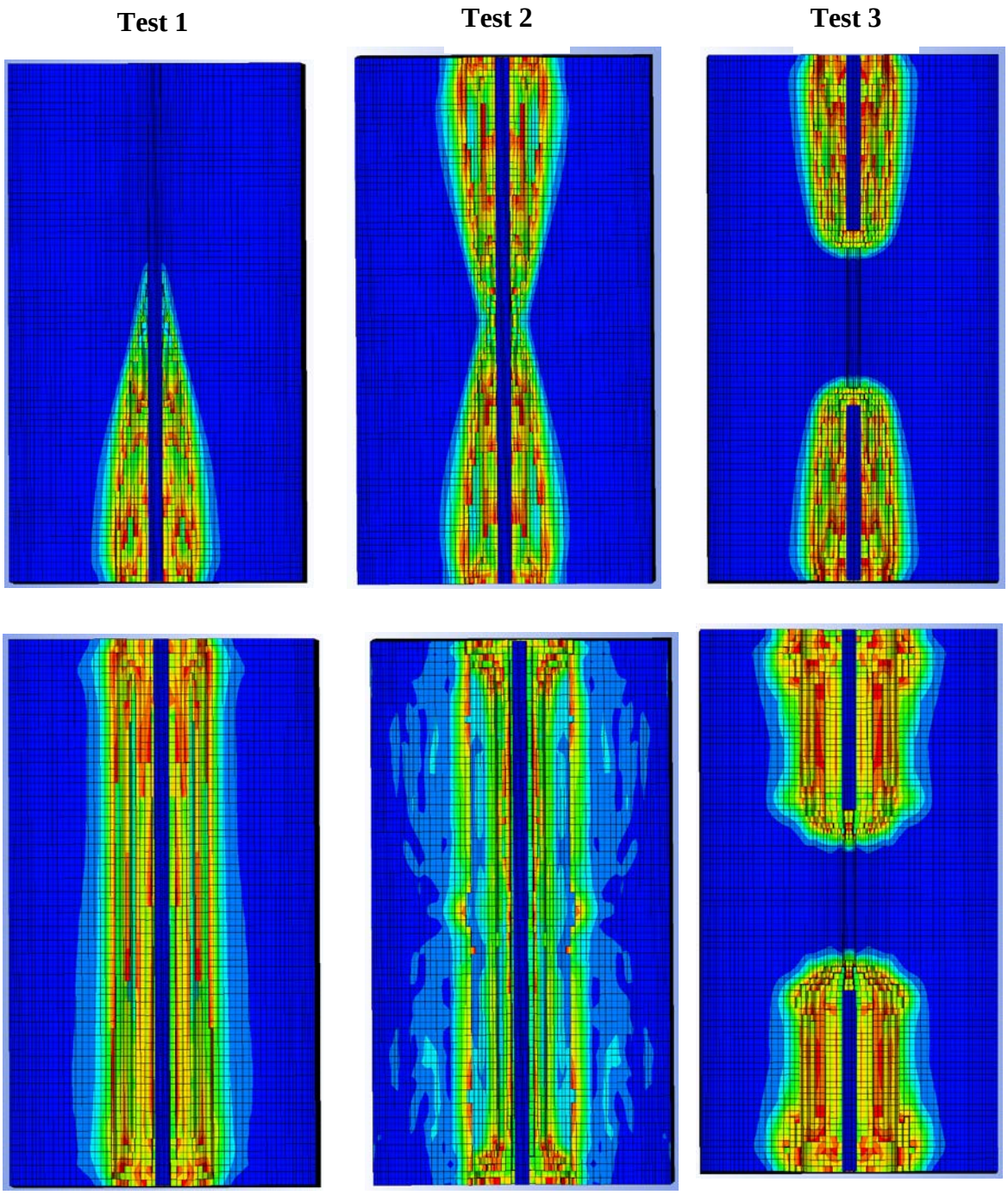

Figure 6-19: Damage contours at 0.025 ms (Top) and 0.075 ms (Bottom) for Tests 1, 2 and 3

Figure 6-20 shows the outside of the block for all three tests after 2ms, the longest the tests ran for. Damage reaching this far outside of the block is minimal due to the lack of the gas pressure phase. In order to see good contour patterns, the scale was reduced so that it only displays the lower end, from 0.3 to 0. It can clearly be seen that Test 2 has a horizontal area where damage is higher where the two detonation waves meet compared to Test 1 which only has vertical patterns. Greatest damage for Test 1 is at the end where detonation was initiated. Interestingly, Test 3 has no damage through the center where the two meet but shows the same pattern as the experimental tests where there is a large crack through the center vertically and a large block left in the center of the collision of shock waves occurs.

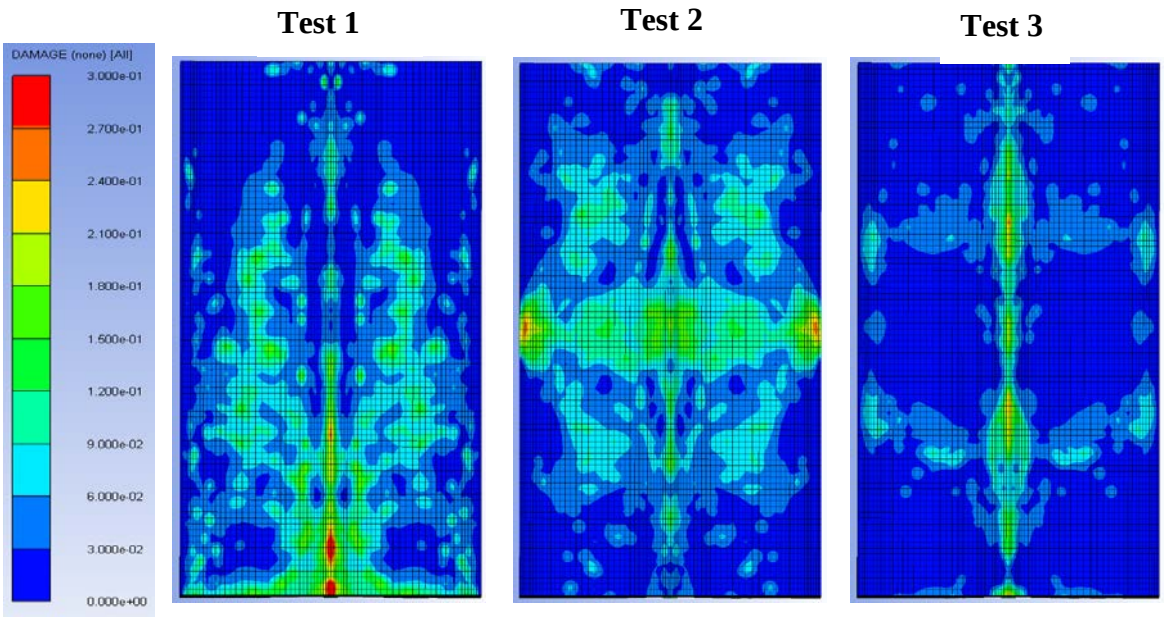

Figure 6-20: Damage on the outside of Tests 1, 2 and 3 at 2 ms

6.3 Conclusion

Many interesting observations have arisen from Chapter 6 where three model simulations were run in ANSYS Autodyn resembling the experimental tests described in Chapter 4. In Test 2 where detonation waves have collided show no evidence of shock wave reflection in the block. Instead, the waves have collided and taken on a 90 degree phase change and the pressure extended to the outside of the blocks. The compressive pressure at the point of collision is greater than that of the strength of the rock, explaining the single line crack in the experimental tests but most of the pressure extended to the sides

of the block. The additional throw shown in the high speed video footage experimentally could be attributed to this early fracture crack creating an easy path for gas escape in one location, sending the burden away from the face at a higher velocity at this point. Fragmentation has increased slightly over that of Test 1 where no collision occurs, but the drastic difference observed in the throw of the material could be excellent for cast blast design for surface coal mines. Additional throw can also impact secondary breakage where fragments further break upon collision with each other, or the muck pile.

Test 3, where shock waves collide have shown evidence of wave reflection through the simulated model. The reason for this over that of Test 2 has been attributed to the shape of the wave front when the two waves collide. In Test 3 the front is almost completely flat, giving a much larger surface area where collision is occurring. Reflection occurs at this point. In Test 2 the collision point is very narrow so the two waves have sheared past each other, and changed direction to the outside of the blocks. Test 3 has also provided good conclusion to the varying results displayed experimentally. The tensile pressure created at the center on the block is very similar to the failure strength of the concrete. A small change in experimental procedure through drilling of explosive burn rate could govern where a center line crack could occur. For the tensile strength to drop so significantly and not always fail at a distance of just 2.5 inches in a relatively weak material similar to that of shale or sandstone, little confidence is given to high fragmentation areas between blast holes where distances to the collision point can be as high as 10 feet.

Chapter 7. Correlation of Experimental and Simulation Results to a Full Scale Production Blast

7.1 Introduction

New technologies such as electronic detonators as well as strict environmental regulations have sparked discussion and new theories on improving the overall blasting process. The final product of a mining blast is optimized fragmentation for the products final use. When small particles are required and minimal boulders, mines have looked at the collision of detonation waves in one hole and colliding shock waves between adjacent holes to increase fragmentation in those locations.

Improvements to fragmentation and throw have been documented at mines using both top and bottom initiation in a single hole, but it is unclear as to the collision that is creating this, or the reduction in time it takes for the blast column to fully detonate. Theories have also been documented regarding two adjacent holes and the greatest fragmentation observed at the area between them where two shockwaves meet (yamomoto, 1999; and Rossmanith, 2003). Small scale tests have been carried out (Outcherlony, 2013) and model simulation (Preece and Lownds, 2008) that show no sign of an increase in fragmentation at short time delays that a shock collision could occur. These short time delays required for a shock collision are approaching instantaneous detonation, used for pre-split blasting. For this reason, others in the industry attribute the single crack joining adjacent holes in a pre-split to shock collision.

In an attempt to understand the fundamentals behind these two theories on dynamic stress wave collision and their effect on fragmentation, three tests were carried out both experimentally and model simulations. The Tests carried out were in small concrete masonry blocks of 15 inches high by $7^{7/8}$ inches wide. This scale is not representative of a large scale mining production blast, but correlations to this and industry recommendations are described throughout this chapter.

7.2 Colliding Detonation Waves

Interesting and significant progress on the theory of top and bottom initiation to collide detonation waves within each blast hole have arisen from the experimental and simulated tests described in this dissertation. It was initially thought that shock waves in the block created by the detonation waves would reflect back in the opposing direction. Simulation has shown that the shock waves in fact do not reflect at 180 degrees, but at 90 degrees. This is attributed to the small angle the shock wave contains at this collision point. The collision occurs at the maximum velocity of detonation of the explosive. The faster the detonation, the smaller the shock wave angle is, or the larger the Mach number. Figure 7-1 demonstrates the joined shock waves from the top and bottom initiation migrating to the outside of the block.

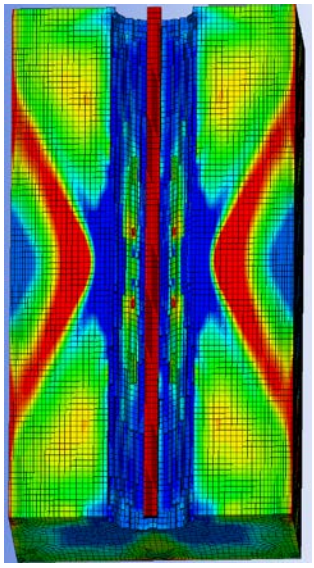

Figure 7-1: Shock wave reaching the outside of the block after detonation wave collision

The direction the shock wave is now travelling is significant for the throw of the muck pile. Verbal conversations with Dennis Johnson at Dyno Nobel (2014) has stated that clients have seen significant change in the throw distance of the muck pile when top and bottom initiation is used. This difference is of greater interest to them then the additional fragmentation. Throw is important when cast blasting. The aim of a cast blast is to move the muck pile to a different area of the mine. It is most often used in surface coal mine blasting where the aim is to remove, or simply move the overburden and expose the

coal underneath. Figure 7-2 shows a high speed video capture from the Test 1 and Test 2.

Figure 7-2: High speed video capture showing throw from the center of the blast.

Test 1 on the left of Figure 7-2 shows the throw is greatest from the top of the blast column. Test 2 has the largest throw at the center where the two waves have met. Although the difference between throw distances is not significant between top and center in these small tests, in a production blast the top of the blast column will be stemmed with inert material and no explosive present. This area at the top of the column is associated with large boulders as little work from the explosive power affects this portion of the bench. Pressure required to throw this area at the top of where fragments are at their largest would have to be much greater than at the center of the blast column where the fragments are smaller. For this reason, in a large scale production blast, throw would be improved when both top and bottom initiation is used. It is expected that the difference in throw would be greater than displayed in Figure 7-2 due to rock mass still present behind the row of holes being blasted. Rather than 4 directions for the throw of material, only 2 free faces will be present.

Fragmentation analysis of small scale tests have shown on average the mean particle size is lower for top and bottom initiation than just bottom initiation. At the area of collision, a single line crack was present in all tests, but the smallest fragments were grouped around the blast hole as in the test with single initiation. Using average particle size

(P50) to govern whether fragmentation has improved is not always ideal. If excessive boulder size is a problem a decrease in the mean will be a good indication of a smaller boulder size. If a lower overall fragmentation needs improvement for throughput of a crusher, then the modal fragment size may be of greater importance as an indication, or a reduction in the range of fragment sizes overall. Despite this, some difference is present in the fragmentation when top and bottom initiation is used. Model simulation of single initiation shows areas of greatest damage are at the bottom, where initiation of the blast column occurs. Clearly doubling the number of initiation points will increase damage contours overall as this area of increase will occur twice.

7.3 Colliding Shock Waves

A divide exists in the explosives engineering industry, most prominently between industry and some areas of academia, on the effects of shock collision on fragmentation. Shock collision has been associated with the single line crack formed in a pre-split blast, and to that of increased fragmentation between adjacent holes. Physics and logic show that both cannot coincide together and the basic principles of blasting for most make the reasoning of either difficult to comprehend. In an attempt to understand the phenomenon from first principles, small scale tests involving a head on collision of two shock waves through solid concrete were implemented.

The first major finding was that the angle of the shock wave front had a significant impact on the direction of wave travel after wave collision. The speed of the shock slowed drastically as soon as the detonation front ended creating a flat front to the wave as collision occurred. A reflection in the opposing direction occurred due to the large head on collision area. This differs drastically to the colliding detonation waves test where the combined waves travelled towards the free face and influenced the throw.

Figure 7-3 shows a comparison of experimental and simulated results for Test 3. The horizontal crack that was present in T3a but not the other 7 tests could be correlated here. The angled tension cracks and center collision crack follow the shape of the simulated shock wave almost perfectly. The point in which the Mach angled cracks leave the center horizontal crack also match that of the model simulation screen capture, and the highest tensile pressure recorded from the gauge points extending radially out from the

last hole. Additionally, the model screen shot shown on the right includes triangular areas of tensile stress at either side of the block at the center. Tensile cracks appear at this location in the experimental results.

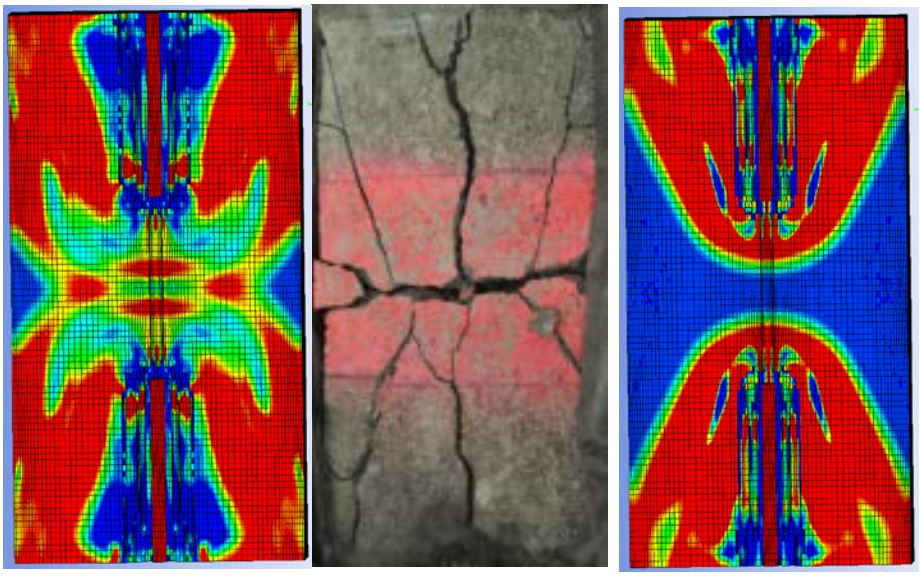

Figure 7-3: Comparison of experimental and simulated results for Test 3

Having correlation between experimental data and that produced from the model input is great for validation of the model and an understanding of crack source, but the real question is related to fragmentation between two adjacent holes. Figure 7-4 shows a simplified diagram of two adjacent holes with expanding shock wave as a result of column detonation. The angle of the shock wave as it meets is clearly not head on, as in Test 3. Due to this, it is not expected that a reflection back about the shock will occur, but some angle dependent on the speed of detonation and density of the rock.

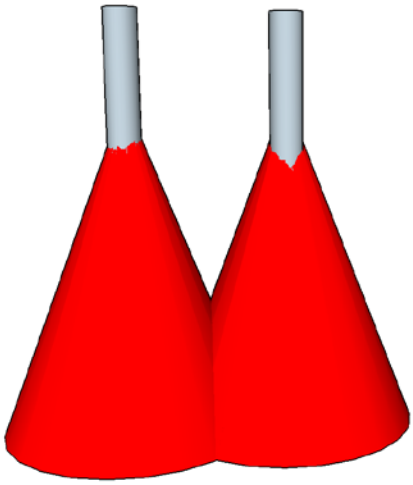

Figure 7-4: Shock Collision between adjacent holes

Of the three tests carried out experimentally, Figure 7-4 most closely resembles two blocks detonated like that of Test 1 sat next to each other (Figure 7-5).

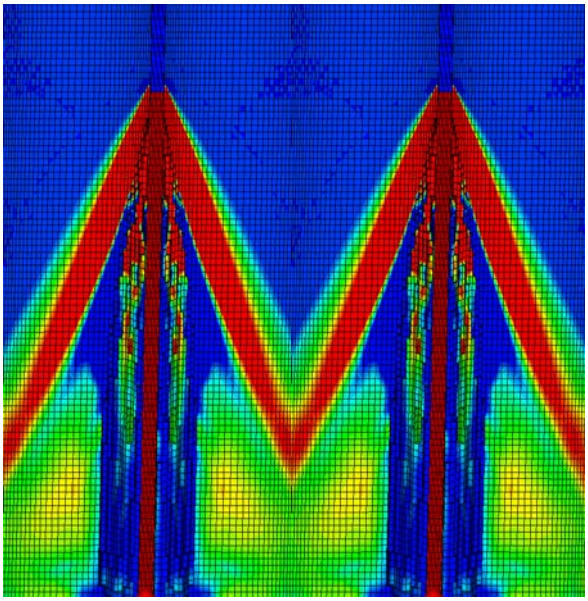

Figure 7-5: Two adjacent shock waves

Figure 7-5 is taken at 0.045 ms after detonation. Even at this short distance to the collision point, the pressure exerted by the shock wave was significantly less than just 4 inches away. Scaling this test by geometry to a typical hole diameter of 7 7/8 inches, the distance to shock collision is around 7 feet. The pressure remaining will be so minimal

by this point that if the shock has not already slowed to that of the rock, any collision is not expected to have any effect on additionally fragmentation. Distance between holes would have to be much closer together for any significant collision to occur. The collision that could occur is also not going to be the maximum it could be, like that of a head on, flat fronted shock collision.

Figure 7-6 shows a Lagrange diagram of the P-wave following two simultaneously detonated blast holes 7.875 inches apart, the same as in Figure 7-5. The diagram follows the same concept as Rossmanith (2003). Similarly Figure 7-7 shows a Lagrange diagram of two holes that are 7 feet apart, representing a full scale blast. The same explosive is used in both tests so the speed of the shock remains constant. On first look, they appear the same, but the interesting thing to note is the time of shock collision, 0.025 ms and 0.25 ms for Figure 7-6 and Figure 7-7, respectively.

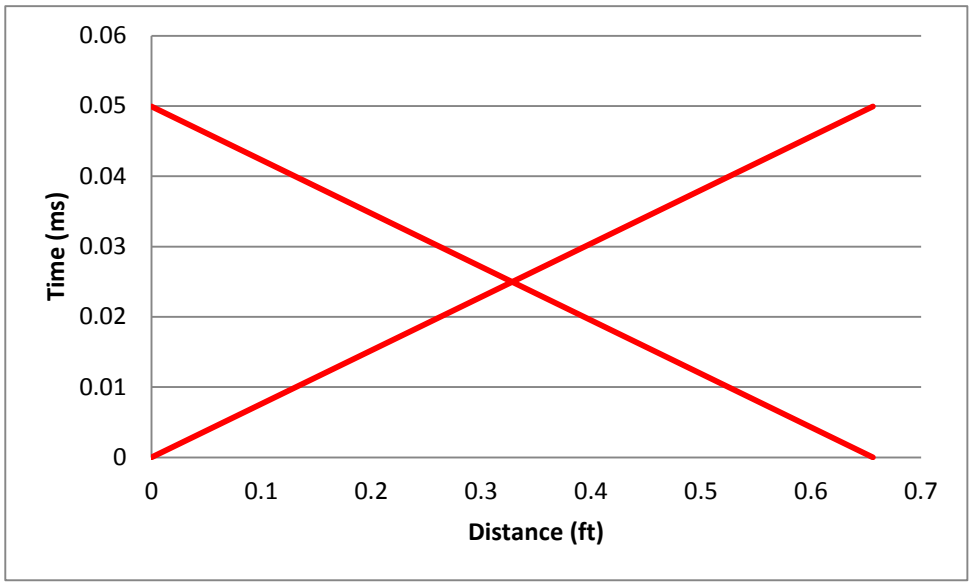

Figure 7-6: Lagrange diagram showing P-Wave from two blast holes 7.875 inches apart

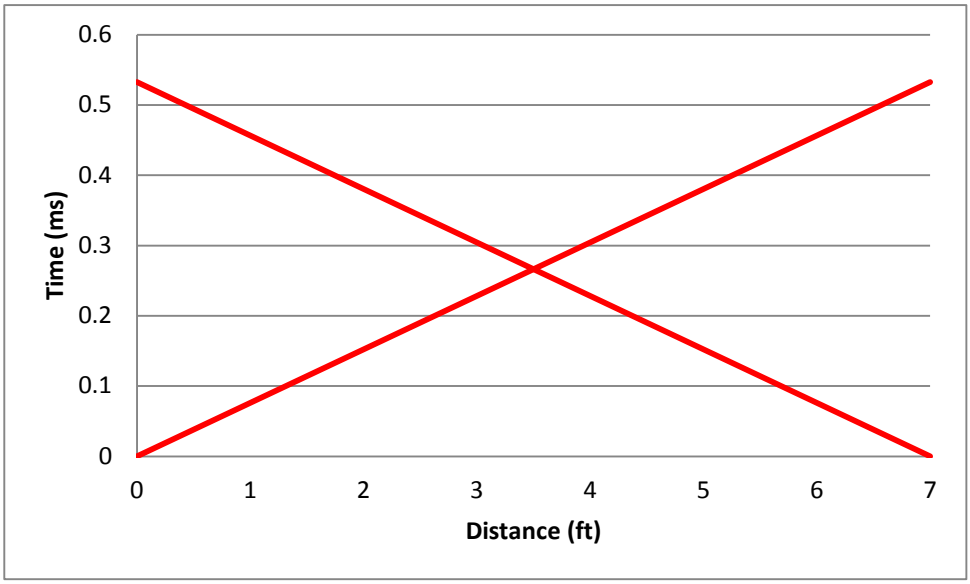

Figure 7-7: Lagrange diagram showing P-Wave from two blast holes 7 feet apart

Model simulation has shown that after 0.045 ms, the pressure from the shock wave is almost negligible. After 0.25 in a full scale blast, the gas pressure phase will have easily taken over the shock pressure as the primary cause of fragmentation. If a time difference between blast holes occurred, this would further reduce the likelihood of a shock collision occurring.

Oversimplification of the shock collision process by Rossmanith has been identified by Johansson and Ouchterlony (2013) and Katsabanis et al (2014). Lagrange diagrams have been found to be impractical for shock collision because as the shock front passes the material, it changes to Eulerian state. Reviewing the simple depiction of particle velocity compared to shock velocity using Popsicle sticks by Cooper (1996) an addition factor not considered by Rossmanith becomes apparent. Figure 7-8 shows the same 11 Popsicle sticks with equal width to distance that Cooper (1996) used to demonstrate the difference between particle velocity and shock velocity. The blue line depicts the particle velocity travelling at a faster rate than the red shock velocity. On the left is a single blast hole, like that demonstrated by Cooper. On the right, however, a second blast hole is taken into consideration and collision occurring by the sixth round of Popsicle sticks.

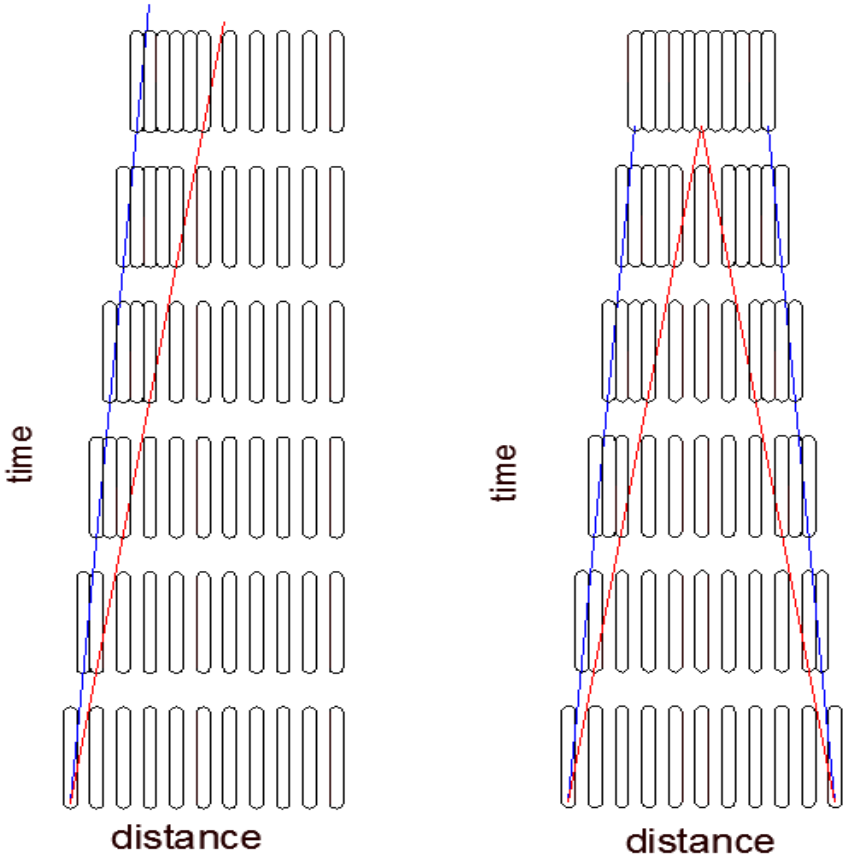

Figure 7-8: Depiction of shock and particle velocity

By the time of the shock collision, all particles will have also moved and are packed closely together, increasing the density of the rock mass. Particles can no longer pass in this same direction, and the pressure required to push all the particles in the reverse direction will be much greater. At the point of collision, have the particles actually moved in the direction of the shock front and increased the density and therefore strength of rock at the point of shock collision, making the pressure required to break the material at this point even greater than the general rock mass? If this is the case, any form of shock collision should be avoided. When a free face is present, this directional particle velocity gets relief at the free face where impedance change allows for spall and tensile failure. The same cannot be said in between two blast holes.

7.3.1 Pre-split theory for shock collision

A pre-split blast is used in construction road cuts to split hard rock almost vertically. Simply blasting the rock would create significant back break and loose material that could fall over time. The pre-split allows a very stable high angle wall to be created through a single crack between adjacent holes. A number of small holes relatively close together are loaded with a low quantity of explosives or decoupled explosive and shot simultaneously before the rest of the production blast. The same principle is used at a mine site when highwall stability is of concern.

Although no experimental tests were carried out regarding pre-splits specifically, the idea thought by many and documented in the ISEE handbook (2011) that a shock collision is the cause of the straight line crack, was kept to mind. Results demonstrated in no test, or that of the model simulation indicate a crack joining the detonation columns. If shock waves were influencing a pre-split, the direction of the crack would be in between the two holes at a 90 degree angle, not joining them. The shock pressure between holes has shown in model simulation to slow drastically as soon as it dissipates slightly from the detonation. The strength of the shockwave from detonating cord, also often used in a presplit, is not great enough to crack a 5 inch block of concrete in the scaled tests investigated. For this reason there seems no logical way that the shockwave will be of great enough strength to crack the hard rock strata often round either side of a highway. Furthermore, the result of decoupling the explosive the full length of the hole when using detonating cord in a larger diameter hole, or just loading packaged explosive in the base of the hole and leaving air above essentially reduces the effect of the shock pressure at the blast hole wall. This will result in a very short distance around the blast hole before the shock pressure will have slowed to that of the rock and reduced in pressure so no crack formation can occur. In essence the shock pressure produced from a pre-split will be so minimal by the time it reaches another wave that crack formation would be almost impossible even in the softest of materials. This, coupled with the fact that experimental and model simulation put this crack at a perpendicular direction to that produced in a pre-split, make the theory doubtful.

Further work in this specific area is needed to set any firm conclusions, but it is far more reasonable to attribute the single crack joining adjacent blast holes to that of hydrofracture. Small cracks will occur around each blast hole that is detonated simultaneously due to the low shock pressure present. The gas pressure phase will expand through these but due to the large volumes of rock in all directions and no free face, the easiest path for the gas pressure to get relief is to that of the next hole.

7.4 Conclusions

Different shock collisions have been observed between detonation waves and shock waves. Critical variables that affect the level of shock collision are the angle of the shock front when shock collision occurs and consequently the shock velocity. The shock velocity quickly dissipates with distance. Distance between holes would have to be small for a shock interaction to occur even at instantaneous detonation. As time between holes increases, the likelihood of a shock collision decreases. Particle velocity is not taken into consideration in any of the Lagrange diagrams previously published in literature. It appears that as the particle velocity travels in the direction of the shock, distance between particles at this point decreases and effectively strengthens the rock strata at this point. If this is the case then fragmentation at this point would actually decrease compared to that of the main rock mass. Detonation wave collision has found to be beneficial for additional throw of material due to the higher shock wave pressure at the collision point travels in the direction of the free face.

Chapter 8. Conclusions

Shock wave collision with respect to fragmentation all leads back to timing. At the time most fragmentation models were implemented, precise timing through electronic initiation was not possible, or even considered. The effect of timing between holes and fragmentation is discussed in two ways: with respect to wave collision between holes and distance to the nearest free face. These two theories are contradictory since the former requires short timings due to the supersonic velocities the waves travel and the latter long delay times between holes in order for the material to move out the way through gas heave and the new free face created. Only one phenomenon can influence fragmentation at a time and timing designed for either one or the other.

Short timing delays have been investigated experimentally and through material models between adjacent holes by Johansson and Ouchterlony (2013) amongst others. Fragmentation was measured and it was found that short delays did not improve fragmentation but reduce it. With this being said, fragmentation results demonstrated boulders and fine particles, not the even distribution typical of a bench blast. This was due the material used and additional free surfaces. Although good work, no convincing conclusions result and people are still unsure on the effects of shock collision. Due to the previous difficulty in scaled experiments with multiple holes, a single hole was used and a head on collision of shock waves investigated in this dissertation. Head on collision of both detonation waves and shock waves were investigated experimentally and model simulations carried out. It was found that the angle of the shock front is the major contributing factor in the degree of shock reflection.

Simulation results demonstrated the small angle about the blast column of the shock wave following a detonation front due to the supersonic speed of travel. As two of these collided, the waves did not reflect back on themselves but directed towards the free face, influencing the throw of the material more than the fragmentation. Experiments demonstrated an additional tensile crack through the center of the block where waves collided. No small fragments were present at the point of collision but were grouped around the blast column, the same as the single initiated test where no collision was

present. The one additional crack provided an easy escape for the expanding gas pressure that follows the shock front. The gas pressure congregating here pushes the fragments away from the face at a greater velocity. It is expected that this process will significantly influence surface mine blasting where cast blasting is used. Top and bottom initiation has been timed to target a band of harder rock through the height of the blast face. The results gathered indicate that this will not actually improve the overall fragmentation significantly at this location but simply apply a single crack through the center of that band. The gas pressure that would otherwise continue expanding hairline cracks will escape out the front of the face and reduce fragmentation at this location. The smaller average particle size found in experimental data is likely due to a smaller boulder size from the crack formed in the center. It is expected that an ideal strata for top and bottom initiation is one that is highly fractured already and does not require high volumes of gas pressure for fragmentation but the throw of material of interest for a cast blast.

Shock collision between two blast columns has produced a flat front to the shock wave, as opposed to the small angled front for detonation wave collision. Here, a reflection of the two waves does occur and the center of the block put in a state of tension. This center location has shown to contain the largest fragments in the block. In 3 of the 8 blocks tested a center crack has been produced and the other 5 contain a single large fragment with no crack through the center. The tensile pressure produced from the collision was very close to that of the tensile strength of the block and is the reason for inconsistency in results. Despite this, even at this short distance with a head on collision of the shock fronts it is far from the ‘area that contains greatest fragmentation’ suggested by Rossmanith (2003) and Yamamoto (1999). Between adjacent blast holes, the angle of shock where the two would meet is not head on and the effects of the shock wave would be even less than shown in these experiments. Another significant observation from the experiments carried out is the lack of inclusion of the particle velocity in the Lagrange diagrams produced to date. The directional movement of the particles as the shock velocity passes through from each blast hole congregate at the center location where the collision would occur. This effectively increases the density and strength of the material at this location, probably reducing fragmentation rather than improving it.

The top of the blocks show radial cracking about the blast hole. This is a typical pattern due to the even pressure distribution in all directions about the cylindrical blast hole. The textbook pattern is amplified here due to the additional free faces not present in a bench blast. Significant findings came when comparing this to the model simulations where areas of tensile pressure congregate in the same areas. Radial cracking about the blast hole is thought to originate from the initial compressive pressure followed by the gas pressure extending some of these along lines of greatest weakness already present in the rock. What model simulations have shown is that the shock pressure actually creates areas of weakness, rather than them already being present in the rock mass. Gas pressure travels along the path of least resistance, the preferential paths of tensile pressure created by the shock are vital for this.

BIBLIOGRAPHY

Adhikari, G. R., Venkatesh, H. S., Theresraj, A. I. Roy, S., Balachander, R. Jain, N. K., and Gupta, R. N., Role of Blast Design Parameters on Ground Vibration and Correlation of Vibration Levels to Blasting Damage to Surface Structures. National Institute of Rock Mechanics, September, 2005.

ANSYS. "Introduction to Autodyn – Chapter 1". Training Manual, ANSYS Inc. 2009

ANSYS. "Online Help and Product Support. Available from the World Wide Web:<www.ansys.com>. Accessed September 30th 2014

Ash, R. L., "Good Blasting Practice: Need for Uniform Standards", Proceedings of the Annual Conference on Explosives and Blasting Technique, 1975

ASTM C39/C39M-12. "Standard Method for Compressive Strength of Cylindrical Concrete Specimens" ASTM International. 2012.

Atlas Powder. "

Bajpayee, T.S., Bhatt, S.K. "Fatal Accidents due to Flyrock and Lack of Blasting Area Security and Working Practices in Mining", Pittsburgh, Pennsylvania: National Institute for Occupational Safety and Health, 2003

Bajpayee., T.S., Mainiero, R.J. "Firing accuracy of electric detonators. International Society of Explosives Engineers, General Proceedings., pp 89-98, 1990.

Bajpayee, T.S., Verakis, H.C., Lobb, T.E., "An Analysis and Prevention of Flyrock Accidents in Surface Blasting Operations", Center for Disease Control, 2004

Ben-Dor. G., Takayama. K. "The Phenomena of Shock Wave Reflection – a Review of Unsolved Problems and Future Research Needs". Shock Waves. 1992.

Berg, V. S. and. Preece, D. S., “Reinforced Concrete Structure Failure Mechanisms Resulting from Explosively- Induced Overpressures”, Proceedings of the 30th Annual Conference on Explosives and Blasting Technique, International Society of Explosives Engineers, New Orleans, LA, February, 2004.

Bauer, F. “Blast Optimization through Long Term Fragmentation Analysis” Proceedings of the fortieth Annual Conference on Explosives and Blasting Technique, International Society of Explosive Engineers, Denver, CO. February 2014

Blair, B. E., and Duvall, W. I., Evaluation of Gages for Measuring Displacement, Velocity, and Acceleration of Seismic Pulses. United States Department of the Interior – Bureau of Mines, Report of Investigations 5073, Washington, D.C., April 1942.

Borrvall, T., Riedel, W. “The RHT Concrete Model in LS-DYNA” Eighth European LS-DYNA Users Conference, Strasbourg, May 2011.

Broek, D. The Practical Use of Fracture Mechanics. Kluwer Academic Press. 1988

Brown, E. T. “Rock Classification, Testing and Monitoring: ISRM Suggestion Methods” Pergamon Press (1981)

Butcher, B M, & Karnes, C H (1968). Sandia Labs. Res Rep. SC-RR-67-3040, Sandia Laboratory, Albuquerque, NM, April 1968

Carroll, M M, & Holt, A C (1972). “Static and Dynamic Pore Collapse Relations for Ductile Porous Materials.” J. Appl.Phys., 43, 4, pp1626 et seq., 1972

Chaiken, R. F, Cook, E. B, Ruhe, T. C., "Toxic Fumes from Explosives: Ammonium Nitrate-Fuel Oil Mixtures", 1974.

Clark, D., Larson, B., and Lande, G., Vibration: Its Effect & Measurement technique at or near dwellings" Proceedings of the 19th Conference on Explosive and Blasting Technique. 1983.

Clark, G.B. Principles of Rock Fragmentation. J.Wiley & Sons. 1987

Cook, M. A. "The Science of Industrial Explosives". Graphic Services and Supplies, Inc. 1974.

Cooper, P. W., "Explosives Engineering". Wiley-vch, USA. 1996

Cunningham, C.V.B., The Kuz-Ram Fragmentation Model – 20 Years On. Briighton Conference Proceedings 2005, African Explosives Limited, Modderfontein, South Africa, 2005: 201-210

Dick, R. A., "A Review of the Federal Surface Coal Mine Blasting Regulations", Proceedings of the Annual Conference on Explosives and Blasting Technique, 1979

Djordjevic, N., A Two-Component Model of Blast Fragmentation. The AusIMM Proceedings, November, 2 1999: 9-13

Dobratz, B. M., P. C. Crawford. "LLNL Explosives Handbook: Properties of Chemical Explosives and Explosive Simulants. University of California; Lawrence Livermore National Laboratory"; Report UCRL-5299; Rev.2;. 1985

Duvall, W. I., and Fogelson, D. E., Review of Criteria for Estimating Damage to Residences from Blasting Vibrations. United States Department of the Interior – Bureau of Mines, Report of Investigations 5968, Washington, D.C., 1962.

Edwards, A. T., Northwood, T. D., "Experimental Studies of the Effects of Blasting on Structures". The Engineer: Technical Contributors Section, September 30, 1960: 538-546

EPC UK. "Shotfirer Training Course Notes" Edwinstowe, UK. 2010

Exedaktylos, G.E., C. Haycocks, Y. Zhou, "Computer-Aided Blast Fragmentation Prediction", Proceedings of the Annual Conference on Explosives and Blasting Technique, 1989

Fedkiw, Ronald P., Coupling an Eulerian Fluid Calculation to a Lagrangian Solid Calculation with the Ghost Fluid Method, Journal of Computational Physics, V 175, I 1, pp: 200-224. January 2002

Fletcher, L.R., D.V. D'Andrea, "Control of Flyrock in Blasting", Proceedings of the Annual Conference on Explosives and Blasting Technique, 1986 Academic Press Professional, Inc. San Diego, CA.

Fogelson, D. E., D'Andrea, D. V., Fischer, R. L. "Effects of Decoupling and Type of Stemming on Explosion-Generated Pulses in Mortar: A Laboratory Study" Proceedings of the 26th Conference on Explosives and Blasting Technique. Anaheim, CA. 2000.

Forbes, J. W. Shock Wave Compression of Compressed Matter. Springer. Berlin (2012)

Herrmann, W. "Constitutive Equation for the Dynamic Compaction of Ductile Porous Materials", J. Appl. Phys., 40, 6, pp 2490-2499, May 1969

Hissem, D. W, "How to Improve Safety, Create Value, and Maximize Profit in the 'New Economy', Proceedings of the Annual Conference on Explosives and Blasting Technique, 2013

Ireland, A. T., Design of Ari-Blast Meter and Calibrating Equipment. United States Department of the Interior – Bureau of Mines, Technical Paper 635, Washington, D.C., 1942.

ISEE (1998). Blasters' Handbook 17th Edition. International Society of Explosives Engineers, Ohio, USA.

ISEE (2011). "Blasters' Handbook 18th Edition". International Society of Explosives Engineers, Ohio, USA.

Iverson, S. R., Hustrulid, W. A., Johnson, J. C. "A New Perimeter Control Blast Concept for Underground Metal/Nonmetal Drifting Applications" Report for investigations 9691. Department of Health and Human Services. Pittsburgh, PA and Spokane WA. March 2013.

Johansson. D., Outcherlony. F. "Shock Wave Interactions in Rock Blasting: The Use of Short Delays to Improve Fragmentation in Model Scale". Rock Mechanics and Rock Engineering 46:1-18. 2013.

Kanchibotla, S.S., W., Valery, "Mine to Mill Process Integration and Optimization - Benefits and Challenges", Proceedings of the Annual Conference on Explosives and Blasting Technique, 2010

Kanchibotla, S. S, Valery, W, and Morrell, S. Modelling Fines in Blasting Fragmentation and its Impact on Crushing and Grinding. Explo '99, Kalgoorlie, WA, 7-11 November, 1999: 137-144

Katsabanis, P. D., Liu, L., "Delay Requirements for Fragmentation optimization, Measurement of Blast Fragmentation. Belkema. 1996.

Katsabanis, P., Omidi, O., Rielo, O., Ross, P. "A review of Timing Requirements for Optimization of Fragmentation". Proceedings of the 40th Conference on Explosives and Blasting Techniques. Denver CO. February. ISEE. 2014

Katsabanis, P., Omidi, O., Rielo, O., Ross, P. "Examination of Timing Requirements for Optimization of Fragmentation Using Small Scale Grout Samples". Blasting and Fragmentation. Volume 8, Number 1. August 2014.

Katsabanis, P. D., Tawadrous, A., Braun, C., Kennedy, C. "Timing Effects on Fragmentation" Proceedings of the 32nd Oncference on Explosives and Blasting Technique. Dallas, TX. USA. 29th Jan – 3rd Feb. 2006.

Kleine, T.H., A.R. Cameron, "A Blast Fragmentation Measurement and Prediction System for Blast Optimization", Proceedings of the Annual Conference on Explosives and Blasting Technique, 1997

Kosanke, K. L., Kosanke. B. J., Sturman. B. T., Winokur. R. M. “Encyclopedic Dictionary of Pyrotechnichnics (and related subjects)” Journal of Pyrotechnicas. 2012.

Kopp, J. W., Siskind, D. E., Effects of Millisecond-Delay Intervals on Vibration and Airblast From Surface Coal Mine Blasting. United States Department of the Interior – Bureau of Mines, Report of Investigations 9026, Washington, D.C., 1986.

Kuznetsov, V. M., The Mean Diameter of the Fragments Formed by Blasting, Institute of Mining, Siberian Branch, Academy of Sciences of the USSR, Novosibirsk, October 17, 1972.

Lashgari, A., Johnson.,C. E., Kecojevic, V., Lusk, B. T., Hoffman, J. M., NOx Emission of Equipment and Blasting Agents in Surface Coal Mining. Appalachian Research Initiative for Environmental Science, 2012

Lee, F. W., Thoenen, J. R., and Windes, S. L., Earth Vibrations Caused by Quarry Blasting, Report of Investigations, Department of the Interior – Bureau of Mines, November 1936.

Lee, N. and Lusk, B.T., ANFO vs. 100% Emulsion: Quantitative Assessment of Performance with Constant Drilling and Blasting Costs, Blasting and Fragmentation, Vol. 6 No.1, November, 2012: 1-22

Leppanen, J. “Concrete Subjected to projectile and Fragment Impacts: Modelling of Crack softening and Strain Rate Dependency in Tension. Int. J. Impact Eng. 32. 2006. pp. 1828-1841

Liepmann, H.W., Roshko, A. “Elements of Gas Dynamics”. Dover Publications Inc, New York. 2001

Lilly, P. A, An Emperical Method of Assessing Rock Mass Blastability, The AusIMM/IE Aust Newman Combined Group, Large Open Pit Mining Conference, University of Queensland, October 1986: 89-92

Little, T.N., "Flyrock Risk" Carine, Australia: TNL Consultants, 2007.

Lusk, B. Hoffman, J. Wedding, C., "Electronic Detonator and Modern Non-Electric Shocktube Detonator Accuracy." Proceedings of the Thirty-Seventh Annual Conference on Explosives and Blasting Technique. San Diego, CA, February 6-9, 2011.

Lusk, B. Silva, J, Eltschlager K., Field Testing and Analysis of Blasts Utilising Short Delays with Electronic Detonators. OSM Final Report: S09AP15632. 2012.

Lusk, B., Schonberg, W., Baird, J., Woodley, R., Noll, W. "Using Coupled Eulerian and Lagrangian Grids to Model Explosive Interactions with Buildings" 25th Army Science Conference, Orlando FL, USA. 2006

MacKenzie, A.S., Cong. J., "Cost of Explosives−Do You Evaluate it Properly?" May 1966: 32−41

Madearis, K., The Development of Rational Damage Criteria for Low-Rise Structures Subjected to Blasting Vibrations. Kenneth Medearis Associates, Research, Engineering, Computer Consultants, Fort Collins, Colorado, June 22-24, 1977.

Mainiero, R. J. 1997. "A Technique for Measuring Toxic Gases Produced by Blasting Agents". Proceedings of the Twenty Third Annual Conference on Explosives and Blasting Technique, Las Vegas

Martin, R. J. Boyd, P. J. "Characterization of Damage in Anisotropic Rock Due to Buried Explosions" proceedings of the 46th US Rock Mechanics / Geomechanics Symposium, 24 – 27 June 2012

Martin, R., Boyd, P., Stroujkova, A., Leidig, M., Lewkowicz, J,. Bonner, J. "Correlating Near-Source Rock Damage From Single-Hole Explosions to Seismic

Waves". Proceedings of the 2011 Monitoring Research Review – Ground-Based Nuclear Explosion Monitoring Technologies, 13 – 15 September 2011, Tucson, AZ, Volume I, pp 483-494.

McHugh. S. "Crack Extension caused by Internal Gas Pressure compared with extension cause by Tensile Stress". International Journal of Fracture 21. Netherlands. 1983.

Muller, B., Litschko, B., Pippig, U. "The Sonic Effect: Revolutionizing Drilling nad Blasting". 2013

Nicholls, H. R., Johnson, C. F., and Duvall, W. I., Blasting Vibrations and Their Effects on Structures. United States Department of the Interior – Bureau of Mines, Bulletin 656, Washington, D.C., 1971

Northwood, T. D., Crawford, R.., and Edwards, A. T., Blasting Vibrations and Building Damage. The Engineer: Technical Contributors Section, May 31, 1963: 973-978

Onederra, I, Bailey, V, Cavanough, G, Torrance, A., "Understanding main Causes of Nitrogen Oxide fumes in Surface Blasting", Institute of Materials, Mineral and Mining, 2012.

Ouchterlony, F., The Swebrec Function: Linking Fragmentation by Blasting and Crushing. Institute of Materials, Minerals and Mining & Australian Institute of Mining and Metallurgy, Stockholm, Sweden, 2005: Vol 114, A29-A44

Ozdemir, K., Kahriman, A., Ozer, U., and Turner, G., Relation Between Excavator Bucket Loading Time and Particle Size Distribution of Shot Rock. Proceedings of the Annual Conference on Explosives and Blasting Technique, Vol 1, ISEE, 2007.

Otsuka, M., Matsui, Y., Murata, K., Kato, Y., Itoh, S. "A study on Shock Wave Propagation Process in the Smooth Blasting Technique". 8th International LS-DYNA Users Conference. Strasburg. 2011.

Persson, G, Persson, P. A., "Estimation of Toxic Fume Characteristics of Explosives from Steel Tube Blasting", Propellants and Explosives, Vol. 5., 1980

Preece, D. S., Lownds, C. M. "3D Computer Simulation of Bench Blasting with Precise Delay Timing" Proceedings of the Thirty-Fourth Annual Conference on Explosives and Blasting Technique, New Orleans, Louisiana, January 27-30, 2008.

Preece, D. S. and Chung, S. H., Blasting Induced Rock Fragmentation Prediction Using the RHT Consitiutive Model for Brittle Materials, Proceedings of the 29th Annual Conference on Explosives and Blasting Technique, International Society of Explosives Engineers, Nashville, TN, February, 2003.

Preece, D. S., Explosive Destruction of an Underground Reinforced Concrete Bunker – Computer Hydrocode Simulation, Proceedings of the 32st Annual Conference on Explosives and Blasting Technique, International Society of Explosives Engineers, Dallas, TX, February, 2006.

Preece, D. S. Oil Shale Blasting Simulations Employing State-of-the-Art (2006) Computer Hydro-Codes and Constitutive Models, Proceedings of the 33d Annual Conference on Explosives and Blasting Technique, International Society of Explosives Engineers, Nashville, TN, January, 2007.

Quan, X., Birnbaum, N. K., Cowler, M. S., Gerber, B. I., Clegg, R. A., Hayhurst, C. J. "Numerical Simulations of Structural Deformation Under Shock and Impact Loads Using a Coupled Multi-Solver Approach". Proceedings of the 5th Asia-Pacific Conference on Shock and Impact Laods on Structures. November 12-14 2003. Hunan, China.

Rocha, M., Kemeny, J., BoBo, T., Rodriguez, C. "Calibration of a Fragmentation Model for a New Mining Operation" Proceedings of the 40th Annual Conference on Explosives and Blasting Techniques. Denver, CO. 2014

Rollins, R. R and Wang, S., Fragmentation prediction in bench blasting The 3rd International Symp. on Rock fragmentation by blasting, Brisbane, Australia, August 26-31, 1990: pp. 195- 199

Rossmanith, H. P. "The Mechanics of Electronic Blasting". Proceedings of the 33rd Conference on Explosives and Blasting Technique. ISEE 2003

Rossmanith, H. P., "The Use of Lagrangian Diagrams in Precise Initiation Blasting, Part 1: Two Interacting Boreholes". FRAGBLAST, Vol 6, No. 1, pp. 104-135. 2002.

Rossmanith, A. D., Knasmillner, R. E., Kouzniak, N., Ohtsu, M., Uenishi, K. "Fracture Mechanics Applications to Drilling and Blasting". Fatigue and Fracture of Engineering Materials and Structures Ltd. 1997.

Riedel, W. "Chapter 9 – 10 Years RHT: A review of Concrete Modelling and Hydrocode Applications" Predictive Modelling of Dynamic Processes. pp143-165. Springer. 2009.

Riedel, W., Thoma, K. Mayrhofer, C,. Stoltz, A. "Engineering and Numberical Tools for Explosion Protection of Reinforced Concrete. Int. J. Prot. Struct. I, 2010. pp. 85-101

Riedel, W., Thoma, K., Hiermaier, S.,Schmolinske, E. "Penetration of Reinforced Concrete by BETA-B-500, Numerical Analysis Using a New Macroscopic Concrete Model for Hydrocodes. Proceedings of the Ninth International Symposium Interaction of the Effects of Munitions with Structures. Berlin, 1999, pp. 315-332.

Schettler, L, Brashear., S., "Effect of Water on ANFO/Emulsion Blends in Surface Mine Blasting", Proceedings of the Twenty-Second Annual Conference on Explosives and Blasting Technique, Orlando, FL, February 4-8, 1996

Sellers, E. J., Kotze, M., Dipenaar, L., Ruest, M. (2010) Large Scale Cube Blasts for the HSBM Model. Rock Fragmentation by Blasting. London.

Shaw, D. E., Evaluation of Potential Blasting-Induced Damage to the Meason House. 1989

Siskind, D. E., Crum, S. V., Otterness, R. E., and Kopp, J. W., Comparative Study of Blasting Vibrations From Indiana Surface Coal Mines. United States Department of the Interior – Bureau of Mines, Report of Investigations 9226, Washington, D.C., 1989.

Siskind, D. E., Crum, S. V., and Pils, M. N., Blast Vibrations and Other Potential Causes of Damage in Homes Near a Large Surface Coal Mine in Indiana. United States Department of the Interior – Bureau of Mines, Report of Investigations 9455, Washington, D.C. 1993.

Siskind, D. E., Stachura, V. J., Stagg, M. S., and Kopp, J. W., Structure Response and Damage Produced by Airblast From Surface Mining. United States Department of the Interior – Bureau of Mines, Report of Investigations 8508, Washington, D.C., 1981.

Siskind, D. E., Stachura, V. J., Nutting, M. J., The Generation of Low-Frequency Long-Duration Vibrations from Surface Mine Blasting at Blandford, IN. United States Department of the Interior – Bureau of Mines. November 15, 1985.

Siskind, D. E., Stagg, M. S., Assesment of Blasting Vibration Impacts from Quarry Blasting in Dade County. D. E. Siskind & Associates, LLC. May 10, 2000.

Siskind, D. E., Stagg, M. S., Blast Vibration Measurements Near and On Structure Foundations. United States Department of the Interior – Bureau of Mines, Report of Investigations 8969, Washington, D.C., 1985.

Sjoberg. J., Schill. M. Hilding. D., Yi. C., Nyberg. U., Johansson. D. “Computer Simulations of Blasting with Precise Initiation”. Eurock. 2012

Stachura, V. J., Siskind, D. E., Engler, A. J., Airblast Instrumentation and Measurement Techniques for Surface Mine Blasting. United States Department of

the Interior – Bureau of Mines, Report of Investigations 8508, Washington, D.C., 1981.

Stachura, V. J., Fletcher, L. R., and Peltier, M. A., Delayed Blasting Tests to Improve Highwall Stability – A Final Report. United States Department of the Interior – Bureau of Mines, Report of Investigations 9008, Washington, D.C., 1986.

Stagg, M. S., Siskind, D. E., Stevens, M. G., and Dowding, C. H., Effects of Repeated Blasting on a Wood-Frame House. United States Department of the Interior – Bureau of Mines, Report of Investigations 8896, Washington, D.C., 1986.

Vabrabant, F. Espinosa, A., Impact of Short Delays Sequence on Fragmetnation by Means of Electronic Detonators: Theoretical concepts and field Validation, PRoc. 8th International Symposium on Rock Fragmantation by Blasting FRAGBLAST 8, pp 236-331. 2006

Watson, R. W., J. Roth, "A Review of Blasting Accidents in Surface Mining", Proceedings of the Annual Conference on Explosives and Blasting Technique, 1978

Williams, M.A., "Mining to Reduce Future Environmental Liabilities", Fifth High-Tech Seminar Blasting Technology Instrumentation and Explosives Applications, New Orleans, Louisiana, 1994

Worsey, P. N. "The Effects of Discontinuity Orientation on the Success of Presplit Blasting". Proceedings of the 10th Annual Conference on Explosives and Blasting Technique. Lake Buena, FL. 1984

Yamamoto, M. Experimental and theoretical study on smooth blasting with electronic delay detonators. Fragblast 3:3-24. 1999

Zhu. Z., Xie. H., Mohanty. B. "Numerical Investigation of Blasting-Induced Damage in Cylindrical Rocks". International Journal of Rock Mechanics and Mining Sciences 111-121. 2008.

VITA

Catherine Emily Johnson was born in Sidcup, Greater London, United Kingdom (UK) in 1989. She graduated from the University of Leeds with a Bachelors and Masters in Mining Engineering from the University of Leeds, UK in May 2012. In August that year, she began a Doctorate Degree at the University of Kentucky as part of the University of Kentucky Explosives Research Team in the Mining Engineering Department of the College of Engineering.

Publications

1. Johnson, C.E., B. Lusk, J.M. Hoffman, J. Rathbun, "Surface Coal Mine Blasting Optimization and Mitigation of Environmental Impacts: Mine to Fill." 2012 Environmental Considerations in Energy Production, ARIES Symposium, SME Littleton, CO
2. Lashgari, A., C. Johnson, V. Kecojevic, B. Lusk, J.M. Hoffman, "NOx Emission of Equipment and Blasting Agents in Surface Coal Mining." 2013 Mining Engineering, Society of Mining Engineering, Volume 65 Number 10, Littleton, CO
3. Birch, W.J., L. Bermingham., C. Johnson., R. Farnfield., S. Hosein. “Investigation to Determine the Origin of Air Overpressure from Quarry Blasting”. 2014. Journal of Explosives Engineering, International Society of Explosives Engineers, Volume 31 Number 1, Cleveland, OH.

Refereed Conference Papers and Presentations

1. Birch, W.J., L. Bermingham., C. Johnson., R. Farnfield., S. Hosein. “Investigation to Determine the Origin of Air Overpressure from Quarry Blasting”. 2013. Proceedings of the Thirty-Ninth Annual Conference on Explosives and Blasting Technique.” Dallas, Fort Worth, TX
2. Johnson, C., B.T., Lusk, J.M., Hoffman, "Investigating Colliding Shock", 2014. Proceedings of the Fortieth Annual Conference on Explosives and Blasting Technique.” Denver, CO

3. Johnson, C., B.T., Lusk, J.M., Hoffman, "Risk Assessment Software Applied to Large Bomb Detonations Near Structures", 2014. Proceedings of the Fortieth Annual Conference on Explosives and Blasting Technique." Denver, CO
4. Johnson, C., B.T., Lusk, J.M., Hoffman, "NOx Emissions from Blasting Activities in a Surface Mining Operation", 2014. Proceedings of the Fortieth Annual Conference on Explosives and Blasting Technique." Denver, CO
5. Hoffman, J.M., C., Johnson, "A Survey to Better Understand Collegiate Talent for Recruiting Purposes", 2014. Proceedings of the Fortieth Annual Conference on Explosives and Blasting Technique." Denver, CO
6. Lashgari, A., Johnson, C., Kecojevic, V., Lusk, B., Hoffman, J.M. "NOx Emission of Equipment and Blasting Agents in Surface Mining". Proceedings of the 143rd Annual Meeting and Exhibition of the Society of Mining, Metallurgy and Exploration, Salt Lake City, UT, February 23-26, 2014.

Research Assistant Experience and Projects of Involvement

1. Lusk, B (PI), Honaker, R, Perry, K, Novak, T "University of Kentucky Experimental Mine Feasibility Study" Kentucky Department for Energy Development and Independence. July 2012-July 2014 (Budget $350,000)
2. Lusk, B (PI), "Development of Unitized Mining Operations for Optimum Fill Construction" Appalachian Research Initiative for Environmental Science, Industry funded. August 2011 - August 2016 (Budget $375,000).